Aus dem Pathologischen Institut

der Ludwig-Maximilians-Universität München

Direktor: Prof. Dr. med. Thomas Kirchner

Dissertation

zum Erwerb des Doctor of Philosophy (Ph.D.) an der

Medizinischen Fakultät der

Ludwig-Maximilians-Universität zu München

Therapeutic targeting of cytokinesis eradicates genomically silent childhood cancer

vorgelegt von:

.....Jing Li.....

aus:

...Yinchuan, Ningxia, China...

Jahr:

.....2020.....

Mit Genehmigung der Medizinischen Fakultät der

Ludwig-Maximilians-Universität zu München

First supervisor: *Prof. Dr. Dr. med. Thomas Grünewald*

Second supervisor*:* *Prof. Dr. med. Thomas Kirchner*

Third supervisor: Prof. Dr. rer. nat. Andreas Jung

Dean: Prof. Dr. med. dent. Reinhard Hickel

Datum der Verteidigung:

___27.04.2021__

Table of content

Summary

One feature of cancer is chromosomal instability (CIN). Through moderate CIN, most cancer types acquire somatic copy number alterations during each cell division creating intra-tumor heterogeneity that enhances the overall 'fitness' of the cancer cell population. Yet, excessive CIN can lead to non-viable karyotypes. While CIN-induction in cancer types that are intrinsically genomically instable may have little therapeutic benefit, it may cause massive cell death in cancers with 'silent' or nearly diploid genomes, as for instance in many pediatric cancer types including Ewing sarcoma (EwS).

To identify a candidate gene that could offer a large therapeutic window, the results presented in this thesis focused on protein regulator of cytokinesis 1 (PRC1), the most significantly overexpressed cytokinesis-related gene in EwS. PRC1 plays pivotal roles in orchestrating cytokinesis through its direct involvement in bundling of antiparallel microtubules (MTs) required for spindle midzone formation, recruitment of and interaction with other spindle midzone effectors and regulatory proteins.

The results presented in this thesis show that EWSR1-FLI1 directly hijacks *PRC1*, which physiologically safeguards controlled cell division, through binding to a proximal enhancer-like GGAA-microsatellite (mSat) thereby promoting tumor growth and poor clinical outcome. Moreover, high PRC1 expression creates a therapeutic vulnerability toward pharmacological PLK1 inhibition at clinically achievable dosages that can repress growth of even chemo-resistant EwS cells by triggering mitotic catastrophe.

List of figures

List of tables

List of abbreviations

3C-seq	Chromatin conformation capture sequence
BAF	BRG1-BRM-assocated factor
BCS	Body Condition Scores
CC	Coiled-coli
CC3	Cleaved caspase-3
CDK	Cyclin-dependent protein kinases
CDX	Cell-derived xenograft
CFI	Cleavage furrow ingression
CIN	Chromosome instability
crRNA	CRISPR RNA
DAPI	4,6-diamidino-2 phenylindol/propidium iodide
DEGs	Differentially expressed genes
DMSO	Dimethyl Sulfoxide
Dox	Doxycycline
Doxo	Doxorubicin
Doxo-res	Doxorubicin-resistant
DRI	Dose reduction index
ED50	Median effective dose
ENCODE	Encyclopedia of DNA Elements
ERG	Encoding transcriptional regulator
EwS	Ewing sarcoma
EWSR1	Ewing sarcoma breakpoint region1 protein
FCS	Fetal calf serum
FCs	Fold changes
FDR	False discovery rate
FFPE	Formalin-fixed and paraffin-embedded
FISH	Fluorescence-in-situ-hybridization
FITC	Fluorescein isothiocyanate
FLI1	Friend leukemia integration 1 transcription factor
genomic DNA	gDNA
GFP	Green fluorescent protein
GO	Gene Ontology
GPP	Genetic Perturbation Platform
GSEA	Functional gene-set enrichment
HDR	Homology-directed repair
HE	Hematoxylin and eosin
HPF	High-power field
HRP	Horseradish peroxidase
i.v.	Intravenously
IC10	Inhibitory concentrations of 90% viability

IC50	50% inhibitory concentration
IHC	Immunohistochemistry
iMTs	Interpolar MTs
IRS	Immune Reactive Score
KI	Knock in
KIF14	Kinesin family member 14
KIF4A	Kinesin family member 4A
KO	Knockout
MAPs	Microtubule associated proteins
mSats	Microsatellites
MSCs	Bone-marrow-derived mesenchymal stem cells
MT	Microtubule
NC	Negative control
NGS	Next-generation sequencing
NSG	NOD/Scid/gamma
OR	Odds ratio
OS	Overall survival
PBD	Polo-kinase binding domain
PBS	Phosphate buffered saline
PDX	Patient-derived xenograft
PI	Propidium iodide
PLK	Polo-like kinase
PLK1	Polo-like kinase 1
PLK1i	PLK1 inhibition
PP2A-B55a	Protein phosphatase 2A regulatory subunit B 55a
PRC1	Protein regulator of cytokinesis 1
RI	Reverse index
RIN	RNA integrity numbers
RNP	Ribonucleoprotein
RT-PCR	Reverse transcription PCR
SDS	Sodium dodecyl sulfate
SDS-polyacrylamide-gel electrophoresis	SDS-PAGE
SEM	Standard error of the mean
shRNA	Small hairpin RNA
SSC	Standard saline concentration
STR	Short Tandem Repeat
TD-PCR	Touch-down PCR
TMAs	Tissue-microarrays
TOPK	T-LAK cell-originated protein kinase
tracrRNA	Trans-activating crRNA
VCR	Vincristine
WGCNA	Weighted correlation network analysis

WGS	Whole genome sequencing
WT	Wide type

1. Introduction

1.1 Chromosome instability (CIN)

1.1.1 Sources of CIN in cancer

CIN refers to the accumulated gain/loss of chromosomes over cell divisions, which is a general feature of cancer [1]. Most human tumors represent chromosomal abnormalities indicative of CIN, with a ratio of 60% to 80% [1]. Genetic heterogeneity derived from CIN set up a foundation for clonal evolution and selection. It is also positively associated with a higher tumor grade, higher recurrence/metastasis, and a reduced patient survival [2]. Furthermore, a large set of cancer-related pathways involve CIN. The dysregulation of such pathways can change normal chromosome division in mitosis [3]. Indeed, many factors, e.g., oncogenic signaling, pre-mitotic replication stress, all promote the development of CIN [4].

A profound influence of CIN in malignant cells is that it alters mitotic phenotype features [5]. For example, cells with lagging chromosomes in the anaphase spindle are the consequences of their defective MT attachments at the kinetochores (**Figure 1**). Other chromosome mis-segregations in mitosis include chromatin/ultrafine DNA bridges and acentric fragments. With the exception of aneuploidy and severer structural chromosomal alterations, chromosome mis-segregation can trigger focal but profound rearrangement known as chromothripsis, double-minute chromosome, as well as extrachromosomal DNA (**Figure 1**) [6].

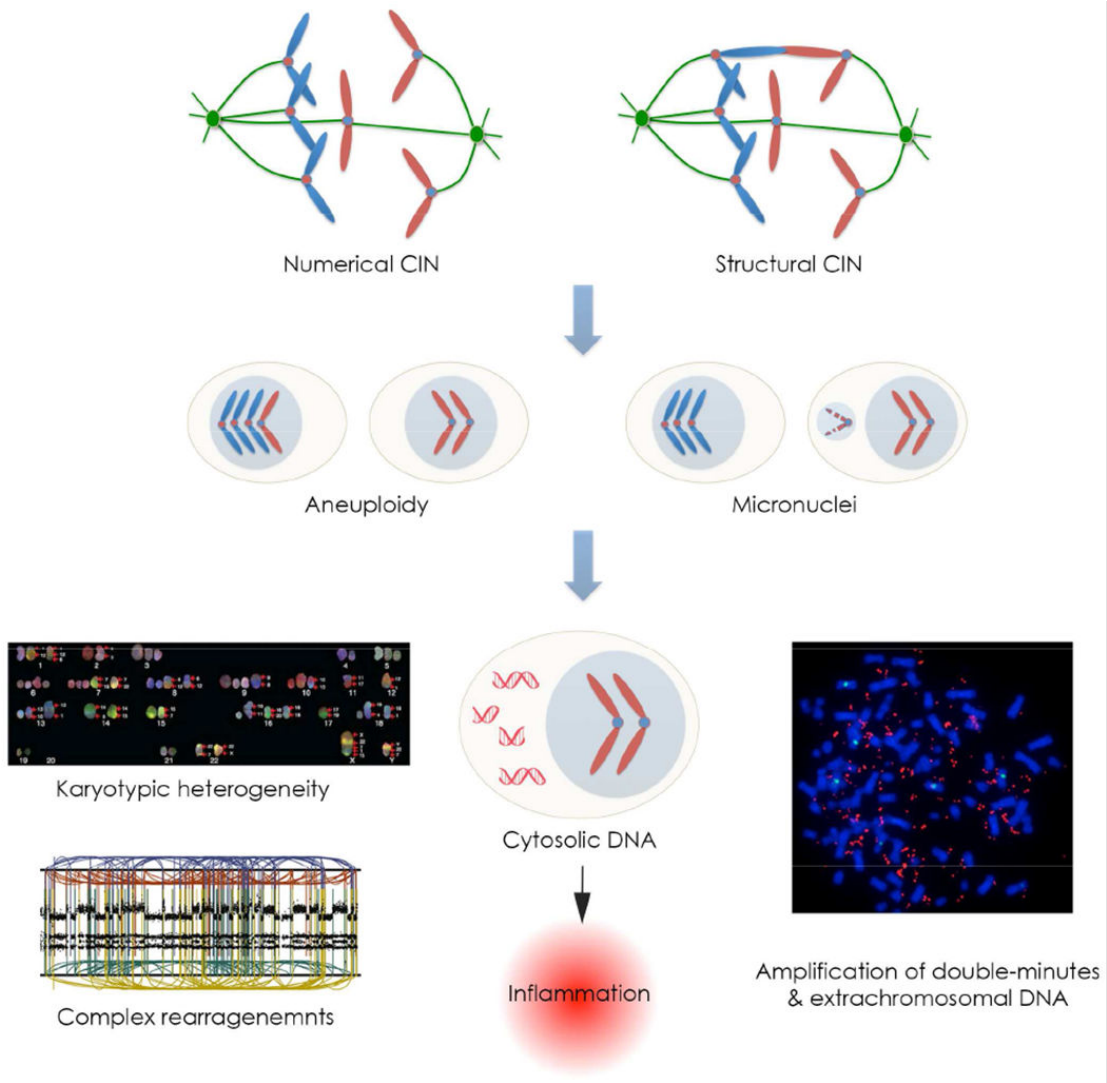

Figure 1 CIN in Cancer

(Figure adopted from Bakhoum and Cantley, *Cell*, 2018 [6])

1.1.2 CIN to Cancer: good or bad?

While being considered as a hall marker of cancer, the involvement of CIN in tumor evolution shows both sides of the coin [7]. Aneuploidies induced by CIN positively correlate with antineoplastic agents resistance in (pre)clinical settings [1]. In contrast, severe CIN can increase sensitivity of tumor cells towards cytotoxic and/or radiation treatments [8]. These findings indicate that optimal fitness for cancer cell survival is obtained by adjusting CIN into an appropriate scope [8].

CIN-induced chromosome copy number diversity is a substrate for natural selection increasing cancer cell viability and promoting immune evasion, enhancing

drug response as well as metastasis [9]. Parallelly, chromosome segregation failures convey a set of cellular stresses (e.g., loss of chromosomes, activation of DNA damage signaling as well as proteotoxic stress) (**Figure 2**) [10]–[12].

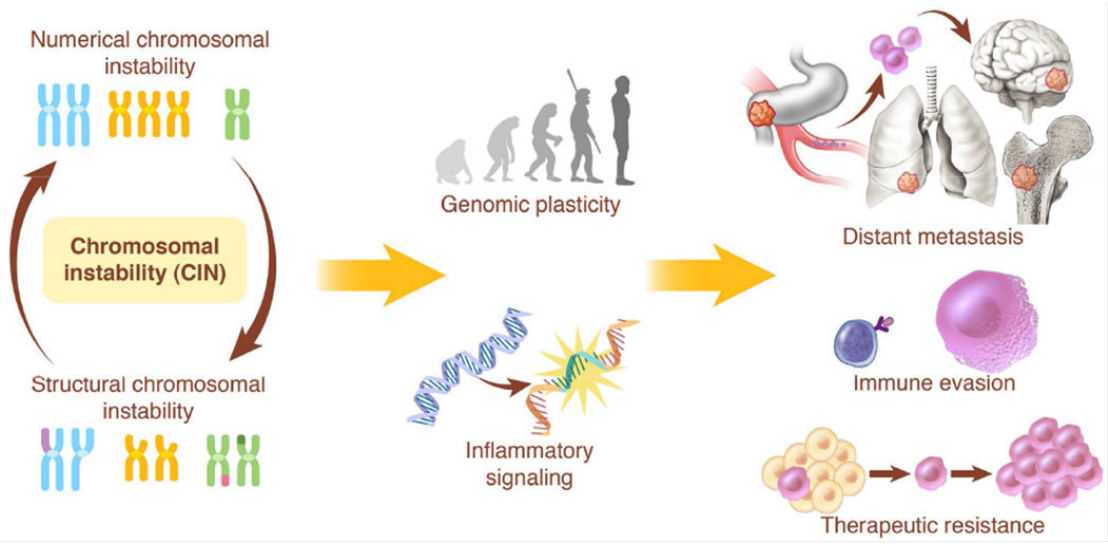

Figure 2 The multi-faceted roles of CIN in cancers

(Figure adopted from Bakhoum and Cantley, *Cell*, 2018 [6])**.**

1.1.3 Induction of high CIN as an anti-tumor therapeutic intervention

Several studies have reported that multiple mouse models with low CIN rate developed late onset of low penetrance tumors. However, increasing CIN rate in the same study led to cell death and suppressed tumors in multiple settings [13], [14]. A similar finding has been verified *in vitro* as well [15]. Collectively, despite the low CIN's weakly tumor promoting effect, high rates of CIN can inhibit tumor growth via inducing massive cell death. Moreover, tumor cells have to limit chromosome mis-segregation rates within a restricted scope maximizing viability in order to keep balance between genome instability and the acquisition of heterogeneity [8].

It is conceivable that leveraging CIN rate over a critical threshold could be exploited therapeutically. As many cancers intrinsically harbor CIN, they are supposed to be more vulnerable than normal dividing cells to CIN-induced agents. In this regard, such agents are expected to safeguard proliferating tissues lacking CIN [16]. For example, Taxol, PARP inhibitors, as well as ionizing radiation are some of the strongest agents inducing chromosome mis-segregation [6].

However, despite recent progresses in the knowledge of CIN in the biological field, clinical adoptions of CIN-induced interventions are still in their infancy. Although demonstration of the CIN has been well demonstrated in cancer cell lines or in mouse models, it is still unclear whether such models can faithfully explain the types of CIN found in real patients. Moreover, detailed elucidation of genetic and epigenetic contributors and outcomes of CIN in human cancers should be clearly interpreted. Given the wide spread of CIN in human cancers, CIN-induced treatments do have the ability to significantly reshape clinical outcomes, through i.e. minimizing the initiation of therapeutic resistance, priming advanced or metastatic disease. However, careful patient selection is required for determining when such intervention will be beneficial to tune CIN and when it might be notorious [17].

1.2 Ewing sarcoma (EwS)

1.2.1 Cell of origin

EwS is thought to be derived from a single cellular lineage with varying developmental timing of oncogenic conversion followed by damaged differentiation potential because of its lack of genetic subtypes [18]. About 80% of EwS cells are present in bone, suggesting progenitors might locate in the developing bone mesenchyme [18]. A mesenchymal origin of EwS has also been proposed. It has been reported that in EWSR1-FLI1 proficient cells the gene expression pattern mimics the ones from neural-crest-derived stem cells, while downregulation of EWSR1-FLI1 steers the EwS transcriptome towards that of bone-marrow-derived mesenchymal stem cells (MSCs) [19]. Additionally, the idea of an epithelial origin has been raised as well [20].

1.2.2 Genetic features

EwS is a quite gnomically ‘silent’ disease featured by a recurrent balanced chromosomal translocation [21]. The fusion of the *FET* family gene *EWSR1* with the *ETS* family gene *FLI1* at t(11;22)(q12;q24) is the most common one (~85%) [22] (**Figure 3**). Through functionally interacting with EWSR1-FLI1, moderate risk al-

leles might contribute to disease progression [23]. Based on the location of breakpoints within *EWSR1* and *FLI1* genes, various subtypes of *EWSR1-FLI1* transcripts have been discovered [24] (**Figure 3**). Different fusions between *EWSR1* and other members of the *ETS* family have been identified with *ERG* (encoding transcriptional regulator *ERG*) being the most commonly one [25]. Subsequently, *ETV1* [26], *ETV4* [27] or *FEV* [28] fusions to *EWSR1* were found. Additionally, some variant fusions were identified between *ETS* genes and *EWSR1* paralog of the *FET* gene family (*FUS* and *TAF15*) [29] (**Figure 3**).

Of note, unlike most developmental malignances, other mutations in EwS are unusual. For instance, *TP53* and *STAG2* mutations are represented at diagnosis in 5-7% and 15-21%, respectively [30]. Recurrent chromosomal abnormalities in EwS generally involve whole or segmental chromosomes [31], [32].

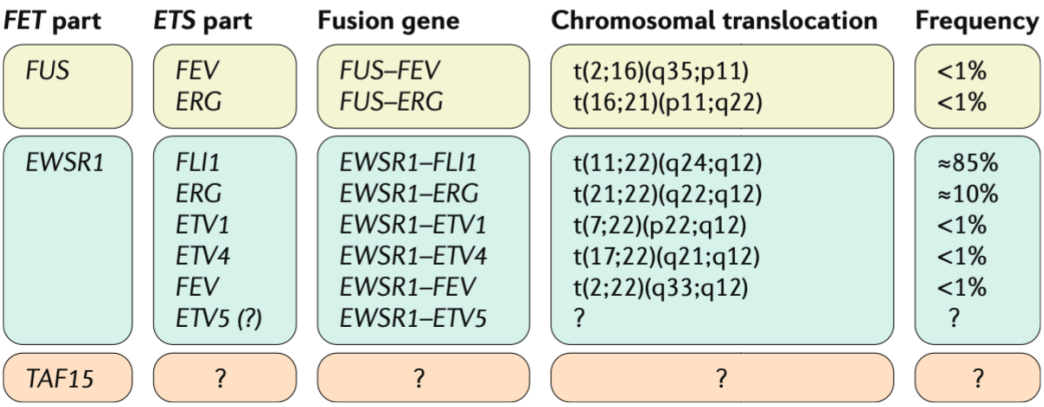

Figure 3 Genetic predisposition to EwS.

(Figure adopted from Grünewald and Cidre-Aranaz, *Nature Rev Disease Primers*, 2018 [33])

Enhancers are dynamically cell-type-specific elements that regulate activation of gene expression in a time and space dependent manner. In EwS, the genome-wide enhancer signature is quite similar [34], which is functionally related to the oncogenic transformation by *EWSR1-FLI1*. GGAA-mSats are EwS specific enhancers, acting as pioneer transcription factors surmounting the non-opened chromatin state of the GGAA-mSats in EwS [35]–[37]. This interaction increases approachability of DNA to other transcription factors, chromatin adjustors and remodeling compounds [35], [37]. Notably, it has been reported that *EWSR1-FLI1*

is able to interact with subunits of the BRG1-BRM-assocated factor (BAF) chromatin-remodeling compounds, leading to translocation of BAF compound at GGAA-mSats [37]. Subsequently, the recruitment triggers chromatin remodeling, builds up *de novo* enhancer elements and activates the EwS transcriptional program [37] (**Figure 4**).

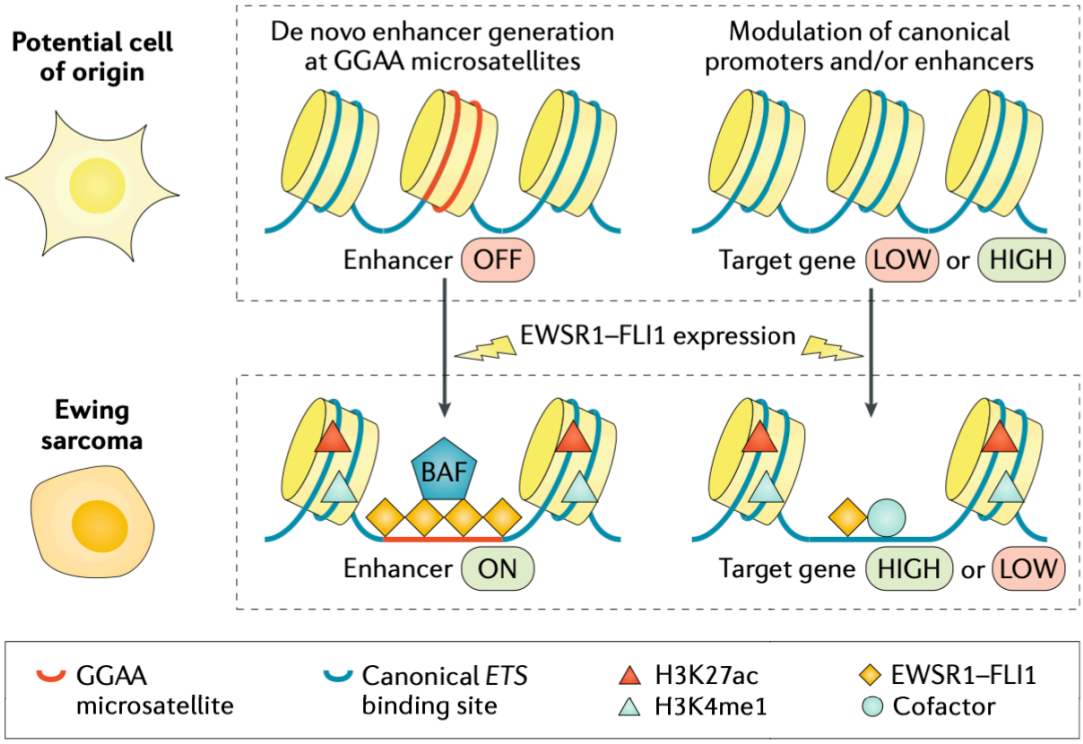

Figure 4 EWSR1-FLi1-mediated epigenetic remodeling of regulatory elements.

(Figure adopted from Grünewald and Cidre-Aranaz, *Nature Rev Disease Primers*, 2018 [33])

Non-coding RNAs conduct epigenetic regulation in EwS cells as well. Indeed, *EWSR1-FLI1* regulates a number of non-coding RNAs (e.g. *miR-34a*, *miR-145*), which actively participate in EwS tumorigenesis [38].

1.2.3 Pathology, diagnosis and therapy

Histologically, EwS is classified as a small round cell with round nuclei, a heterogeneous group of malignancies that are nevertheless morphologically quite similar [39]. Sufficient materials of EwS through a biopsy is required for the precise diagnosis for classical histology, immunohistochemistry (IHC), molecular pathol-

ogy and biobanking [40]. CD99, a cell-surface glycoprotein, is a sufficient auxiliary diagnostic indicator for EwS [42]. IHC revealed that ~95% of EwS represent high and disperse expression of CD99 in the membrane [39]. However, CD99 expression is not unique for EwS as it is also broadly expressed in normal tissues as well as in other tumors [39]. Recently, our lab found that BCL11B and GLG1 may serve as specific auxiliary IHC markers in conjunction with CD99 for EwS diagnosis when confirmatory molecular diagnosis has failed [42]. Fluorescence-in-situ-hybridization (FISH)-based detection of *EWSR1* rearrangements and/or reverse transcription PCR (RT-PCR) as well as detection of *FET-ETS* gene fusions that are characteristic for EwS have been widely used currently as more robust diagnostic tools [43]. Next-generation sequencing (NGS) is recommended when FISH and/or RT-PCR cannot produce precise results [33].

Newly diagnosed EwS patients generally receive a combination of multi-agent cytotoxic chemotherapy with local treatment (surgery and/or radiotherapy). Chemotherapy is carried out before local treatment in order to minimize the load of the local tumor and manage micro-metastatic disease [44]. Metastatic EwS patients are treated with agents utilized in localized patients or tested in randomized clinical trials aimed at improving patients survival [45]. Recurrent EwS is always correlated with a very poor survival, with a 5-year survival of less than 10% [46]. A highly resistant clone of cancer cells that developed under treatment, may explain a potential source of relapse [47]. Admittedly, development of novel treatments for EwS is still at slow pace because of the rarity of EwS. Although several clinical trials with EwS patients have been performed, just modest efficacies were observed. Thus, it is urgent to search for innovative targeted therapeutic agents, e.g., small-molecular inhibitors like YK-4-279 [48].

1.3 Protein regulator of cytokinesis 1 (PRC1)

1.3.1 Cytokinesis

Cytokinesis, the final stage of cell mitosis, physically splits one parental cell to two equal offspring. Cytokinesis should be properly done to maintain genome stability, the defect of which can lead to aneuploidy contributing to cancer development [49]. Accurate time-and-spatial control of cytokinesis ascertains that each

offspring gains one complete equal amount of chromosomes, evenly distributed cytoplasm and cellular organelles. Such fine-tuned processes are regulated delicately by a complex network of fibrillary structures (**Figure 5**) [50].

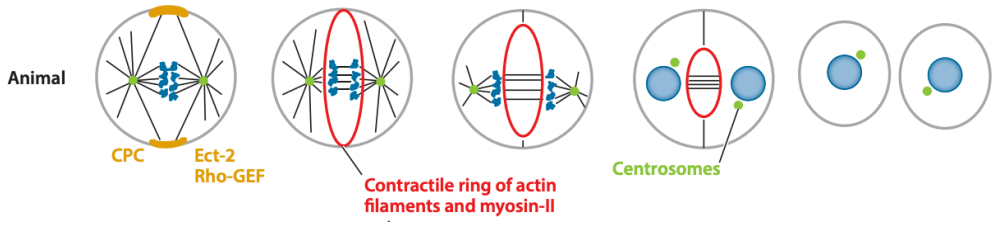

Figure 5 Illustrations the steps in cytokinesis by animals.

(Figure adopted from Pollard and O'Shaughnessy, *Annual Reviews*, 2019 [51])

1.3.2 Structure and Role of PRC1

PRC1 contains 620 amino acids. It has multiple domains, namely central microtubule (MT)-binding, rod, dimerization, and Lys/Arg-rich domains (**Figure 6a**). The 5'-terminus comprises alpha-helices featured by a number of coiled-coli (CC) motifs. The 3'-terminus consists of beta sheets and turns [52]–[54]. PRC1 cooperates with other actin-binding proteins via the interaction of PRC1 central MT-binding domain with actin-binding protein spectrin domain [55], in which the central MT-binding domain is linked to the rod domain through its constituting three helices [56]. The structural stability of PRC1 is preserved via the formation of its rod domain linked to the dimerization domain [57]. Though the clear functional role of Lys/Arg-rich unstructured 3' terminus is not clear yet, the Lys/Arg-rich unstructured 3' terminus is actively involved in increasing the affinity of the central MT-binding domain [55], [56]. Additionally, two nuclear localization signals and two cyclin-dependent protein kinases (CDK) 1 phosphorylation sites at Thr-470 and Thr-481 are all located in the 3'-terminus [56].

PRC1 is structurally flexible but stable via the formation of various rigid conformations by body rotations. One major function of PRC1 is bundling overlapping interpolar MTs (iMTs), which relies on PRC1-formed-homodimers via forming a U-shaped hairpin in the dimerization domain. Then, the orientation of two rod domains is changed to opposite directions, which is critical for MT crosslinking and serves as a platform of recruiting other proteins, e.g., Kinesin family member 4A (KIF4A) [52], [55]–[57] (**Figure 6b**).

1.3.3 Regulation of PRC1 expression

Several kinases and phosphatases are tightly regulated and participate in the PRC1-involved cytokinesis process. In the early stage of mitosis, CDK1/cyclin B phosphorylates PRC1 at Thr-470 and Thr-481 to suppress PRC1 dimerization [58]. This process is promoted by TOPK (T-LAK cell-originated protein kinase) via forming the CDK1/cyclin B/PRC1 complex [59]. Monomeric PRC1 lacks the ability of bundling MT's and its interaction with KIF4A, though it can bind spindle MTs [54], [60] (**Figure 6c**).

When entering anaphase from metaphase, the dephosphorylated PRC1 is activated by the mitotic phosphatases, such as Cdc14A, which enforces PRC1 interaction with KIF4A [54]. PRC1 further moves and resides in the plus-ends, where PRC1 bundles antiparallel iMTs with the help of KIF4A and then forms midzone for other critical microtubule associated proteins (MAPs) [61].

Moreover, the PP2A regulatory subunit B55a (PP2A-B55a) regulates PRC1 as well (**Figure 6c**). The CDK1-mediated inactivated dephosphorylation of PRC1 and PP2A-B55a/ENSA/Greatwall pathway-mediated activated dephosphorylation of PRC1 take place in such a fine-tuned time-and-spatial way that PRC1 is completely activated in the early stage of anaphase [62].

PRC1 is phosphorylated and bound to polo-like kinase 1 (PLK1) during the anaphase (**Figure 6d**). Polo-kinase binding domain (PBD) is required for such targeting[63], [64], [64], [64]–[67]. Of note, PLK1 shares overlapped CDK1-dependent docking sites for phosphorylation and thus establishes a frame where PLK1 translocation and activity are finely adjusted in the early stage of mitosis when CDK1 is active [68]. Specifically, PRC1 is phosphorylates by CDK1 at Thr-470 and Thr-481, which avoids PRC1 phosphorylation by PLK1 [68]. Since the function of CDK1 is inactivated in the early stage of mitosis, PRC1 is phosphorylated by PLK1 at Thr-578 and Thr-602 in anaphase, which enhance the affinity of PLK1-PRC1 complex. These two different docking sites of PLK1 have different roles: PRC1 is activated via phosphorylation at Thr-602. Thr-578 can stabilize PBD binding to increase approachability of PRC1 to Thr-602 [68]. Notably, CDK1

seemingly has no pre-anaphase regulatory effect on PRC1. Instead, the phosphorylation of PRC1 by PLK1 at Thr-602 can ascertain mature midzone assembly [69].

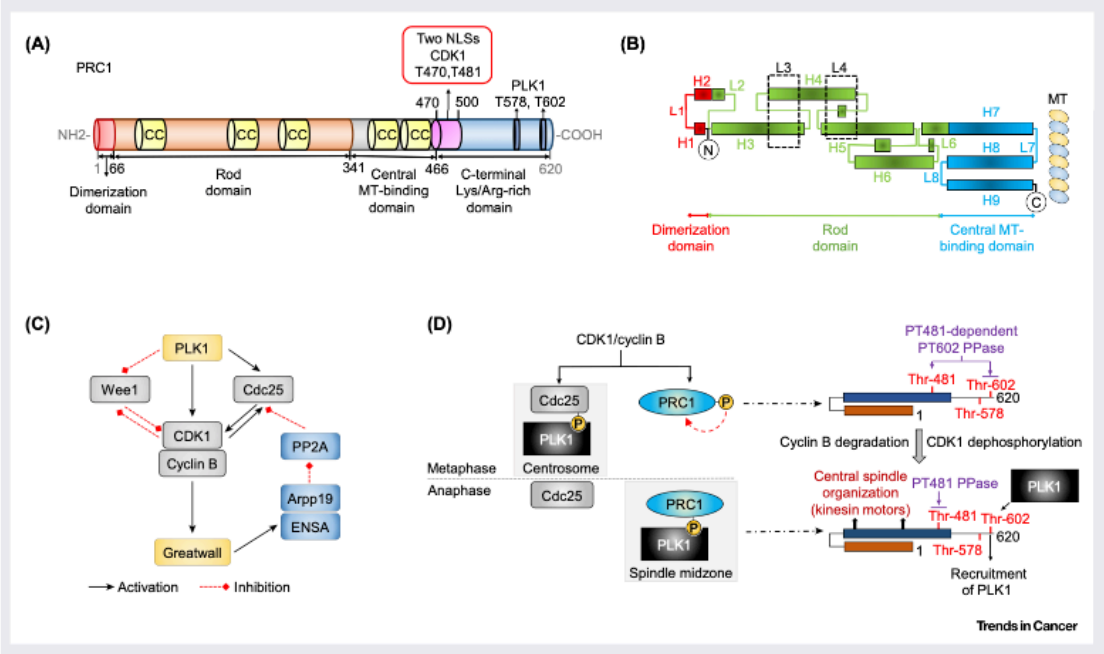

Figure 6 PRC1 modular structure and its expression regulated by several pathways

(Figure adopted from Li *et al. Trends in Cancer*, 2018 [70]**).**

1.3.4 PRC1 is essential for normal cell cytokinesis

PRC1 is a key player in the network of fibrillary structures required for normal cytokinesis. The heterogeneous expression of PRC1 determines the frequency of mitosis in different tissue and organs [71]. PRC1 locates in nuclei in interphase and then moves to the spindle when entering into mitosis. Finally, PRC1 resides in midzone post-mitotic bridges until the end of cytokinesis [52].

PRC1 plays essential roles in spindle midzone formation. PRC1 crosslinks iMTs to maintain the stability of two iMTs [60]. This process has been further facilitated by the central MT-binding domain of PRC1 [55]. The 3'-terminus of PRC1 ascertains fine-tuned flexible linking between two antiparallel MT filaments, which enhances PRC1 crossing-linking activity [55]. The resulting cross-bridge determines the distance between interdigitating MTs (35 nm), which influences the interactions of PRC1 with other motor proteins [55], [72]. Silencing of *PRC1* strongly disables iMTs bounding activity and disrupts spindle midzone formation, subsequently causing significant mitotic defects [58], [73].

Cleavage furrow ingression (CFI) relies on synergistic work of contractile ring with spindle midzone. PRC1 directly interacts with kinesin family member 14 (KIF14) to promote citron kinase translocation to the midzone, thereby providing maintenance of the spindle stability over the period of constriction to abscission [74]–[76].

K-fibers provide mechanical pulling forces, with which interkinetochore stress between sister kinetochores is adjusted by bridging fibers. In order to preserve the curve-shaped spindle in the metaphase, bridging fibers where PRC1 stretches from spindle midzone to the position of kinetochores link k fibers internally [77]. These findings suggest that PRC1-enriched fibers can bind to sister k fiber.

1.3.5 PRC1 in tumorigenesis

Silencing of *PRC1* induces generations of binucleated cells, the accumulation of which is a major risk factor of aneuploidy formation [58]. PRC1 overexpression also causes abnormal ploidy formation, potentially owing to obstruction of the well-adjusted cytokinesis. Remarkably, PRC1 ranked as the second highest CIN-associated gene in a large gene set comprising 10,151 genes from different cancer entities [78]. PRC1 overexpression was related with strong abnormal ploidy formation followed by a poor overall survival in a CIN signature [78]. Tetraploid, a common consequence generated by cytokinesis defects, promotes severe aneuploidy, tumor progression and worse survival of patients [79]–[81]. Indeed, while physiologically PRC1 seems to safeguard genome stability [81], PRC1 is commonly dysregulated in different cancers, suggesting the prognostic value of PRC1 in cancer.

Therapeutically targeting PRC1's upstream kinases and/or pathways may provide novel approaches to disrupt delicate cytokinesis/mitosis that induce CIN in cancer. Despite the expression/activity of PRC1 can be adjusted by some indirect approaches in cancer, identifying drugs which directly target PRC1 is urgently required. By the same token, more studies are required towards achieving a clearer and more comprehensive understanding of the manner in which PRC1 promotes tumorigenesis and CIN.

2. Research Design

2.1 Objectives

EwS is a bone and soft-tissue cancer with highly aggressive behaviors. It mostly affects children, adolescents, and young adults. EwS often shows an unfavorable clinical course, despite very intensive therapies. Especially patient's prognostic value is still unsatisfied, which urges the development of innovative and in particular less toxic therapeutic options for EwS patients.

Genetically, EwS is characterized by pathognomonic *EWSR1-ETS* fusion oncogenes (in 85% *EWSR1-FLI1*), which encodes aberrant transcription factors that massively rewire the tumor transcriptome. Despite rapid proliferation, EwS cells maintain a remarkably stable genome. In fact, most EwS do not show any other genomic abnormality than *EWSR1-ETS* and exhibit a largely diploid genome without CIN, which is maintained by a fine-tuned balance of mitosis and cell division (cytokinesis).

This PhD project aimed at targeting the delicate balance between mitosis and cytokinesis that could drive EwS cells into cell death, which may constitute a new approach for targeted therapy.

2.2 Scientific aims

1st aim: Analysis of the PRC1 expression pattern in EwS, other pediatric cancers, and normal tissues as well as prospective validation of PRC1 as a prognostic marker.

2nd aim: Investigation of EWSR1-FLI1 mediated *PRC1* expression in EwS.

3rd aim: Functional characterization of the phenotypic effects of PRC1 *in vitro* and *in vivo.*

4th aim: Evaluation and validation of the transcriptomic effects of PRC1 silencing.

5th aim: Analysis of CIN and aneuploidy induced by PRC1 silencing and/or PLK1 inhibition *in vitro* and *in vivo.*

6th aim: Functional characterization of PRC1-dependent effects of PLK1 inhibition *in vitro* and *in vivo*

7th aim: Functional characterization of PRC1-dependent effects of PLK1 inhibition in combination with chemo-reagents *in vitro*.

3. Materials and methods

3.1 Materials

3.1.1 List of manufacturers

Manufacturer	Location
(Carl) Roth	Karlsruhe, Germany
Abcam	Cambridge, UK
Agilent Technologies	Santa Clara, USA
Applied Biosystems	Darmstadt, Germany
ATCC	Rockville, Maryland, USA
BD Biosciences Europe	Heidelberg, Germany
Biochrom	Berlin, Germany
BioRad	Richmond, California, USA
Cambio	Cambridge, UK
Cell Marque Corporation	Rocklin, California, USA
Cell Signaling Technology	Frankfurt a. M., Germany
Corning incorporated	New York, USA
Eppendorf	Hamburg, Germany
Falcon	Oxnard, California, USA
Fischer Scientific	Schwerte, Germany
Gilson Incorporated	Middleton, USA
HP Labortechnik	München, Germany
IDT technologies	Coralville, Iowa, USA
INTEGRAbiosciences	Zizers, Switzerland
Invitrogen	Karlsruhe, Germany
InVivoGen	San Diego, California, USA
Leica Biosystems	Wetzlar, Germany
LI-COR	Nebraska, USA
Life Technologies	California, USA
Macherey-Nagel	Düren, Germany
Merck Millipore	Burlington, Massachusetts,
New England BioLabs	Frankfurt a. M., Germany
OriGene Technologies	Rockville, Maryland, USA
Pechiney Plastic Packaging	Menasha, Wisconsin, USA
Promega	Madison, Wisconsin, USA
Proteintech Group	Leon-Rot, Germany
Qiagen	Chatsworth, California, USA
OriGene Technologies	Rockville, USA
Roche	Mannheim, Germany
Santa Cruz Biotechnology	Heidelberg, Germany
Selleckchem	Munich, Germany
Sigma-Aldridge	St. Louis, Missouri, USA
Takara Bio Europe	Saint-Germain-end-Laye,
Thermo Fisher Scientific	Ulm, Germany
Thermo Scientific	Braunschweig, Germany

Zeiss	Oberkochen, Germany

3.1.2 General materials

Material	Manufacturer
6, 12, 24 and 96-well-plate	Corning Incorporated
96-well-plate (white)	Corning Incorporated
Amersham Protran 0.45 nitrocellulose Western blotting membranes	GE Healthcare
Blotting paper	Hartenstein
Cell culture flasks (150, 75, 25 cm)	Corning Incorporated
Cell scraper	Corning Incorporated
Costar Ultralow attachment plates 96-well	Corning Incorporated
Eppendorf Tubes (1.5 and 2 ml)	Hartenstein
Falcon Tubes (15 ml and 50 ml PP or PS)	Falcon
HandyStep electronic	Brand
Heating lamp	Beurer GmbH
Nunclon cell culture dish (10 cm)	Thermofisher
Optical adhesive film for 96er PCR-Plates	Fisher Scientific
Parafilm	Pechiney Plastic Packaging
Pasteur Pipette	Hartenstein
PCR-Plates (96-well)	Fisher Scientific
Pipetboy	INTEGRA Biosciences
Pipette tips (10 µl, 20 µl, 100 µl, 200 µl, 1000 µl)	Biozym
Pipettes (0.5-10 µl, 10-100 µl, 100-1000 µl)	Gilson
Scalpels	Mergo GmbH & Ko KG
Stripette (2, 5, 10, 25 and 50 ml)	Corning Incorporated
Needle and syringe for intravenous injection (BD Micro-Fine™+ Insulin)	BD Biosciences
Syringes for viruses (0,45 µm)	(Carl) Roth

3.1.3 Mice strains

Mouse strain	Manufacturer
NSG(NOD.CG-SCID): NOD-scid IL2Rgammanull, NOD-scid IL2Rgnull, NSG, NOD scid gamma	The Jackson Laboratory
NOD/SCID: NOD/MrkBomTac-Prkdcscid	Taconia Denmark ApS

3.1.4 Instruments and equipments

Device	Specification	Manufacturer
Affymetrix-Gene Chip	Human Clariom™ D	Thermofisher
Autoclave	Varioklav	HP Laboratortechnik

Bacteria incubator	Kelvitron	Heraeus
Bacteria shaker	Certomat IS	Braun BioTech internat.
Cell counter	Countess II	Thermofisher
Centrifuge	Heraeus™ Megafuge™40	Heraeus
Centrifuge	Centrifuge (5424 Rand 5430)	Eppendorf
Controlled-freezing box	Mr. Frosty	Nalgene
Electrophoresis	Mini Trans-Blot	Biorad
ELISAreader	Varioskan™LUX	Thermofisher
Flow Cytometer	BD Accuri™C6	BD Biosciences
Freezer (-20°C)	No Frost	Siemens
Freezer (-80°C)	B 35-50	Fryka
Gel documentation	Multi Image Light Cabinet	Alpha Innotech
Hemocytometer	C-Chip	Biochrom
Ice maker	SPR80	Nordcap
Incubator	Heracell™240i CO incubator	Thermofisher
Luminometer	Orion II	Berthold
Microscope (fluores-cence)	Axiovert200	Zeiss
Microscope (TMA)	Axioplan 2 imaging	Zeiss
Multichannel pipette	Transferpette-12 electronic	Brand
Nanodrop	Nanodrop ND-1000 UV/Vis	Thermofisher
pH-meter	pH-197	WtW
Power Supply	PowerPac ™	Biorad
RT-qPCR software	Bio-Rad CFX Connect™	Biorad
Scale	GE1302	Sartorius
SDS-PAGE chamber	Mini Trans-Blot	Biorad
Shaker	Unimax 1010 DT	Heidolph Instruments
Sterile bench	Maxisafe2020	Thermofisher
Thermocycler	T100 TM Thermal Cycler	Biorad
Thermomixer	Thermomixer comfort	Eppendorf
Vortex	Vortex-Genie 2	Scientific Industries
Waterbath	ED-5	Julabo
Western blot documen-tation	Image Studio Ver 5.2	LI-COR

3.1.5 Chemicals

Chemicals	Manufacturer
Acrylamide/Bisacrylamid	(Carl) Roth
Agar	Sigma-Aldrich
Agarose	Sigma-Aldrich
Ammonium Persulfate (APS)	Sigma-Aldrich
Ampicillin	Sigma-Aldrich
BI2536	Selleck
BI6727 (Volasertib)	Selleck
Bovine albumin (BSA)	Sigma-Aldrich
Dimethylsulfoxid (DMSO)	Sigma-Aldrich

Dithiothreitol (DTT)	Sigma-Aldrich
Doxycycline Hyclate (HPLC)	Sigma-Aldrich
Ethanol (99%)	(Carl) Roth
Glacial acetic acid	Sigma-Aldrich
Glycine	(Carl) Roth
Isopropanol	(Carl) Roth
L-glutamine	Sigma-Aldrich
LB-Medium	(Carl) Roth
Methanol (100%)	(Carl) Roth
Milk powder	(Carl) Roth
N-acetylcysteine (Nac)	Sigma-Aldrich
Resazurin	Sigma-Aldrich
Sodium Chloride (NaCl)	(Carl) Roth
Sodium dodecyl sulfate (SDS)	Sigma-Aldrich
Sodium hydroxide (NaOH)	Sigma-Aldrich
Sodium Orthovanadate (Na3VO4)	Sigma-Aldrich
Tiron (disodium 4,5-dihydroxy-1,3-benzenesulfonate) X-100	Sigma-Aldrich
TRIS-Base	Sigma-Aldrich
Tween-20	Sigma-Aldrich
0.1N HCl endotoxin free	Sigma-Aldrich

3.1.6 Biological reagents

Reagents	Manufacturer
1-kbp DNA-ladder	(Carl) Roth
100-bp DNA-ladder	(Carl) Roth
4% Formalin	Sigma-Aldrich
Accutase	Sigma-Aldrich
AEC+Substrate-Chromogen	Agilent Technologies
AgeI-HF	New England BioLabs
Beetle- and Renilla-Juice	PJK
Bovine serum albumin	Sigma-Aldrich
Bradford reagent	Biorad
Crystal violet	Sigma-Aldrich
Deoxynucleotide triphosphates (dNTPs)	Sigma-Aldrich
Dh5α competent cells	Thermofisher
DMEM with 3.7 g/l NaHCO3, with 1.0 g/l D-glucose	Biochrom
EcoRI-HF	New England BioLabs
Fetal bovine serum (Tetracycline-free)	Sigma-Aldrich
G418	InVivoGen
GeneRuler 100 bp Plus DNA Ladder	Life Technologies
GoTaq G2 Hot Start Polymerase	Promega
Hematoxylin	Vector Laboratories
HEPES	Sigma-Aldrich
Hexadimethrinbromide (polybrene)	Sigma-Aldrich

HindIII-HF	New England BioLabs
Hypotonic solution (75 mM KCl)	Merck
Immobilon Western HRP Substrate	Merck
iTaq™ Universal Probe Supermix (2X)	Bio-Rad
Lipofectamine LTX Reagent with PLUS Reagent	Invitrogen
Lipofectamine LTX with Plus Reagent	Thermofisher
Lipofectamine RNAiMax	Invitrogen
Maxima Hot Start Taq DNA Polymerase	Thermo Scientific
Maxima Hot Start Taq Polymerase	Thermo scientific
Opti-MEM Medium	Life Technologies
PageRuler Prestained Protein Ladder	Thermofisher
Penicillin-Streptomycin-Glutamine (100x)	Life Technologies
Penicillin/Streptomycin	Biochrom
Phosphate Buffered Saline (PBS)	Biochrom
Phusion High-Fidelity DNA Polymerase	Thermo Scientific
Plasmocure	InVivoGen
Propidium-iodide	Sigma-Aldrich
Protease inhibitor cocktail	Sigma-Aldrich
Puromycin	InVivoGen
Quick Start Bovine Serum Albumin Standard	Biorad
RNase	Thermofisher
RPMI 1640 with 2.0 g/l NaHCO3 500 ml	Biochrom
Stellar competent cells	Takara
Streptavidin HRP	Leica Biosystems
Sucrose > 99.5% (GC)	Sigma-Aldrich
SYBRSELECT Master Mix	Life Technologies
T4 DNA Ligase (HC)	Promega
T4 Ligase	Thermo Scientific
Target Retrieval Solution	Agilent Technologies
Trypan blue	Sigma-Aldrich
Trypsin/EDTA (10x)	Biochrom
XhoI	Thermo Scientific

3.1.7 Commercial kits

Kit	Manufacturer	Reference
FITC Amplification Kit (2 Step)	Cambio	1084-KF-50
FITC Annexin V Apoptosis Detection kit I	BD Biosciences	556547
High-Capacity cDNA Reverse Transcription Kit	Applied Biosystems	4368814
ImmPRESS Anti-Mouse IgG Polymer Detection Kit	Vector Laboratories	MP-7402
ImmPRESS anti-rabbit IgG Polymer Detection Kit	Vector Laboratories	MP-7401
NucleoSpin Gel and PCR Clean-up	Macherey-Nagel	740609
NucleoSpin RNA	Macherey-Nagel	740955
NucleoSpin Tissue/DNA	Macherey-Nagel	740952
PureYield Plasmid Midiprep System	Promega	A2495

QIAGEN Plasmid Maxi Kit	Qiagen	12162
ReliaPrep miRNA Cell and Tissue Miniprep System	Promega	Z621

3.1.8 Restriction enzymes

Name	Sequence (5'→3')	Manufacturer	Reference
AgeI-HF (20U)	ACCGGT	New England BioLabs	R3552S
EcoRI-HF (20U)	GATATC	New England BioLabs	R3195S
HindIII-HF (20U)	AAGCTT	New England BioLabs	R3104S
KpnI-HF (20U)	GGTAC	New England BioLabs	R3142S
XhoI-HF (20U)	CTCGAG	New England BioLabs	R0146S

3.1.9 Primary and secondary antibodies for Western blot and immunohistochemistry

Antibody	Manufacturer	Reference
anti-CD99	Abcam	Ab8855
anti-human mitochondria antibody	Abcam	Ab92842
anti-mouse IgG	ImmPress	MP-7402
anti-phospho-gH2AX	Abcam	Ab81299
anti-rabbit IgG	ImmPress	MP-7401
Goat polyclonal anti-mouse IgG(H+L)-HRP	Promega	W402B
Goat polyclonal anti-rabbit IgG-HRP	OriGene EU	R1364HRP
Mouse monoclonal anti-GAPDH	Santa Cruz	Sc-32233
Rabbit monoclonal anti-Ki67	Cell marque	275R-15
Rabbit polyclonal anti-Cleaved Caspase 3	Cell Signaling	9661
Rabbit polyclonal anti-PRC1	Proteintech	15617-1-AP
Rabbit polyclonal anti-PRC1	Proteintech	15617-1-AP

3.1.10 Buffer and solutions

Solution	Composition
1 M Tris-HCl; pH = 6.8	30.3g Tris up to 250 ml H 2O
1.5 M Tris-HCl; pH = 8.8	45.4g Tris up to 250 ml H 2O
1× Blotting buffer	100 ml 10 × R/B buffer; 700 ml H2O; 200 ml methanol
1× Running buffer	100 ml 10× R/B buffer; 900 ml H2O; 10 ml 10% SDS
1× TBS	100 ml 10× TBS; 900 ml H2O
1× TBST	100 ml 10× TBS; 900 ml H2O; 1 ml Tween-20
10% APS	1g ammonium persulfate; 10 ml H2O
10% SDS	10g SDS; 100 ml H2O
10× RIPA Buffer	150 mM NaCl; 1% triton X-100; 0.5% sodium deoxycholate; 0.1% SDS;50 mM Tris-HCl, pH = 8

10× Running/Blotting buffer (10× R/B buffer) (pH = 8.3)	30g Tris-Base; 144g glycine
10× TAE electrophoresis buffer	48.4g Tris-Base, 11.4 ml glacial acetic acid, 3.7g EDTA, fill up to 1L with H2O
10× TBS (pH = 7.3)	24g Tris-Base; 88g NaCl
4× Loading dye	250 mM DTT to 1 ml loading dye
Blocking buffer	5% non-fat dried milk or 5% BSA in 1x TBST
DMEM glutaMax medium	500 ml DMEM medium, 10% FCS, 1% P/S
Electrophoresis gel	100 ml 1× TAE buffer, X% agarose, 4 µl EtBr
Freezing solution	10% DMSO, 45% FCS and 45% normal medium
RPMI medium	500 ml RPMI 1640 medium, 10% FCS, 1% Penicil-

3.1.11 SDS-PAGE gel compositions

Resolving gel (7.5 ml)	**10%**
H_2O	2.9 ml
1.5 M Tris-HCl (pH = 8.8)	2ml
30% (w/v) Acrylamide/Bisacrylamid	2.5 ml
10% (w/v) SDS	75 µl
10% (w/v) APS	40 µl
TEMED	10 µl

Stacking gel (5ml)	**3%**
H2O	3.5 ml
1 M Tris-HCl (pH = 6.8)	860 µl
30% (w/v) Acrylamide/Bisacrylamid	500 µl
10% (w/v) SDS	48 µl
10% (w/v) APS	40 µl
TEMED	10 µl

3.1.12 Oligos Sequences

3.1.12.1 shRNA sequence for pLKO-Tet-On cloning

Name of Oligo	**Hairpin sequence (5' → 3')**	**TRCN-Number**
sh_Control top	CCGGCAACAAGATGAAGAGCACCAACTCGAGTT-GGTGCTCTTCATCTTGTTGTTTTT	
sh_Control bottom	AATTCAAAAACAACAAGATGAAGAGCACCAACTCGAGTTGG TGCTCTTCATCTTGTTG	
shRNA_PRC1_CDS-top	CCGGCAGGAACATTCAAAGGCATTTCTCGAGAAATGCCTTT-GAATGTTCCTGTTTTTG	0000280793
shRNA_PRC1_CDS-bottom	AATTCAAAAACAGGAACATTCAAAGGCATTTCTCGA-GAAATGCCTTTGAATGTTCCTG	

shRNA_PRC1_UTR-top	CCGGGCCTGACTTCTCTACCACATACTCGAGTATGTGGTAGA-GAAGTCAGGCTTTTTG	0000166004
shRNA_PRC1_UTR-bottom	AATTCAAAAAGCCTGACTTCTCTACCACATACTCGAG-TATGTGGTAGAGAAGTCAGGC	

3.1.12.2 Primers

Name of Oligo	Sequence (5' → 3')
RPLPO_FW	GAAACTCTGCATTCTCGCTTC
RPLPO_RV	GGTGTAATCCGTCTCCACAG
PRC1_FW	CTGCGTACTCAAATCCGAGAG
PRC1_RV	CAACCGATCCACTTCTAATTG
pGL3_PRC1_mSat_FW	CGGGGTACCGGGTCTCGCTTTCTTG
pGL3_PRC1_mSat_RV	CTAGCTAGCAGTTGCCACTTCATCCTA
EWSR1-FLI1_FW	GCCAAGCTCCAAGTCAATATAGC
EWSR1_FLI1_RV	GAGGCCAGAATTCATGTTATTGC
Tet-pLKO_FW	GGCAGGGATATTCACCATTAT
Tet-pLKO_RV	CTATTCTTTCCCCTGCACTG

3.1.12.3 CRISPR gRNA/crRNA sequences

gRNAs	Sequence (5' → 3')
sgGFP	GAGCTGGACGGCGACGTAAA
sgRNA-1	TGCAGGAAGGAAGGAAGGA
sgRNA-2	TCTTTCTTTCTATCTTGAC
crRNA-1	GTCTGTCACACCAAAACTCC
crRNA-2	ACCCGAGTACTGGTTCCCAT
ssODN-KO	gaacaggcagatatggagaatcataacatactggagcagaaaaccccat gtccagggagatgtagttattgaggggctttcgttagttttaagtccagga
ssODN-24GGAA-KI	gaacaggcagatatggagaatcataacatactggagcagaaaaccccatgg gaagaagaa-gaaggaaggaaggaaggaaggaaggaaggaaggaaggaagaagaa-gaa-gaaggaaggaaggaaggaaggaaggaatccagggagatgtagttattgaggg

3.1.12.4 3C-sequence primer/probe

Name of Oligo	Sequence (5' → 3')
PRC1-mSat-Taqman-probe	FAM-CCCAGCCATGTCTAATCTAATGAGCCC-TAMRA
PRC1-mSat-constant-fragment-RV	CACTGTAAGAGAAATGAAGAAAGCC
Test-fragment I (PRC1-promoter)	GTTTCCCTCGCTCATCCAA

Test-fragment II	AGGGATACAGAGCAGGTTCTA
Test-fragment III	TGTCACAGACATTATGAGCTGAA
Test-fragment IV	CCCTCAGGGTGTATAGTGTAGA
GAPDH loading control-FW	CTGTCTGCTTCTCTGCTGTAG
GAPDH loading control-RV	TTCACACCCATGACGAACAT
ERCC3 ligation control Taq-Man-probe	FAM-TTTACCCAGCAAGCCAGCAAGTCT-TAMRA
ERCC3 ligation control-FW	TCTTATGAAGGCTGGGAGGA
ERCC3 ligation control-RV	GGAAAGGGACTGCTGTGTAG
HindIII-test-I(PRC1-promoter) cut-FW	GTTTCCCTCGCTCATCCAA
HindIII-test-I(PRC1-promoter) cut-RV	ACTCAATGTTCCTTCCCTTCC
HindIII-test-I (PRC1-promoter) un-cut-FW	CCAAGCCAGCTACCTCATC
HindIII-test-I (PRC1-promoter) un-cut-RV	ACTCAGGGAAGCCAGGTA
HindIII-test-II cut-FW	AGGGATACAGAGCAGGTTCTA
HindIII-test-II cut-RV	GTATTGTGGAATTGTGCGAAGAG
HindIII-test-II uncut-FW	GTGAGGCCCTGTCTCAAATAA
HindIII-test-II uncut-RV	TTCCCTAGAGTCCTGTCCTTAG
HindIII-test-III cut-FW	TGTCACAGACATTATGAGCTGAA
HindIII-test-III cut-RV	GCTGCTCAAAGGAGGAAAGA
HindIII-test-III uncut-FW	TGGTCAGCCAATCGTTTCTAC
HindIII-test-III uncut-RV	TGACCTCTCTTTCTTGCCATTT
HindIII-test-IV cut-FW	CCCTCAGGGTGTATAGTGTAGA
HindIII-test-IV cut-RV	TTTATGTGTGTGTGTATGTGTGTG
HindIII-test-IV uncut-FW	GCCTCTCAGGCTCAAGTAATC
HindIII-test-IV uncut-RV	GCGAGACCCTGTCTCTACTAA

3.1.12.5 Primers for sequencing

Name	Sequence (5' → 3')
pGL_primer2	CTTTATGTTTTTGGCGTCTTCCA
pLKOseq_FW	GGCAGGGATATTCACCATTATCGTTTCAGA
pLKOseq_RV	GACGTGAAGAATGTGCGAGA
RVprimer3	CTAGCAAAATAGGCTGTCCC

3.1.13 Vectors

Vector name	Number	Manufacturer
pCAG-YFP	# 11180	Addgene
pCEF-VSV-G (*env*)	# 41792	Addgene
pCMV-GFP	# 11153	Addgene
pGL3-Promoter Vector	# E1761	Promega
pHAGE TRE dCas9-KRAB	#50917	Addgene
pLKO.1-puro U6 sgRNA BfuAI large stuffer	# 52628	Addgene
psPAX2	# 12259	Addgene
Tet-pLKO-puro	# 21915	Addgene

3.1.14 Software

Software	Manufacturer
BD Accuri C6 Software	BD Biosciences
Bio Rad CFXManager 3.1	Biorad
Cytoscape 3.8.1	Cytoscape
GraphPad PRISM 8	GraphPad
Image J	www.rsbweb.nih.gov/ij/
Image Studio Lite	LI-COR
Photoshop 2020	Adobe
R-project	https://www.r-project.org/
SnapGene	GSL Biotech
SPSS	IBM

3.2 Methods

3.2.1 Microbiology

3.2.1.1 pGL3-promoter vector establishment

To evaluate whether EWSR1-FLI1 interacts with a distal enhancer-like GGAA-mSat about 90kb telemetric away from *PRC1* promoter, 1,053 bp fragment including *PRC1*-associated GGAA-mSats (hg19 coordinates: chr15:91,623,953-91,625,005) from three EwS cell lines (A673, TC71 and EW-1) were inserted into the pGL3-Fluc vector (Promega, #E1761). The backbone vector was linearized via double digestion (KpnI and NheI) at 37°C for 3 hrs (**Table 1)**. A673, TC71 and EW-1 genome DNA (gDNA) were extracted according to NucleoSpin Tissue kit manual instruction and adjusted to a final concentration of 100 ng/µl.

Name	Volume (µl)
pGL3-Promoter vector (1µg)	Variant
10× CutSmart buffer	10
KpnI	1
NheI	1
dH_2O	Up to 50 µl

Table 1 pGL3-Promoter vector linearization

Primers were specifically designed by Primer Premier and BLAT in UCSC (https://genome.ucsc.edu/cgi-bin/hgBlat) to check specificity in hg genome. An In-Silico PCR has been performed via UCSC In-Silico PCR tool (https://genome.ucsc.edu/cgibin/hgPcr?hgsid=879734033_fYCe8o5jbApFjbAp-FxKk8yA87GWs), which yields desired PCR amplicon without any non-specific amplification. The target mSat-amplicon was amplified from pre-diluted gDNA (100 ng) by using corresponding primer pair with overhangs. PCR amplification program was set up in **Table 2**.

Name	Volume (µl)
Phusion HF buffer (5X)	10
pGL3_PRC1_mSat-FW (10 µM)	2.5
pGL3_PRC1_mSat-RV (10 µM)	2.5
Phusion HF polymerase	0.5
gDNA (100 ng/µl)	1
dNTP (10 mM)	1
DMSO	1.5
dH_2O	= up to 50

Table 2 Recipe of mSat amplification from gDNA

A touch-down (TD) PCR was used in order to avoid non-specific amplification (**Table 3**). The annealing temperature (T_a) of mSat primer pair was calculated via NEB Tm calculator online tool (https://tmcalculator.neb.com/#!/main). The start annealing temperature of TD-PCR was 5°C higher than the actual T_a value, with a gradient cooling process (-0.5°C/cycle) for 10 cycles. The last 25 cycles of PCR amplification were annealed at the actual T_a value. Elongation time was determined according to the length of the desired amplicon.

Step	°C	Time	Cycles
Initialization	98	30 sec	1
Denaturation	98	10 sec	1-10th
Annealing	55-0.5°C /cycles	30 sec	
Elongation	72	30 sec	
Denaturation	98	10 sec	11th-35th
Annealing	50	30 sec	
Extension	72	30 sec	
Final Extension	72	10 min	

Table 3 PCR amplification program for Phusion-mediated mSat-PCR- amplification

The right band was cut and extracted with the NucleoSpin PCR and Gel clean up kit. Extra variants devoid of the GGAA-mSat was excluded by whole genome sequencing (WGS) of the parental cell lines and Sanger sequencing of the cloned fragments. Sequenced mSat fragment was ligated to digested pGL3-promoter vector (50 ng) with T4 ligase (NEB) in a molar insert : vector ratios of 5:1. The required mass of insert for the indicated ratio was calculated via NEB ligate calculator (http://nebiocalculator.neb.com/#!/ligation) (**Figure 7**).

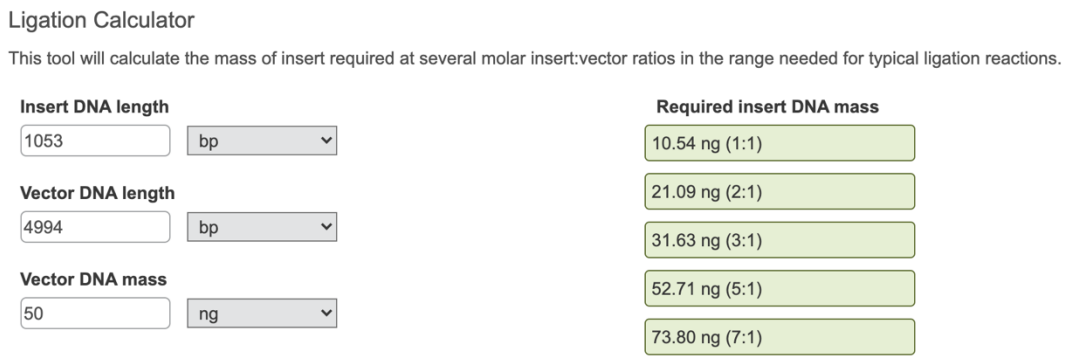

Figure 7 Calculation of the mass of mSat insert

Calculation of the mass of mSat insert needed for linearized pGL3-promoter vector (http://nebio-calculator.neb.com/#!/ligation).

55 ng mSat fragment was ligated to 50 ng linearized pGL3-promoter vector in a 20 µl ligation system at 16°C overnight (**Table 4**).

Components	Sample	Neg. Ctrl
Insert	x µl mSat-fragment (55 ng)	X µl ddH2O
Linearized backbone vector	50 ng	50 ng
Ligation buffer (10X)	2 µl	2 µl
T4 ligase (400 U/µl)	1 µl	1 µl
dH_2O	= up to 20 µl	= up to 20 µl

Table 4 Ligation reactions of mSat fragment with pGL3 backbone

An extra heating step (65°C, 10 min) was carried out for enzyme inactivation. The cloned pGL3-mSat vector is showed in **Figure 8**.

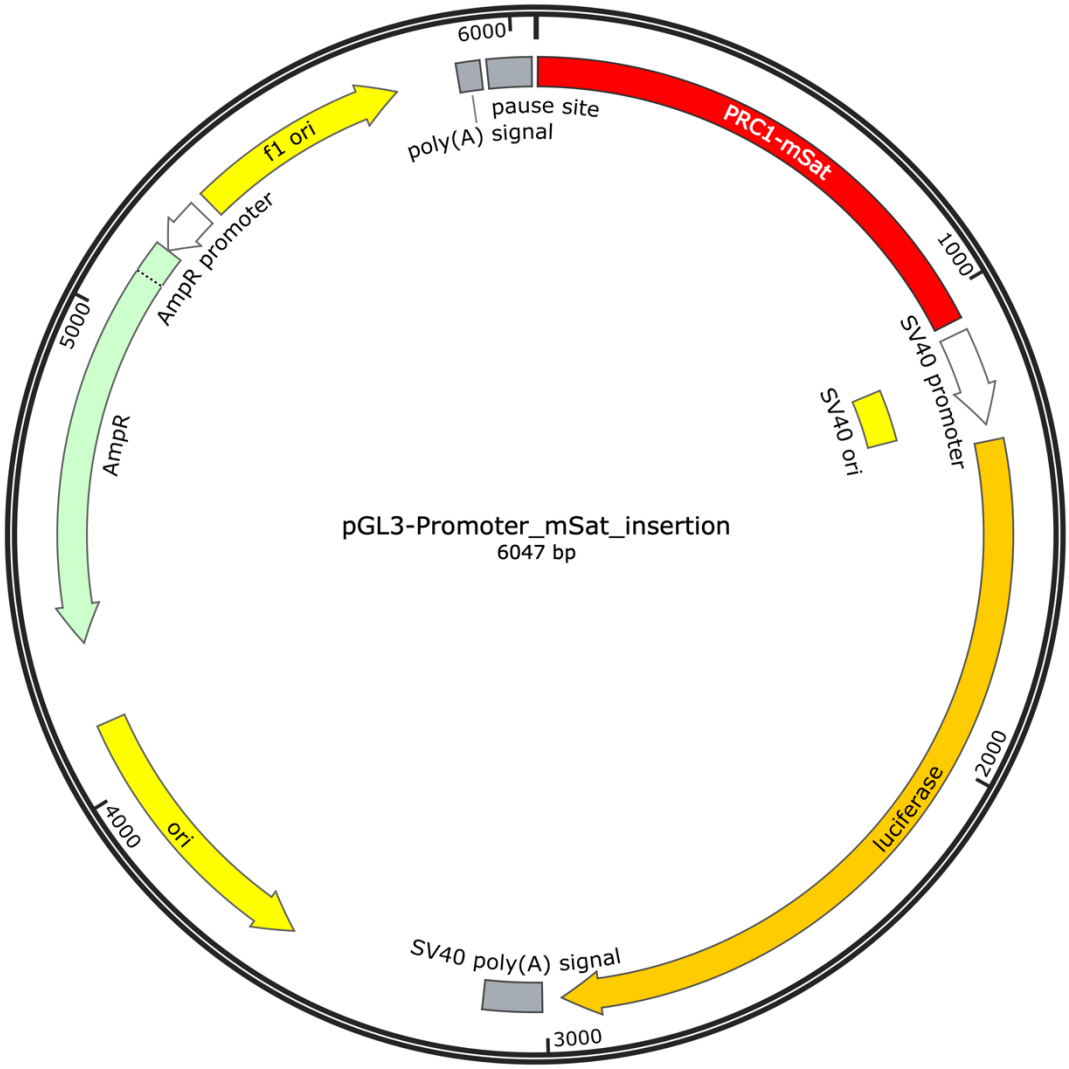

Figure 8 Cloning with the pLKO-Tet-On system

3.2.1.2 pLKO-Tet-On system establishment

In order to establish *PRC1* stable knockdown cell lines, the pLKO-Tet-On system for inducible shRNA expression was used [82]. The cloning was carried out according to Wiederschain 's protocol [83] [Addgene (Plasmid # 21915)].

shRNA sequences with corresponding restriction overhang used in the pLKO-Tet-On vector were listed in **Table 5**. "Genetic Perturbation Platform (GPP) Web Portal" from the Broad institute was used for sequence designing. A scrambled sequence was used for the control (**Table 5**).

	AgeI	Target sequence	XhoI	Target sequence	Term. signal	EcoRI	
shPRC1_CDS:							
Top	CCGG	CAGGAACATTC AAAGGCATTT	CTCGAG	AAATGCCTTTGAA TGTTCCTG	TTTTTG		
		AAATGCCTTTG AATGTTCCTG	CTCGAG	CAG– GAACATTCAA AGGCATTT	CAAAAA	AATT	bot-tom
shPRC1_UTR:							
Top	CCGG	GCCTGACTTCTC TACCACATA	CTCGAG	TATGTGGTAGAG AAGTCAGGC	TTTTTG		
		TATGTGGTAGAG AAGTCAGGC	CTCGAG	GCCTGACTTCTC TACCACATA	CAAAAA	AATT	bot-tom
sh_Control:							
Top	CCGG	CAACAAGATGAA GAGCACCAA	CTCGAG	TTGGTGCTCTTCA TCTTGTTG	TTTTTG		
		TTGGTGCTCTTCA TCTTGTTG	CTCGAG	CAACAAGATGAA GAGCACCAA	CAAAAA	AATT	bot-tom

Table 5 Sequences of shRNAs against *PRC1* or control.

A double digestion was performed by using AgeI and EcoRI restriction enzymes in the Tet-pLKO-puro vector (**Table 6**):

Name	Volume (µl)
CutSmart buffer (10X)	2
AgeI	2
EcoRI	2
4 µg Tet-pLKO-puro vector	variant
dH_2O	Up to 20

Table 6 Linearization of Tet-pLKO-puro vector

Plasmid digestion was performed following the NEB manual instructions by mixing digestion solutions together to double their final yield. The digested vector backbone was collected via sodium acetate/ethanol precipitation and reformulated with dH_2O. The vector has been verified by gel (about 8800 bp for linearized vector) and was cut for purification.

Before ligation, shRNA was first annealed. Forward and Reverse oligo were reconstituted in ddH_2O in a final concentration of 100 µM. 11.25 µl of each 100 µM

primers were pooled together and 2.5 µl 10X annealing buffer was added to the mixed primer solution in a PCR-tube. An annealing process was described in **Table 7**.

Step	°C
Start temperature	95
Annealing	-1°C /min
End temperature	14°C

Table 7 Oligo annealing

Dilute 1 µl of the primer mixture 1:400 in 0.5X annealing buffer. Digested backbone vector and annealed shRNA was ligated at 16°C for 16 h (**Table 8)**:

Name	Volume (µl)
Gel-purified digested pLKO-Tet-On (10-20 ng)	variant
Oligo dilution	1
10X Ligase buffer	1.5
T4 DNA ligase	1
dH_2O	up to 15

Table 8 Ligation reaction of cloned Tet-pLKO-puro vector

The cloned Tet-pLKO-puro vector is noted in **Figure 9**.

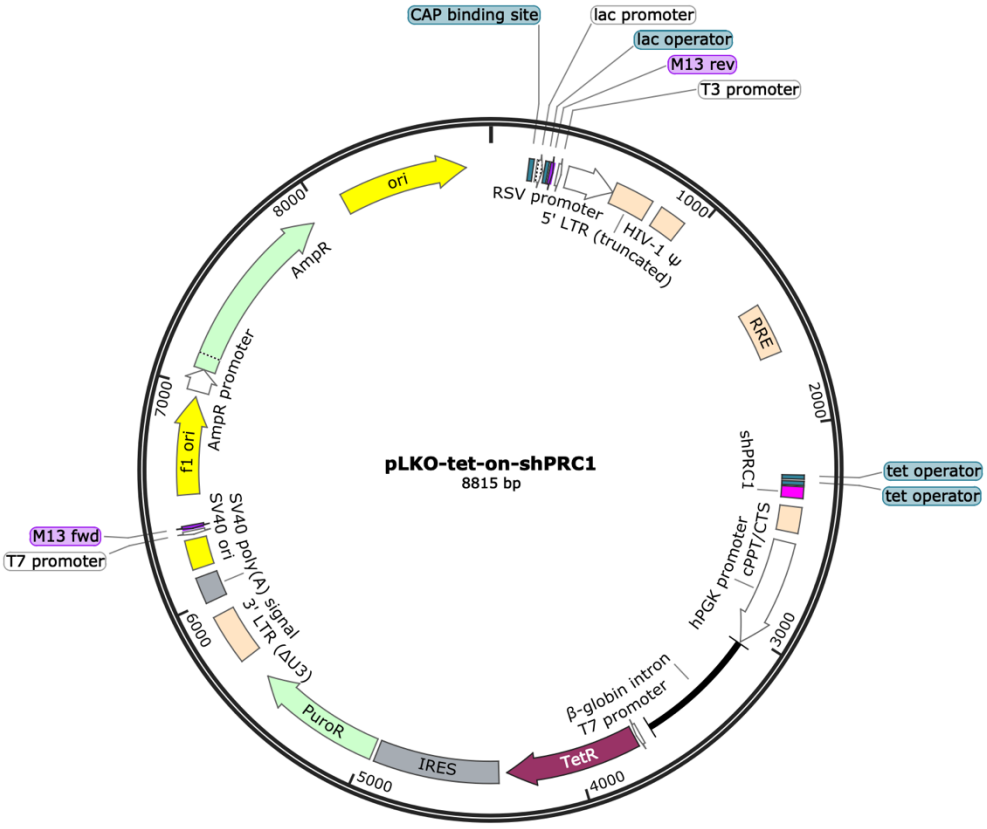

Figure 9 Vector map of cloned Tet-pLKO-puro

3.2.1.3 Transformation and clone verification

Transform Stellar Competent cells (50 µl) with 4 µl of the total ligation reaction volume in 1.5 ml Eppendorf tube followed the manual instruction (https://www.takarabio.com/documents/User%20Manual/PT5055/PT5055-2.pdf). Briefly, pre-chill ligation on ice for 30 min, heat shock for exactly 45 sec at 42°C, and incubate on ice for 2 min. Add 500 µl pre-warmed SOC-medium to the stellar competent cells and incubate at 37°C while shaking for 1.5 h. Plate 100 µl of *E.coli* cells onto pre-warmed LB plates (Amp 100 µg/ml) for an overnight incubation at 37°C with shaking.

The colony touch-down (TD) PCR was performed to verify the right clones. Pick single colonies and incubate in 100 µl LB-Medium (100 µg/ml ampicillin) for 2 h while shaking at 37°C.

Name	Volume (µl)
Gotaq green buffer (5X)	10
dNTPs (10 mM)	1
MgCl (25 M)	6
10 µM FW primer	2.5
10 µM RV primer	2.5
Gotaq polymerase	0.25
Colony solution	3
dH_2O	up to 50
Total volume	50

Table 9 Components of colony PCR

The colony-PCR mix is shown in **Table 9**:

For pGL3-mSat, Tet-pLKO_shPRC1/shCtrl vectors, the following primers were included:

pGL3 primers:

pGL3_mSat_FW: 5'-CGGGGTACCGGGTCTCGCTTTCTTG-3'

pGL3-mSat_RV: 5'-CTAGCTAGCAGTTGCCACTTCATCCTA-3'

pLKO primers:

Tet-pLKO_FW: 5'- GGCAGGGATATTCACCATTAT–3'

Tet-pLKO_RV: 5'- CTATTCTTTCCCCTGCACTG–3'

The colony-PCR program has a longer initialization time, as the bacterial membrane should be completely destroyed first to expose the plasmid. The PCR-program was set up in **Table 10**:

Step	°C	Time	Cycles
Initialization	95	10 min	1
Denaturation	98	10 sec	1- 10th
Annealing	X*	30 sec	
Elongation	72	1 min	
Denaturation	98	10 sec	11th - 30th
Annealing	X**	30 sec	
Extension	72	1 min	
Final Extension	72	∞	

Table 10 Protocol of colony-PCR program

X*: The Ta for first 10 cycles should be adjusted on Tm of primer pairs and the DNA polymerases used in PCR-process: For pGL3_mSat vector: T_a = 55-50°C; Tet-pLKO_shPRC1/shCtrl vector: T_a = 59-49°C.

X**: The Ta for the rest 20 cycles is the actual annealing temperature of the primer pairs used: For pGL3_mSat: 49°C; For Tet-pLKO_shPRC1/shCtrl vector: 56°C.

Resolve PCR products on 1.5% agarose gel: mSat insert = 1053 bp, shPRC1/shCtrl insert: 420 bp.

Inoculate midiprep cultures in 100 ml LB/Amp medium (100 µg/ml) at 37°C over-night with constant shaking (350 rpm).

3.2.1.4 pGL3-mSat and Tet-pLKO-shPRC1/shCtrl Sanger sequencing

Sanger sequencing was carried out by using corresponding sequence primers to exclude potentially introduced point mutation during transformation with *E.coli*. The primers for sequencing were formulated to 10 µM with dH_2O. Plasmid was adjusted to 75 ng with dH_2O (30 µl).

3.2.2 Cell Culture

3.2.2.1 Cell lines

Ewing Sarcoma

A673, RDES, SK-N-MC, TC32, EW1 and TC71.

The A673/TR/shEF1 was established by Dr. med. Martin Orth.

Others

HEK-293 (Human embryonic kidney cell line)

EwS cell lines were listed in **Table 11**.

Cell line	Description
A673	Established from the primary tumor of a 15-year-old girl [84]
RDES	Established from humerus of a 19-year-old man
SK-N-MC	Established in 1971 of a 14-year-old Caucasian female with an Askin's tumor
EW1	Established from the tumor of a 17-year-old man
TC32	Established from the tumor of a 17 years old female [85]
TC71	Established from the tumor of a 22-year-old man with metastatic Ewing sarcoma

Table 11 Description of EwS cell lines used.

3.2.2.2 General cell culture

RPMI-1640 or DMEM medium including 10% tetracycline-free fetal calf serum (FCS) and 100 U/ml Penicillin and 100 µg/ml Streptomycin (P/S) were selectively used for normal cell culture depending on cell lines. Cells were growing in humidified incubator at 37°C (5% CO_2). About 1 × 10^6 cells/ml were frozen at -80°C for a short-term and in liquid nitrogen for long-term storage by adding 1 ml freezing medium (10% Dimethyl Sulfoxide (DMSO), 45% FCS and 45% normal culture medium) to the cell pellet.

When cells were confluent, cells were passaging by washing with PBS 1X and trypsinized. Mycoplasma test was performed regularly by nested PCR every 3 months. Short Tandem Repeat (STR)-profiling was carried out every half year.

3.2.2.3 Establishment of Doxorubicin-resistant EwS cells

Doxorubicin-resistant (Doxo-res) EwS cells (A673 Doxo-res and TC71 Doxo-res) were established through continuous culture with serially increasing Doxo concentrations starting at ~10 nM corresponding to pre-determined 50% inhibitory concentration (IC50) values. After the successfully adaptation to the given concentrations indicated by re-growth, cells were cultured with serially ascending Doxo concentrations by multiplying the IC50 values by factor 1.1–2.0. Doxo-res variants were maintained with ~200 nM Doxo.

3.2.2.4 Lentivirus transfection and transduction

5 × 10^6 HEK-293T cells were seeded in 10 ml DMEM-glutaMAX medium (10% FCS and 1% P/S) one day before transfection.12 µg DNA plasmid, 9 µg psPAX2 and 3 µg VSV-G were mixed to OptiMEM and the transfection was done followed the Lipofectamine LTX (Thermo Fisher) manual instruction. Old medium was replaced by 10 ml virus harvest medium (DMEM-GlutaMAX + 30% FCS + 15 mM HEPES w/o P/S) 6 h after transfection in order to reduce toxicity and accelerate virus production. 48 h after transfection, the virus supernatant was gathered by spinning down at 500 g for 10 min to get rid of debris. The virus supernatant was then filtered via 0.45 µm filter and stored at 4°C temporarily. 5 ml fresh pre-warmed virus harvest medium was added gently to the flask for the 2nd virus production. 2nd virus supernatant was collected and treated as mentioned above and mix with the 1st virus supernatant together. The pooled virus supernatants were condensed 20X via Lenti-Concentrator and the virus pellets were resuspended with cold PBS.

At the same time 5 × 10^5 cells/ T25 flask were pre-cultured 24 h before transduction in normal cell culture medium. 500 µl concentrated virus supernatant was added to 2.5 ml DMEM-GlutaMAX complete medium (10% FCS + 1% P/S) containing polybrene (8 µg/ml). Polybrene was removed 8 h after transduction by replacing with normal complete medium. The cells were then incubated for 72 h. Successfully transduced cells containing antibiotic-resistance cassette were selected by using proper antibiotics.

3.2.2.5 CRISPR interference

The pLKO.1-puro U6 sgRNA BfuAI large stuffer plasmid (#52628) was used for expressing sgRNA. The pHAGE TRE dCas9-KRAB lentiviral plasmid (#50917) encodes dCas9-KRAB fusion protein. Candidate sgRNAs were designed by searching for G(N)20GG motifs 150 bases upstream/downstream of the *PRC1*-associated GGAA-mSat. Relevant off-target matches were determined and ruled out by CRISPR-Cas9 guide RNA design checker (IDT). SgRNAs were then cloned individually in the digested pLKO.1-puro U6 sgRNA BfuAI large stuffer plasmid and verified by Sanger-sequencing (**Figure 10**). Lentivirus was produced as described above (see **3.2.2.4**). A673 and RDES cells were first transduced

with pHAGE TRE dCas9-KRAB plasmid and selected with G418 (800 µg/ml). Cells stably expressing dCas9-KRAB protein (**Figure 11**) were then transduced with pLKO.1-sgRNA lentiviral particles and treated with puromycin (1 µg/ml) and G418 (400 µg/ml) to select and maintain successfully transduced cells. An sgRNA targeting the Green fluorescent protein (GFP) gene was used as the negative control.

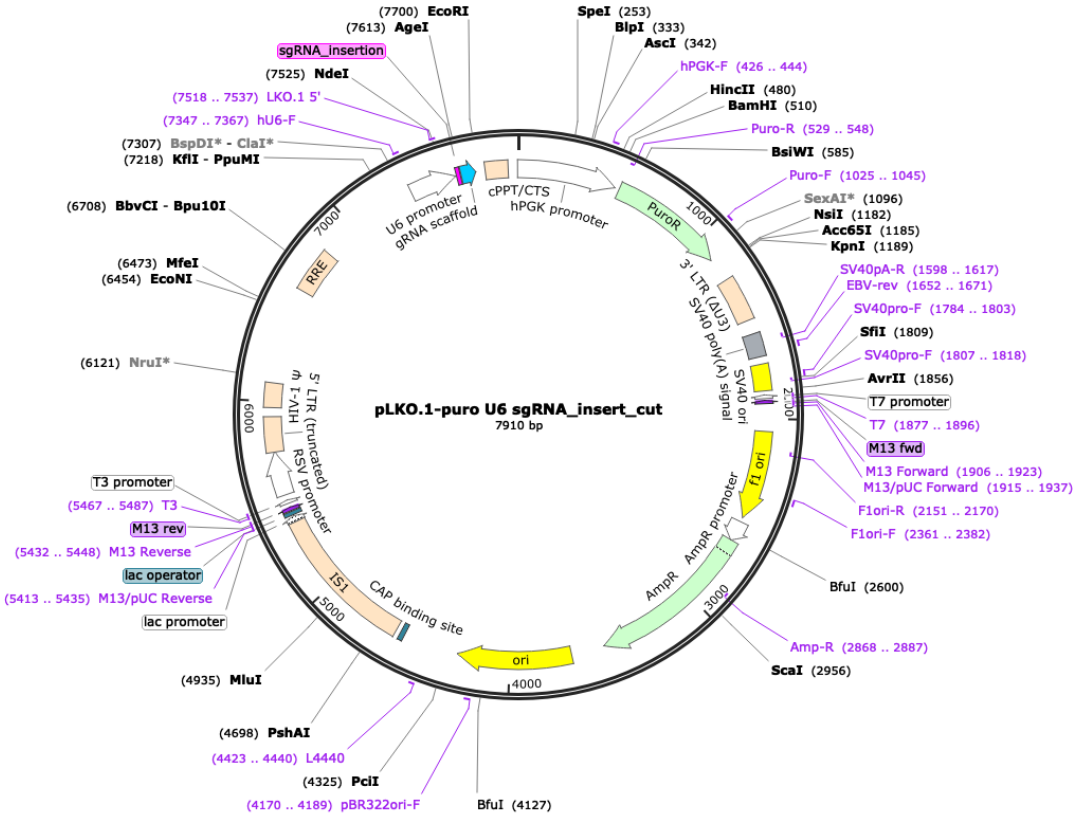

Figure 10 The pLKO.1-puro U6 sgRNA BfuAI large stuffer lentiviral plasmid backbone with sgRNA as insert

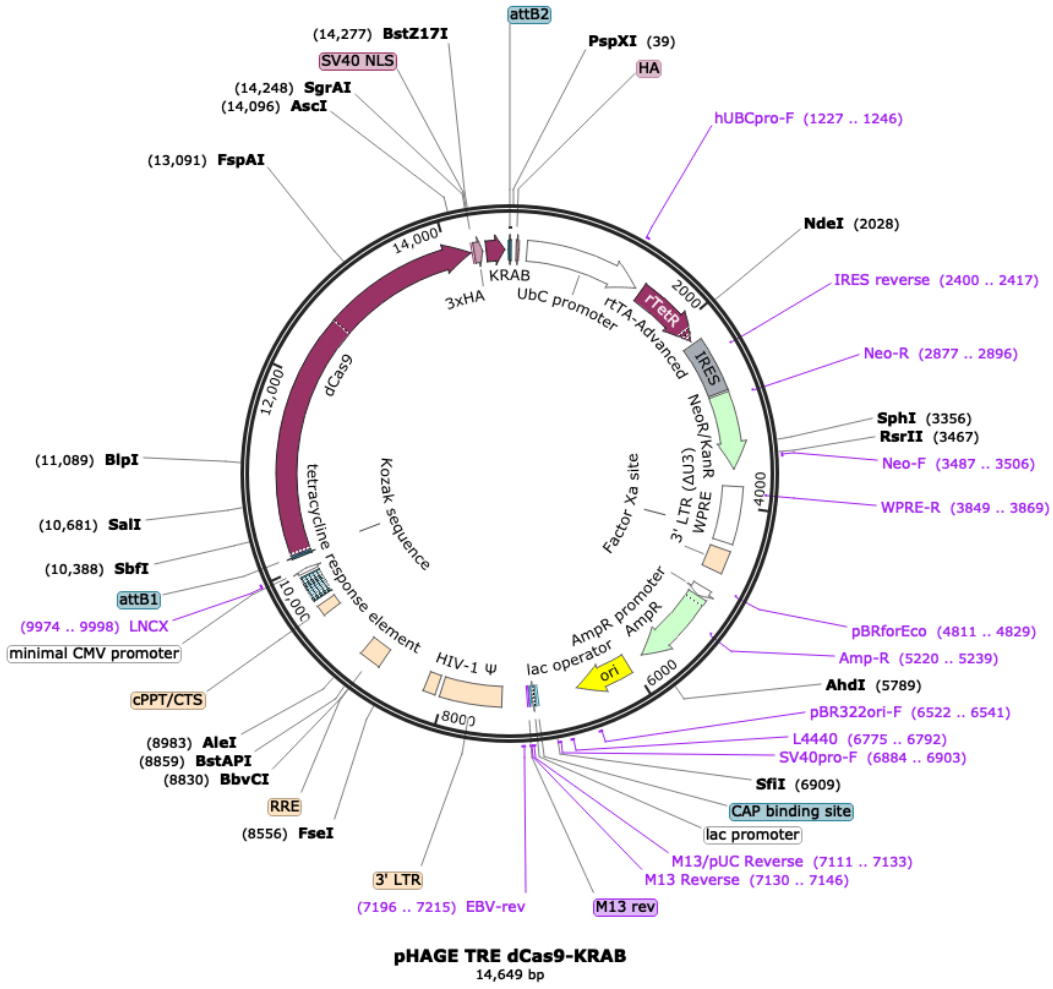

Figure 11 The pHAGE TRE dCas9-KRAB lentiviral plasmid encoding dCas9-KRAB

3.2.2.6 CRISPR-Cas9 homology-directed repair editing

Publicly available gRNA design tool from IDT (https://eu.idtdna.com/site/order/designtool/index/CRISPR_CUSTOM) was used to identify high-scoring candidates gRNAs complementary to two target regions flanking the *PRC1*-associated GGAA-mSat motifs (**Figure 12**).

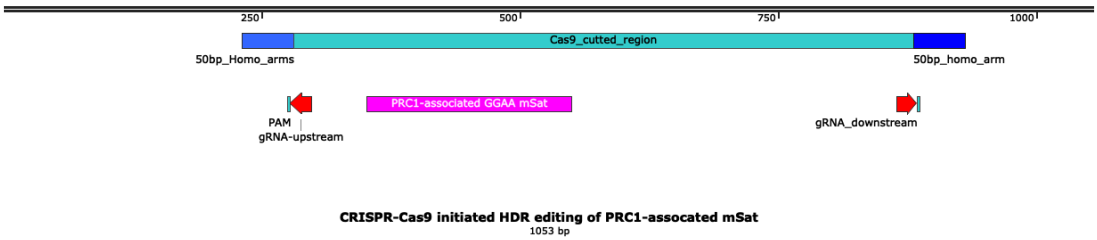

Figure 12 Representative map of CRISPR-Cas9 cutting position in *PRC1*-associated mSat.

Each crRNA (CRISPR RNA) (IDT, Alt-R CRISPR-Cas9 crRNA, custom design) was mixed with tracrRNA (trans-activating crRNA) (IDT, Alt-R CRISPR-Cas9 tracrRNA) in equimolar concentrations to form crRNA:tracrRNA duplexes (10 µM). The crRNA:tracrRNA duplexes were heated at 95°C and gradually cooled down to room temperature (RT) (20-25°C). The up- and downstream RNA complexes were mixed in equimolar concentrations and then incubated with Cas9 HIFI V3 nuclease (IDT, Alt-R S.p. HiFi Cas9 Nuclease V3, #369268) for 5 min at room temperature to assemble the RNP complex. A negative control (ctrl) ctRNP was established at the same time (IDT, Alt-R Cas9 Negative Control). Ultramer ssODN donor of either homologous arms alone (50 bp up- and downstream) or homologous arm plus a 24-GGAA-insert (196 bp) was added to the RNP complex individually and incubated for 5 min at RT to generate the RNP mixture (ssODN final concentration 4 µM). The RNP mixture was added to diluted CRISPR MAX reagent (Invitrogen) to generate the RNP lipid complex of a final concentration of 90 nM. The ctRNP transfection solution was then incubated for 13 min at RT. EwS cells were synchronized in the G2/M phase via incubation with Nocodazole for 16 h (200 ng/ml) followed by a release of 1 h release before transfection. 50 µl of the ctRNP transfection solution were added to 100 µl synchronized cell suspension (40,000 cells) with HDR enhancer (final concentration 30 µM) (IDT, Alt-R® HDR Enhancer) seeded in triplicates in 96-well plates. Transfected cells were incubated at 37°C (5% CO_2) and the medium from cells was replaced by fresh medium without HDR enhancer after 24 h. Genomic DNA isolation and detection of editing efficacy at bulk level were performed 48 h after transfection by assessment of the fluorescence intensity, and by PCR amplification and gel-electrophoresis. Finally, single-cell cloning was carried out to select successfully edited clones, which were verified by Sanger-sequencing (**Figure 13**).

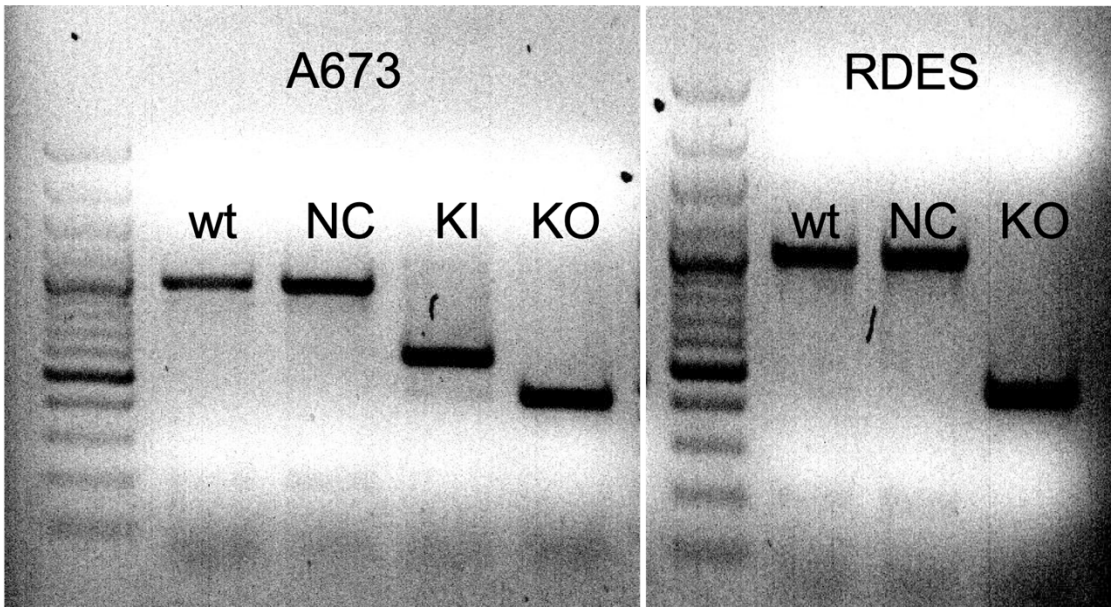

Figure 13 CRISPR-modified mSat gel image

Representative images of agarose gel electrophoresis of amplicons containing the wildtype (wt) PRC1-associated GGAA-mSat, CRISPR Cas9-edited negative control (NC), or CRISPR Cas9-initiated HDR edited KO of A673 and RDES cells, as well as the insertion of 24-GGAA repeats in A673 cells (100 bp DNA ladder).

3.2.3 Molecular biology

3.2.3.1 Reverse transcription, and quantitative RT-PCR

High-Capacity cDNA Reverse Transcription Kit was used for cDNA synthesis (**Table 12**):

Name	Volume (µl)
RT buffer (10X)	2
Random primers (10X)	2
dNTP Mix (100 mM)	0.8
Reverse Transcriptase (50 U/µl)	0.8
RNA diluted with dH_2O	14.4

Table 12 cDNA synthesis components.

The qRT-PCR reactions were performed using 'SYBR green master mix' (**Table 13**) with Bio-Rad CFX Connect instrument. Data analysis was carried out by using Bio Rad CFX Manager 3.1 software.

Name	Volume (µl)
SYBR green master mix (2X)	10
10 µM FW/RV primer mix	1.0
Diluted cDNA	9.0

Table 13 qRT-PCR with SYBR dye

Gene expression values were calculated using the "2^−(ΔΔCt) method" [86]. *RPLP0* was used as internal control.

The qRT-PCR reaction was set up as follows (**Table 14**):

Step	°C	Time	Cycles
Heat activation	95	2 min	1
Denaturation	95	10 sec	50
Annealing	60	20 sec	
Extension	60	20 sec	
Final denaturation	95	30 sec	1

Table 14 qRT-PCR with SYBR dye program

3.2.3.2 DNA extraction and RNA extraction,

1×10^7 cells were extracted with the NucleoSpin Tissue/DNA or RNA kit according to manual instructions. DNA or RNA concentration was measured by Nanodrop.

3.2.3.3 Chromatin conformation capture (3C) PCR assays

In order to check if heterogenous expression of *PRC1* in EwS can be mediated through long-range direct physical interactions of EWSR1-FLI1 between *PRC1* promotor via binding to a distant GGAA-enhancer like mSat, chromosome conformation capture (3C) PCR assays were performed to test such looping interactions.

The 3C PCR-seq was carried out as previously described with minimal modifications [87]. Briefly, 1×10^7 cells were fixed with 1% formaldehyde in PBS/10% FCS and incubated for 10 min at RT while tumbling. This cross-linking was inactivated by glycine (125 mM) and washed with PBS. Fixed cells were lysate in a pre-cold lysis solution (10 mM Tris, pH 8.0, 10mM NaCl, 0.2% NP40 and a protease inhibitor cocktail [Roche]) under constant shaking for 15 min. The formaldehyde-crosslinked nuclei were harvested and washed with 1.2X RE buffer and then re-suspended into 0.5 ml 1.2X RE buffer with addition of sodium dodecyl sulfate

(SDS) (0.3%). The mixture was incubated for 20 min at 65°C followed by 40 min at 37°C with shaking at 1,200 rpm. The solution containing 2% Triton X-100 was further incubated for 1 h at 37°C with shaking at 1,200 rpm. The DNA was first digested with 400 U HindIII-HF (NEB) for 6 h at 37°C (1,200 rpm). Another 400 U HindIII-HF was used for a second digestion at 37°C overnight (1,200 rpm). After collection of the digested solution, the solution was diluted in 7 ml 1X ligation buffer. Then, the solution/1% Triton X-100 was incubated at 37°C for 1 h while gently shaking. Next, DNA was ligated with 100 U T4 DNA Ligase (HC) (Promega) for 4 h at 16°C and then for 45 min at RT. Crosslinks were reversed by 300 µg proteinase K for an overnight incubation at 65°C. Residual RNAs in the sample were digested by RNase A. DNA was purified by phenol-chloroform extraction and dissolved in 100 µl of 10 mM Tris (pH 7.5).

Perform real-time PCR quantifications (SYBR Green) on both samples (undigested and digested) using the qPCR conditions detailed in **Table 15,16**. Digestion efficiencies were monitored by SYBR qPCR with primer pairs that amplify genomic regions containing or devoid of HindIII digestion sites. The digestion efficiency should be above 60–70%.

Component	Volume	Final concentration
H_2O	6 µl	
Forward primer (10 µM)	1 µl (10 pmol)	0.5 µM
Reverse primer (10 µM)	1 µl (10 pmol)	0.5 µM
SYBY master mix (2X)	10 µl	
50X dilution of 3C sample	2 µl	

Table 15 Set up 20 µl qPCRs for 3C sample digestion efficacy test.

Step	Temperature	Duration	Cycles
UDG Activation	50°C	2 min	Hold
AmpliTaq® Fast DNA polymerase, UP Activation	95°C	2 min	Hold
Denature	95°C	15 sec	40
Anneal/Extend	60°C	1 min	

Table 16 Thermal cycling conditions using SYBER-dyed for digestion efficacy test.

TaqMan real-time PCR was carried out for quantification of ligation products (**Table 17, 18)**. A random ligation control was generated using a bacterial artificial

chromosome (BAC; clone CH17-26I20, CHORI BACPAC Resources Center) harboring all ligation products under study. The ligation frequency was calculated as a ratio of the 3C ligation product to the corresponding product in the random ligation control by normalization with *ERCC3* [87].

Component	Volume	Final concentration
H_2O	2 µl	
Test primer (10 µM)	0.5 µl (5 pmol)	0.5 µM
Constant primer (10 µM)	0.5 µl (5 pmol)	0.5 µM
iTaq™ Universal Probe Supermix (2X)	5 µl	
TaqMan probe (1.5µM)	1 µl (1.5 pmol)	0.15 µM
3C sample (200 ng/µl)	1 µl	

Table 17 10 µl qPCRs system for ligation frequency of 3C samples

Step	Temperature	Duration	Cycles
Polymerase Activation & DNA Denaturation	95°C	3 min	Hold
Denaturation	95°C	5 sec	40
Anneal/Extend + Plate read	60°C	30 sec	

Table 18 10 µl qPCRs system for ligation frequency of 3C samples.

3.2.4 Biochemistry

3.2.4.1 Protein preparation and quantification

5×10^5 cells were seeded in 6-well plate treated with/without Dox (1µg/ml) for 72 h to induce *PRC1* knockdown. Whole cellular proteins were collected with 100 µl RIPA buffer including 1 mM Na_3VO_4 and 100 µl/ml protease inhibitor cocktail. Bradford protein assay was used for protein concentration measurement [88].

3.2.4.2 Western blotting

Proteins were separated on a 10% gel, and blotted on PVDF membranes. Membranes were incubated with rabbit polyclonal anti-PRC1 antibody (1:1,000, 15617-1-AP, Proteintech) or mouse monoclonal anti-GAPDH (1:800, sc-32233, Santa Cruz). Then, membranes were incubated with horseradish peroxidase

(HRP) coupled anti-rabbit IgG (H+L) (1:5,000, R1364HRP, OriGene) or anti-mouse IgG (H+L) (1:3,000, W402B, Promega). Proteins were detected using chemiluminescence HRP substrate (Millipore-Merck).

3.2.5 *In vitro* assays

3.2.5.1 Proliferation assay

2×10^5 EwS cells harboring dox-inducible shRNA against *PRC1* or CRISPR Cas9-initiaed HDR-edited EwS cells were seeded in 6-well plates. 1 µg/ml Dox was used for inducing *PRC1* knockdown for 72 h and refreshed every 48 h. A673/TRE/dCas9/sgPRC1 or sgGFP and RDES/TRE/dCas9/sgPRC1 or sgGFP cells were treated with/without Dox (2 µg/ml) for 14 d with regular media changes (Dox refreshed every 48 h). Cells (including supernatant) was counted within standardized hemocytometers (C-Chip, Biochrom) using the Trypan-Blue (Sigma-Aldrich) exclusion method.

3.2.5.2 Colony forming assay (2D/3D)

For 2D Colony forming assay, 300 cells of RDES, SK-N-MC, and TC32 cells harboring Dox-inducible shRNAs against *PRC1* and respective control/ RDES and TC32 EwS cells treated with indicated dose of PLK1 inhibitors (BI2536 or BI6727) were seeded and cultured in triplicates in 12-well plates for 12–16 d. Dox (1 µg/ml) was used for *PRC1* knockdown and refreshed every 48 h. Thereafter, Crystal-Violet solution (Sigma-Aldrich) was used for colony staining. ImageJ Plugin Colony area was used for colony number/size measurement. The clonogenicity index was calculated as: colony number X colony area.

For 3D sphere formation assay, 500 cells of RDES, SK-N-MC, and TC32 cells harboring Dox-inducible shRNAs against *PRC1* and respective control/ RDES and TC32 EwS cells treated with indicated dose of PLK1 inhibitors (BI2536 or BI6727) / CRISPR Cas9-initiated HDR edited A673 cells were in 96-well Costar Ultra-low attachment plates (Corning) in 100 µl standard cell culture for 14 d. For shRNA-mediated EwS cells, 10 µl of fresh medium with/without Dox was applied to each well every 48 h. PLK1 inhibitor at indicated doses were applied to RDES and TC32 cells when seeding without any refreshment afterwards. On day 14,

wells were photographed, and sphere numbers and diameters were analyzed by means of ImageJ using the formula A=π×d2/4.

3.2.5.3 Propidium iodide staining

8×10^5 RDES, SK-N-MC, and TC32 cells harboring a Dox-inducible shRNA against *PRC1* and respective control cells were seeded in 10 cm dish with/without addition of Dox (1 µg/ml) for 72 h. Dox was renewed 48 h after seeding. Ice-cold 70% ethanol was taken for cell fixation. 100 µg/ml RNAse (ThermoFisher) was added to the fixed cell solution, which was then stained with 50 µg/ml propidium iodide (PI) (Sigma Aldrich). At least 1 X 10^5 events were gated and analyzed with BD Accuri C6 Cytometer (**Figure 14).**

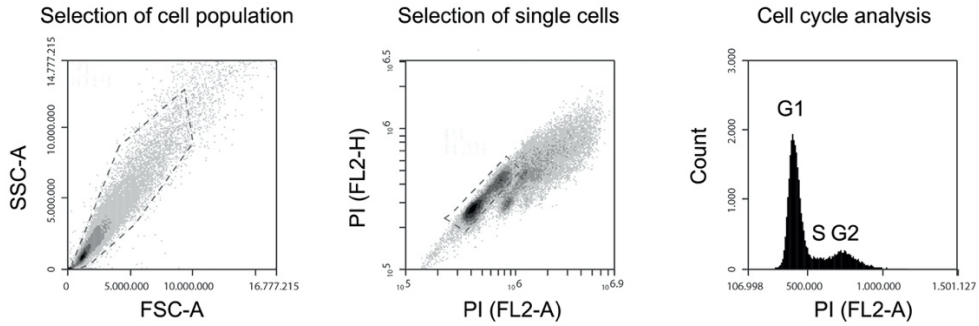

Figure 14 Representative gating steps for PI cell cycle analysis.

3.2.5.4 Annexin V staining

8×10^5 RDES, SK-N-MC, and TC32 cells harboring a Dox-inducible shRNA against *PRC1* and respective control cells were seeded in 10 cm dish with/without addition of Dox (1 µg/ml) for 72 h. Dox was renewed 48 h after seeding. 8×10^5 RDES and TC32 EwS cells treated with indicated dose of PLK1 inhibitors (BI2536 or BI6727) were seeded in 10 cm dish for 72 h. Cells were washed with PBS 1X and the pellet was collected by centrifuging at 1200 rpm, 4min. Cell pellet was resuspended by 500 µl 1x Annexin V buffer (5 µl of Annexin V + 5 µl PI solution) and incubated at RT for 15 min in the dark. At least 1 X 10^5 events was gated and analyzed with BD Accuri C6 Cytometer within 1h (**Figure 15**).

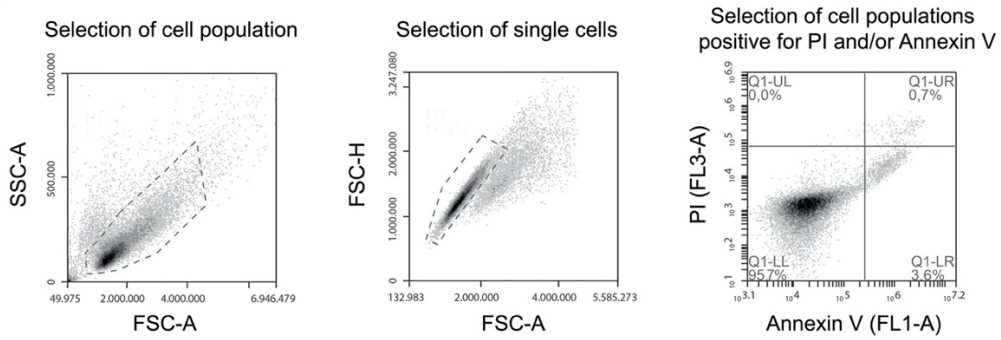

Figure 15 Representative gating steps for Annexin V cell apoptosis analysis.

3.2.5.5 Drug-response assay

For PLK1 inhibitor treatment, 5,000 cells/well of Dox-inducible shRNA expressing RDES and TC32 EwS cells were seeded in triplicate wells of 96-well plates. Cells were pre-treated for 48 h with Dox to induce the *PRC1* knockdown before addition of BI2536 (S1109, Selleckchem) or BI6727 (Volasertib; S2235, Selleckchem). Cells were then treated with 0–1,000 nM BI2536 or BI6727 (Volasertib) with/without Dox for additional 72 h. The same assays were carried out with wt and CRISPR Cas9-initiaed HDR edited A673 cell with a pre-incubation time of only 24 h to permit surface adherence. At the experimental endpoint, cell growth inhibition was assessed using a Resazurin assay (Sigma-Aldrich) based on manual instruction. PRISM 8 (GraphPad Software Inc., CA, USA) was used for calculating IC50 values.

3.2.5.6 Drug combination analysis

For drug combination assays, 5,000 cells of Dox-inducible shRNA expressing RDES and TC32 EwS cells were seeded in triplicate wells of 96-well plates. Cells were pre-treated for 48 h with Dox to induce the *PRC1* knockdown. Then, cells were treated with 0–100 nM PLK1 inhibitor, 0–4 nM Vincristine (VCR) and/or 0–100 nM Doxorubicin (Doxo). Inhibition of cell growth was assessed 72 h after start of the treatment using a Resazurin assay. Excess over Bliss was calculated using synergyfinder (R package v.2.2.4) [89]. For assessment of the dose reduction index (DRI), 5,000 cells/well of RDES and TC32 EwS cells were seeded in triplicate wells of 96-well plates 24 h before addition of PLK1 inhibitors. Cells were treated with 0–100 nM PLK1 inhibitor, 0–4 nM VCR alone or in combination in a 1:1 constant combination ratio as previously described [90]. Inhibition of cell

growth was assessed 72 h after start of the treatment using a Resazurin assay. CompuSyn (ComboSyn, Inc.) was used for determining the DRI of each PLK1 inhibitor at the IC50 level.

3.2.5.7 Doxo-resistance reversal assays

For Doxo-resistance reversal assays, non-toxic concentrations (<IC10) of PLK1 inhibitors BI2536 or BI6727 in two Doxo-res EwS cell lines (A673 Doxo-res; TC71 Doxo-res) was determined by a Resazurin assay after PLK1 inhibition (0–1,000 nM) for 72 h, respectively. In Doxo-resistant cell lines, the differential in vitro efficacy of Doxo depending on the co-treatment with PLK1 inhibitor BI2536 or BI6727, was assessed by a Resazurin assay. To this end, cells were treated for 72 h with different concentrations of Doxo (0–2,000 nM) and co-treated with the non-toxic dosage of PLK1 inhibitor BI2536 or BI6727 (10 nM) as defined above. The predicted ED50 concentrations were calculated using CompuSyn (ComboSyn, Inc.). For both cell lines, the reverse index (RI) was calculated by dividing the ED50 of Doxo alone by the ED50 of the combination-treatment (Doxo plus 10 nM of PLK1 inhibitor).

3.2.5.8 Fluorescence-in-situ-hybridization (FISH)

After shRNA-induced *PRC1* knockdown or PLK1 inhibitor treatment for 48 h, EwS cells with ~70% confluency were incubated for 6 h with 0.2 mg/ml colcemid (D1925 Sigma 10 µg/ml in HBSS). Cells were collected and incubated in a pre-warmed hypotonic solution (75 mM KCl) for 30 min at 37°C, and fixed in fresh, ice-cold Carnoy's fixative for 3×15 min. The fixed cells were kept overnight at 4°C. 20 µl of fixed sample was dropped onto pre-cold clean slides and allowed to air dry overnight. For chromosome counts, the cells were incubated with pan-centromere probe coupled with fluorescein isothiocyanate (FITC) dye (Star*FISH, 1695-F-02, Cambio, UK) following the manufacturer's instructions with modifications. Slides were kept in dark at 4°C. Analysis was carried out using a fluorescence microscope (Zeiss AxioVision MC 50, 100W HBO lamp) with a triple dye filter (DAPI, propidium iodide and FITC). Images were captured using AxioVision 4.9 software, and when necessary, signals were enhanced for optimal contrast using Adobe Photoshop 2020. Approximately 200 nuclei were evaluated in each

set from at least 3 independent experiments (at least 35 nuclei). The karyotypic changes were classified and quantified according to the International Standard of Cytogenetic Nomenclature (ISCN) [91]: aneuploidy (chromosome loss/gain), non-congressed, multipolar, and 'monster' cells.

3.2.5.9 Luciferase assay

2×10^5 A673/TR/shEF1 cells were co-transfected with the pGL3-promotor vectors with inserted mSat and Renilla pGL3-Rluc vectors (Promega) (ratio 100:1) in a 6-well plate by using the Lipofectamine LTX transfection kit (Thermo Fisher) according to its manual instruction. Transfection medium was replaced by medium with/without Doxycycline (Dox) (1 µg/ml; Sigma-Aldrich) 4 h after transfection. After 72 h the cells were lysed. The transcription activity has been measured by a dual luciferase assay system (Berthold). Firefly luciferase activity was normalized to Renilla luciferase activity.

3.2.6 Histology

3.2.6.1 IHC staining.

The slides received the antigen retrieval treatment and were stained with either polyclonal anti-PRC1 antibody (1:200, 15617-1-AP, Proteintech), polyclonal anti-CC3 primary antibody (1:100; 9661, Cell Signaling), monoclonal anti-phospho-γH2AX (1:8,000, ab81299, Abcam), monoclonal anti-human mitochondria antibody (1:1,000; ab92824, Abcam) or with monoclonal anti-Ki-67 (1:200, 275R-15, Cell Marque) for 60 min at RT. A monoclonal secondary horseradish peroxidase (HRP)-coupled horse-anti-rabbit antibody (ImmPRESS Reagent Kit, MP-7401/MP-7402, Vector Laboratories) was carried out depending on antibody species afterwards. AEC-Plus (K3461, Agilent Technologies) was used as chromogen. Samples were counterstained with hematoxylin (H-3401, Vector Laboratories). DAB+ (K3468, Agilent Technologies) was used as chromogen and hematoxylin for counterstaining. For CD99 staining, slides were stained with monoclonal anti-human CD99 antibody raised in mouse (1:40, ab8855, Abcam) for 32 min using the ultraView detection kit in a VENTANA BenchMark system (Roche, Basel, Switzerland), and counterstained with hematoxylin.

3.2.6.2 IHC quantification

To assess tissue integrity and for detection of mitotic defects, e.g., ‚monster' cells, FFPE blocks of EwS xenografts were stained with hematoxylin and eosin (H&E). Evaluation was performed similar to scoring of hormone receptor Immune Reactive Score (IRS) as previously described [92] (**Table 19**). The final IRS was determined by multiplying these two grades. Evaluation of Ki-67, CC3, and phospho-γH2AX immunoreactivity were quantified based on their positive staining percentage of cells per high-power field (HPF). Examination of 5–15 HPFs of at least one section is required for each sample.

% of expression	Grade	Intensity classification	Grade
0-19	0	None	0
20-39	1	Low	1
40-59	2	Moderate	2
60-79	3	Strong	3
80-100	4		

Table 19 IRS score of IHC quantification

3.2.6.3 Human samples and ethics approval

Human FFPE tissue samples were retrieved from the archives of the Institute of Pathology of the LMU Munich (Germany) and the Gerhard-Domagk Institute of Pathology of the University of Münster (Germany) with approval of the institutional review boards. All patients gave informed consent. Tissue-microarrays (TMAs) were stained and analyzed with approval of the ethics committee of the LMU Munich (approval no. 550-16 UE).

3.2.7 Survival analysis

A public-available cohort comprising tumor samples of 196 primary EwS tumors with clinical annotations were analyzed [93]. *PRC1* transcription expression was stratified as low (1st Third), moderate (2nd Third) and high (3rd Third). The expression of PRC1 was analyzed in a cohort of 144 EwS patients with available clinical

annotation by IHC staining. PRC1 expression was stratified by different IRS values in those with low (IRS<2), moderate (IRS:2-5) and high (IRS>5). P value in overall survival (OS) analysis was assessed by the Kaplan-Meier method (Log-rank Mantel-Cox test).

3.2.8 *In vivo* models

3.2.8.1 Xenograft subcutaneously injected with shRNA-mediated cells

5×10^6 EwS cells were injected subcutaneously in a 1:1 mix of cells suspended in HBSS formulated with Calcium and Magnesium (ThermoFisher) of 10–12 weeks old NOD/Scid/gamma (NSG) mice. Tumor diameters were measured every two day. Tumor volume was calculated by the formula (L×l2)/2. When the tumors reached an average volume of ~100 mm3, mice were randomized in different groups according to the purpose of each experiment. For mice injected with Dox-inducible shRNA against *PRC1* EwS cells, 2 mg/ml BelaDox (Bela-pharm) dissolved in drinking water containing 5% sucrose (Sigma-Aldrich) was used to induce an *in vivo* knockdown. Mice injected with control cells only received 5% sucrose (control). All mice were sacrificed by cervical dislocation once tumor volume of the last mouse in control group exceeded 1,500 mm^3. Then, xenograft tumors were extracted and fixed in 4%-formalin and paraffin-embedded (FFPE) for (immuno)histology.

3.2.8.2 Intravenous injection of PLK1 inhibitors

5×10^6 CRISPR Cas9-initiated HDR edited PRC1-associated mSat KO A673 cells and CRISPR Cas9-edited negative control (NC) cells were subcutaneously injected in mice of 10-12-week-old. When tumors were growing to an average volume of ~100 mm^3, mice were randomized and treated once per week intravenously (i.v.) with 40 mg/kg BI2536, 30 mg/kg BI6727 (Volasertib) or vehicle (0.1N HCl with 0.9% saline) for 3–4 weeks. Mice were sacrificed by cervical dislocation once the tumor volume of the last mouse in the control group exceeded 1,500 mm^3 or after the last cycle of treatment. Then, xenograft tumors were extracted and fixed in 4%-formalin and paraffin-embedded (FFPE) for (immuno)histology. Animal experiments were approved by the government of Upper Bavaria and

conducted in accordance with ARRIVE guidelines, recommendations of the European Community (86/609/EEC), and UKCCCR (guidelines for the welfare and use of animals in cancer research).

3.2.9 *In silico* analysis

3.2.9.1 Chromatin immuno-precipitation DNA sequencing (ChIP-Seq)

ENCODE SK-N-MC DNase-Seq (GSM736570) and ChIP-Seq data (GSE61944) were extracted from the GEO, analyzed as previously described and loaded in the UCSC genome browser [22]. The following samples were used in this study:

ENCODE_SKNMC_hg19_DNAseHS_rep1

GSM1517546_SKNMC.shGFP96.FLI1

GSM1517555_SKNMC.shFLI196.FLI1

GSM1517547_SKNMC.shGFP96.H3K27ac

GSM1517556_SKNMC.shFLI196.H3K27ac

GSM1517569_A673.shGFP48.FLI1

GSM1517572_A673.shFLI148.FLI1

GSM1517570_A673.shGFP48.H3K27ac

GSM1517573_A673.shFLI148.H3K27ac

3.2.9.2 Enriched GO analysis

To identify genes involved in cytokinesis in EwS, we used curated publicly available gene expression data generated on Affymetrix HG-U133 Plus2.0 DNA microarrays for 979 samples comprising 50 EwS tumor samples and 929 normal tissue samples (71 normal tissue types) [94]. First, differential gene expression and statistical significance levels were calculated with *limma* (R package, v,3.44.3) [95]. Then, the resulting *P*-values were adjusted for multiple testing based on false discovery rate (FDR) correction. Finally, only differentially expressed genes with significant fold changes (FCs) (FDR-adjusted $P<0.05$) were

analyzed for Gene Ontology (GO)-term enrichment using *clusterProfiler* (R package, v,3.16.1) [96]. Annotation of GO-terms was done using the *org.Hs.eg.db* (R package, v,3.11.4).

3.2.9.3 Transcriptome analysis

Extracted RNAs from EwS cells with/without *PRC1* silencing for 60 h were transcriptome profiled at IMGM laboratories (Martinsried, Germany). Samples with RNA integrity numbers (RIN) > 9 were hybridized to Human Affymetrix Clariom D microarrays. SST-RMA algorithm was used for data normalization via Transcriptome Analysis Console (v4.0; Thermo Fisher Scientific). Annotation was performed using the Affymetrix library for Clariom D Array (version 2, human) on gene level. Differentially expressed genes (DEGs) with consistent and significant FCs across shRNAs and cell lines were identified in our previously published paper [97] as shown in **Figure 16**:

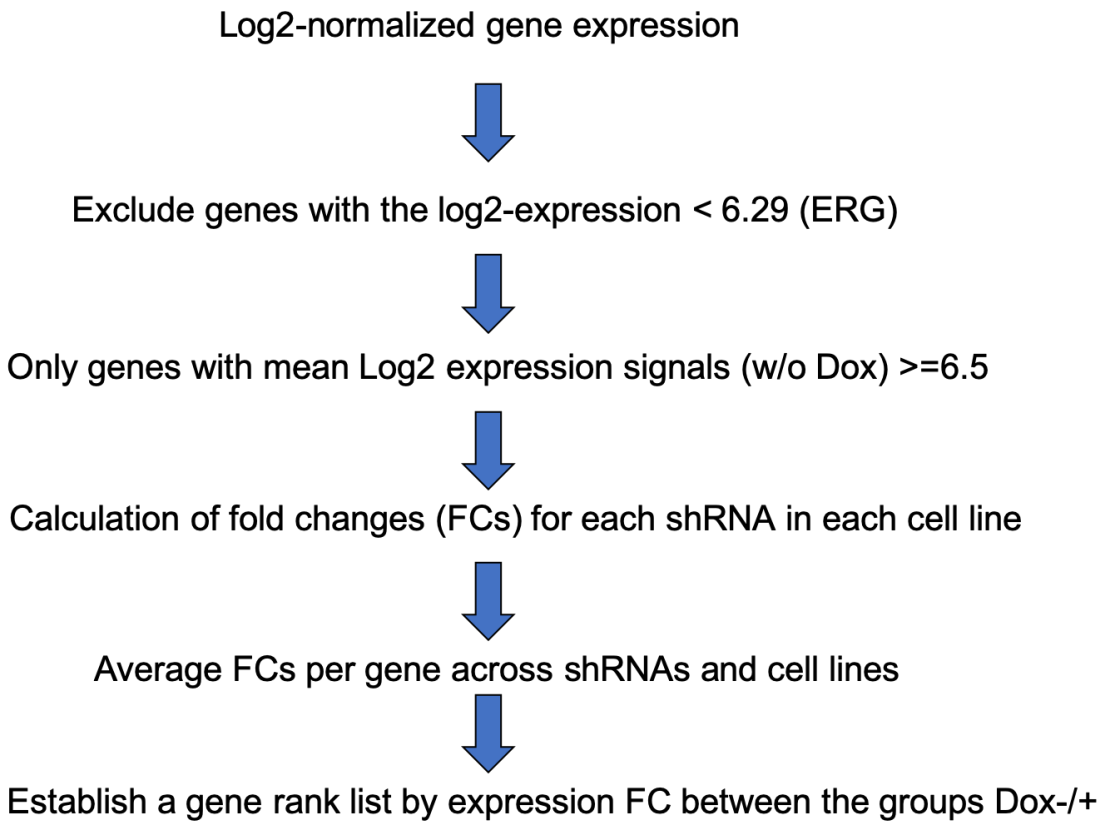

Figure 16 Identification of DEGs and establishment of pre-rank gene list

fgsea (R package, v,1.14.0) was used for pre-ranked gene-set enrichment analysis (GSEA) annotated by GO definitions from MSigDB (v7.0, c2.cgp.all) [98],

[99]. Filtered GO terms (adjusted P<0.01; |Normalized enrichment score|>1.75) (**Appendix A**) were used to create a symmetric GO adjacency matrix based on the Jaccard distance between GO terms and respective gene lists. GO clusters were identified using dynamicTreeCut (R package, v.1.63.1), and the GO network was visualized in Cytoscape (v.3.8.0) [100].

3.2.10 Statistics

If not otherwise specified in the figure legends, data are presented as box-dot-plots with horizontal bars representing means and whiskers indicating the standard error of the mean (SEM). Data analysis was carried out by using PRISM 8 (GraphPad Software Inc., CA, USA) or R project. Comparison of two groups in functional *in vitro* and *in vivo* experiments was calculated by using a two-sided Mann-Whitney test. Contingency tables of FISH counting were carried out by the Chi-square or Fisher's exact test as appropriate. Pearson correlation analysis was done and visualized using the R package ggpubr (v,0.4.0). Statistical differences between the groups were assessed by a Mantel-Haenszel test. Cox multivariate statistical analyses were carried out in IBM SPSS Statistics software (version 23.0; IBM Corp). *P*-values <0.05 were classified as statistically significant and all P-values were calculated from two-sided statistical tests.

4. Results

CIN is a hallmark of cancer [101]. Yet, many childhood cancers, such as EwS, feature remarkably 'silent' genomes with minimal CIN [102]. PRC1 plays key roles in assembling a complete functional spindle midzone [58], [103]. Its role involved in microtubule-bundling activity assures proper spindle midzone formation [104]. Thus, this thesis aims to investigate by means of the EwS model how uncoupling of mitosis and cytokinesis via targeting PRC1 or its activating PLK1 can be employed to induce fatal genomic instability and tumor regression.

4.1 PRC1 is the most highly overexpressed cytokinesis-related gene in EwS and correlates with poor overall survival in EwS patients.

4.1.1 PRC1 is the most highly overexpressed cytokinesis-related gene in EwS

Curated expression data of 929 normal tissue samples (71 tissue types) and 50 primary EwS tumors were analyzed to search for significantly overexpressed genes in EwS compared to normal tissues [105] (**Figure 17**). Among its versatile and profound role in normal cell division and cellular structure formation (**Figure 18**), *PRC1* exhibited the greatest fold change among 77 significantly overexpressed cytokinesis-related genes (FDR-adjusted $P<0.05$) (**Figure 19**), being on average ~8-fold higher expressed in EwS than in normal tissues (**Figure 20**). These results indicated that PRC1 could be a proper candidate offering a large therapeutic window for CIN-induced therapy in EwS.

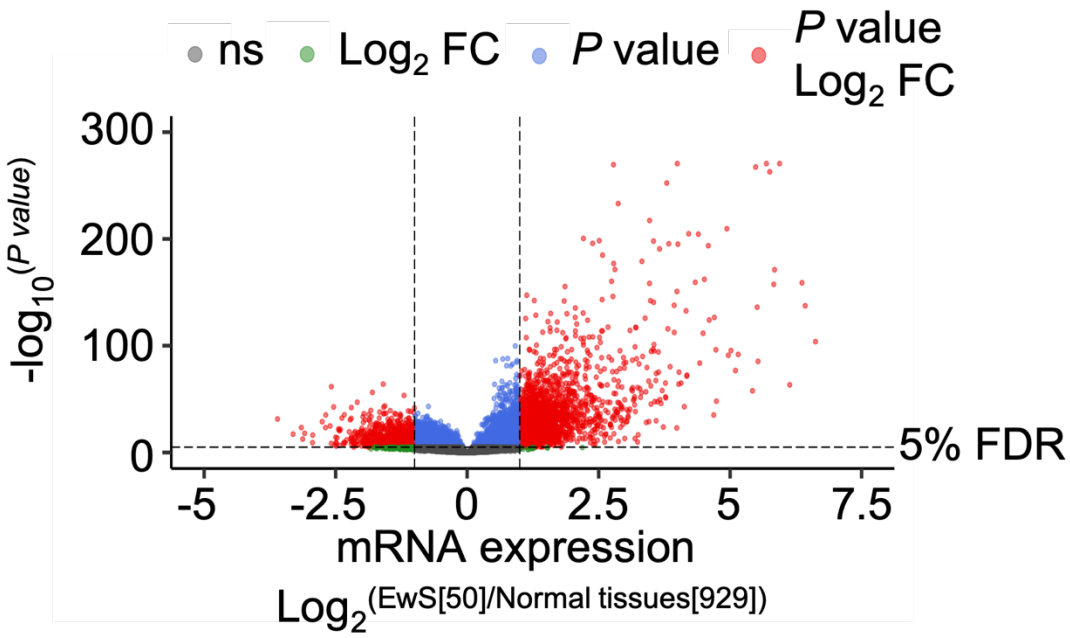

Figure 17 Volcano plot of DEGs

Volcano plot showing differentially expressed genes (DEGs) in EwS (50 samples) compared to normal tissues (929 samples). *P* value less than 5% FDR adjustment was used as the threshold.

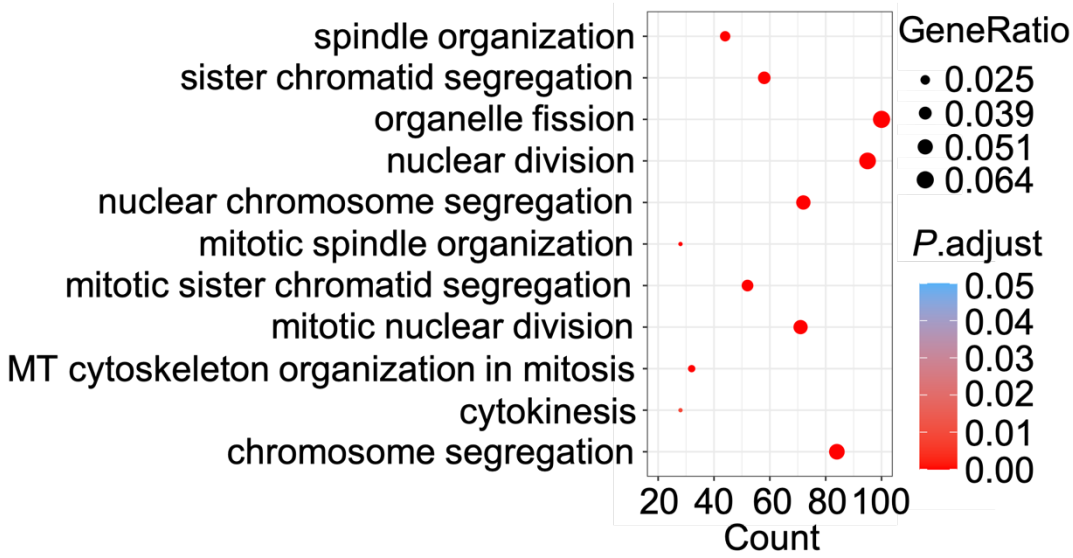

Figure 18 GO enrichment analysis

GO enrichment analysis indicated that *PRC1* actively participates in multiple biological processes in EwS.

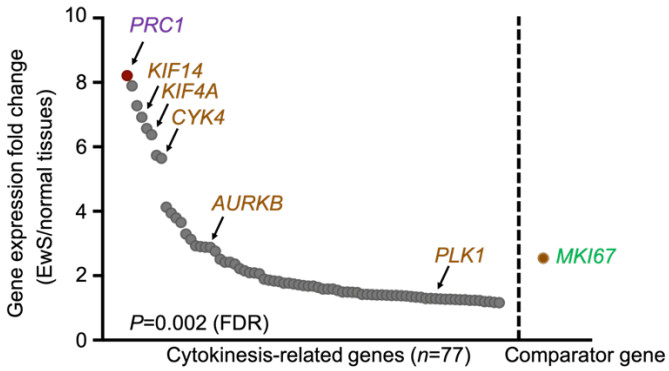

Figure 19 PRC1 is the most overexpressed cytokinesis-related gene in EwS

Displayed are 77 significantly upregulated genes in EwS compared to normal tissues (linear fold change (FC)>1, FDR $P<0.05$) that are annotated for the GO-term cytokinesis (GO:0000910). *MKI67* encoding the proliferation marker Ki-67 was used as a comparator. *PRC1* and its direct interacting/binding partners, such as cytokinesis defect 4 (*CYK4*), aurora kinase B (*AURKB*), the kinesin family members 14 and 4A (*KIF14/4A*) as well as *PLK1*, have been indicated by arrows.

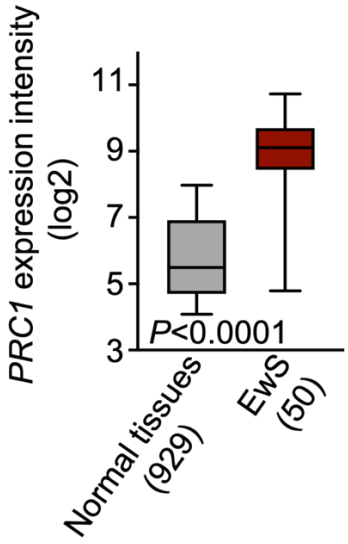

Figure 20 PRC1 overexpressed in EwS in comparison to normal tissues

Analysis of *PRC1* mRNA expression in 50 EwS and 929 normal tissues (comprising 71 normal tissue types). Horizontal bars indicate median expression levels, boxes the interquartile range, and whiskers the 10th and 90th percentile.

4.1.2 The prognostic value of PRC1 in EwS patients

An established patient cohort (n=196) in which EwS tumors were profiled on gene expression microarray was analyzed [94]. A Kaplan-Meier analysis revealed that high *PRC1* expression is associated with poor OS of EwS patients (*P*=0.005) (**Figure 21**). To verify this result at the protein level, a tissue-microarray (TMA) comprising 144 independent EwS samples with a specific anti-PRC1-antibody (specificity proven through *in vivo* knockdown experiments) was stained by IHC. Although EwS tumors showed on average relatively strong immunoreactivity for PRC1, substantial inter-tumor heterogeneity was observed, which allowed semi-quantitative grouping of tumors based on PRC1 expression. While 54% (78/144) of samples did not express detectable levels of PRC1, 24% (35/144) displayed low, and 21% (31/144) high expression. Kaplan-Meier analysis confirmed that patients with PRC1 overexpression had a poor overall survival as compared to patients with low or absent PRC1 expression (*P*=0.0037) (**Figure 22**). Furthermore, Cox multivariate analysis indicated that, in addition to the status of metastasis, PRC1 overexpression is an independent prognostic factor in EwS patients (OR:3.1, P=0.04) (**Table 20**).

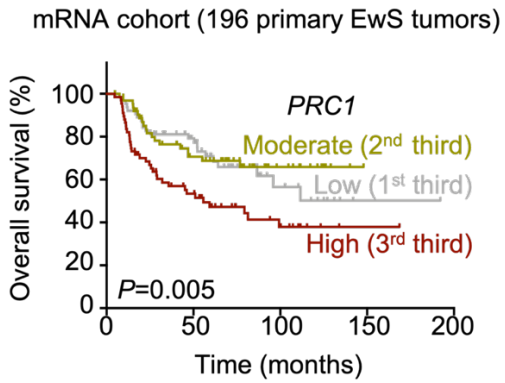

Figure 21 Kaplan-Meier survival analysis of 196 EwS patients stratified by thirds of PRC1 mRNA expression (Low, Moderate, High).

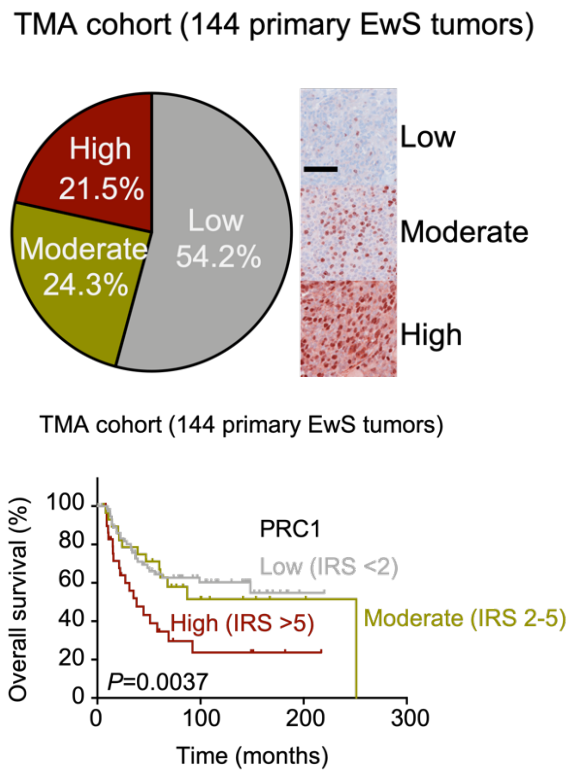

Figure 22 Overexpression of PRC1 at protein level correlates with poor overall survival in EwS

Upper: IHC staining of a TMA comprising 144 primary EwS tumors for PRC1. Scale bar=200 µm; Lower: Kaplan-Meier analysis of overall survival of 144 EwS patients stratified by their intra-tumoral PRC1 expression levels (Low: IRS <2; Moderate: IRS 2–5; High: IRS >5). Mantel-Haenszel test.

Factors	OR (95% CI)	*p*
age >20	not included in the variants	0.385
gender	not included in the variants	0.72
Low PRC1 expression	1	
High PRC1 expression	3.108 (1.050-9.201)	0.041
w/o metastasis	1	
with metastasis	3.371 (1.308-8.687)	0.01
w/o recurrence	not included in the variants	
with recurrence		0.211

Table 20 Evaluation of risk factors of prognosis in 96 primary EwS patients by Cox regression analysis

Collectively, these data suggest that PRC1 offers a therapeutic window for CIN-induced therapy via uncoupling cytokinesis and mitosis in EwS. Its significantly heterogeneous overexpression in EwS correlates with poor overall survival and could serve as an independent prognostic factor for EwS patients.

4.2 EWSR1-FLI1 directly regulates *PRC1* expression

4.2.1 EWSR1-FLI1 positively regulates PRC1 expression in a time-dependent manner

An established cell line model (A673/TR/shEF1) [106] that enables a doxycycline-(dox)-inducible shRNA-mediated knockdown of the fusion protein was used to test if EWSR1-FLI1 regulates *PRC1* expression or not. In time-course experiments silencing of *EWSR1-FLI1* was accompanied by downregulation of *PRC1* (**Figure 23a**). These results were further validated by IHC on the protein level in xenografts derived from A673/TR/shEF1 *in vivo*, whereas no effect was observed

by dox-treatment of A673/TR/shCtrl xenografts expressing an inducible non-targeting control shRNA (**Figure 23b**).

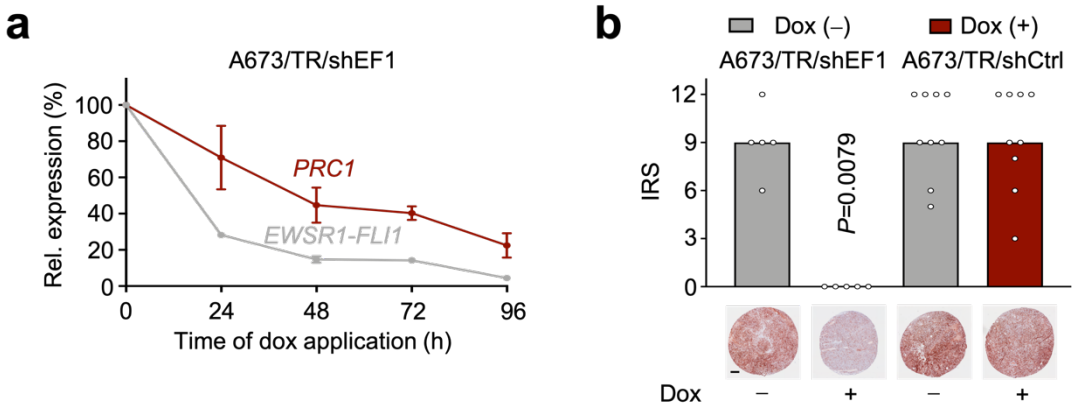

Figure 23 EWSR1-FLI1 regulates PRC1 expression in a time-dependent manner

a) Time-course knockdown of *EWSR1-FLI1* in A673/TR/shEF1 EwS cells and analysis of *PRC1* and *EWSR1-FLI1* expression by qRT-PCR *in vitro*. Dots represent means and whiskers SEM, n=4 biologically independent experiments. **b)** Analysis of PRC1 expression by IHC in xenografts derived from A673/TR/shEF1 and A673/TR/shCtrl cells with/without Dox-treatment for 96 h *in vivo*. Data are displayed as individual dots. Horizontal bars represent median, n≥5 biologically independent experiments; Scale bar=200 µm.

4.2.2 The enhancer activity of EWSR1-FLI1 on regulating PRC1 expression is determined upon the length of the GGAA-motifs.

ChIP-Seq data for EWSR1-FLI1, and epigenetic marks (H3K4me1 and H3K27ac) generated in EwS cell lines (A673 and SK-N-MC) [35] revealed a prominent EWSR1-FLI1 peak located about 90 kb apart from the PRC1 promoter. This EWSR1-FLI1 peak mapped to a GGAA-mSat located in an area with open chromatin (DNase 1 hypersensitivity site) that exhibited epigenetic characteristics for an active enhancer (**Figure 24**). Silencing of *EWSR1-FLI1* was accompanied by a loss of EWSR1-FLI1 ChIP-Seq signals at this locus in both cell lines, and more interestingly, with a loss of activating H3K27ac histone marks (**Figure 24**).

To verify the *EWSR1-FLI1*-dependent enhancer activity of this GGAA-mSat, different alleles from three EwS cell lines (A673, EW1 and TC71) encompassing variable numbers of GGAA-repeats were cloned into the pGL3 luciferase vector. All cloned fragments included flanking regions (in total 1,053 bp). Dual luciferase assays in A673/TR/shEF1 with/without silencing of *EWSR1-FLI1* showed that this

GGAA-mSat had strong *EWSR1-FLI1*-dependent enhancer activity, which increased with the number of consecutive GGAA-repeats (**Figure 25a**). Other genetic variation in the cloned fragments was excluded by WGS and focal Sanger-sequencing. Notably, the average number of GGAA-repeats at this mSat positively correlated to the *PRC1* expression levels across EwS cell lines (**Figure 25b**).

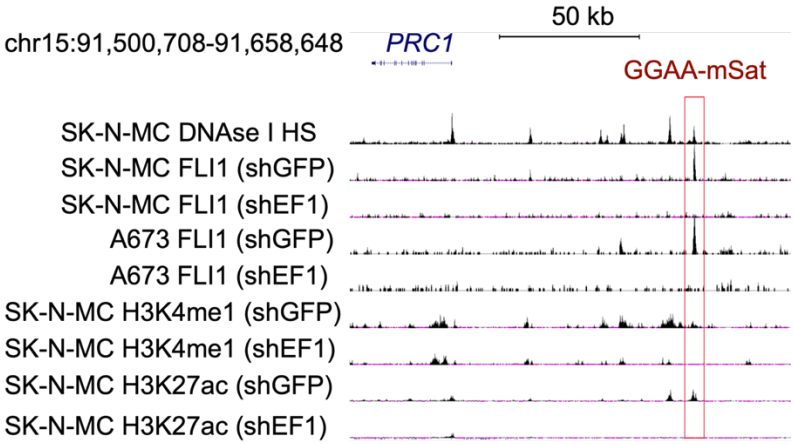

Figure 24 Integrative genomic view (hg19) of the PRC1 locus from data of A673 and SK-N-MC cells being transfected with shRNAs targeting either *GFP* (shGFP; negative control) or *EWSR1-FLI1* (shEF1).

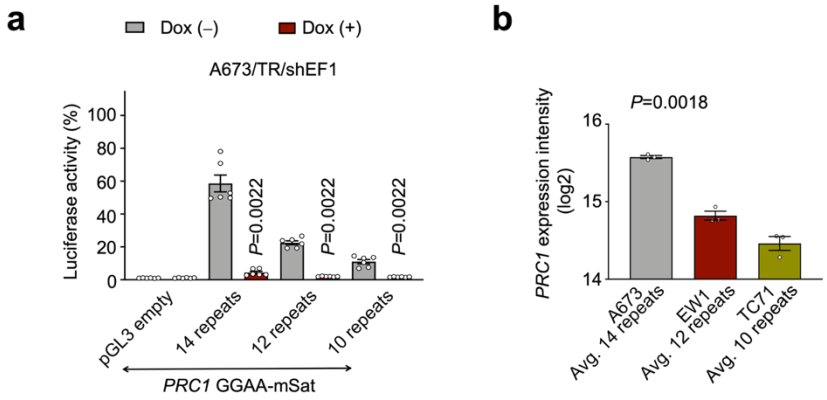

Figure 25 EWSR1-FLI1-bound GGAA-mSats have enhancer activity in regulation of *PRC1* expression.

a) Luciferase reporter assays in A673/TR/shEF1 cells with/without knockdown of *EWSR1-FLI1* (Dox +/–) 72 h after transfection. Data are displayed as individual dots. Horizontal bars represent means and whiskers SEM, n=6 biologically independent experiments. **b)** *PRC1* expression intensity in 3 EwS cell lines as assessed by Affymetrix Clariom D microarrays (triplicates per cell line). The average number of GGAA-repeats at the *PRC1*-asscoiated GGAA-mSat is reported. One-way ANOVA test.

4.2.3 Epigenomic *PRC1*-associated GGAA-mSat blockage via CRISPR interference

To confirm the regulatory effect of this GGAA-mSat on *PRC1* transcription, clustered regulatory interspaced short palindromic repeats interference (CRISPRi) experiments in two EwS cell lines (A673, RDES) were performed. Epigenetic interference with this GGAA-mSat markedly reduced *PRC1* expression and proliferation of derivative EwS cells (A673/TRE/dCas9/KRAB; RDES/TRE/dCas9/KRAB) (**Figure 26**).

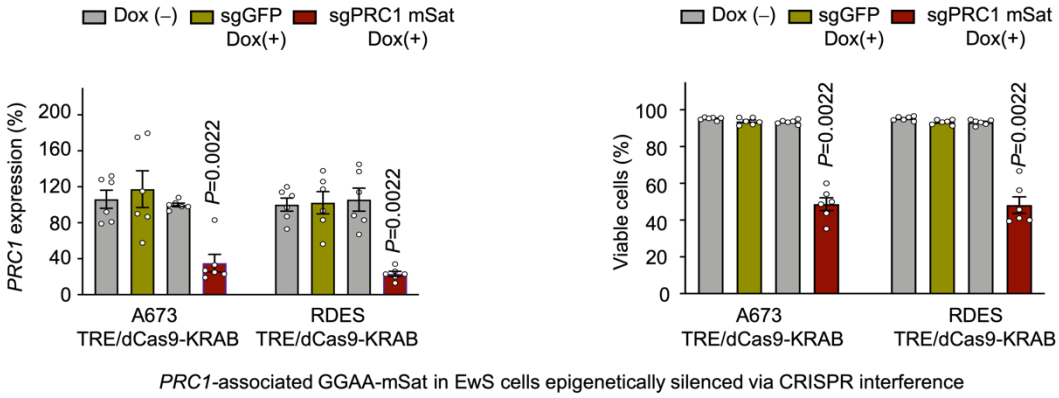

Figure 26 Epigenomic *PRC1*-associated GGAA-mSat blockage via CRISPR interference

Analysis of *PRC1* expression by qRT-PCR (**left**) and viable cells (**right**) in TRE-regulated dCas9-KRAB A673 and RDES cells transduced with sgRNAs against the *PRC1*-associated GGAA-mSat and GFP sgRNAs (negative control) 15d after addition of Dox (2 µg/ml). Data are displayed as individual dots. Horizontal bars represent means and whiskers SEM, n=6 biologically independent experiments.

4.2.4 CRISPR Cas9-initiaed HDR edited PRC1-mSat modification

In order to gnomically edit the enhancer-like GGAA-mSat, a knockout (KO) experiment of the *PRC1*-associated GGAA-mSat and a knock in (KI) experiment of a 24-GGAA exogenous motifs into the locus of *PRC1*-associated mSat via homology-directed repair (HDR) using CRISPR-Cas9 genome editing were carried out (**Figure 27**). KO of the *PRC1*-associated GGAA-mSat strongly reduced *PRC1* expression and proliferation of A673 cells compared to wide type cells (wt), while no significant differences were observed in its control cells (NC). Strikingly, replacement of the wt mSat comprising 14 consecutive GGAA-repeats by a ‘longer’

haplotype (24 GGAA-repeats) in A673 cells significantly, increased *PRC1* expression and proliferation (**Figure 28**). This finding has been confirmed in a second EwS cell line RDES (**Figure 29**). Consistently, in a long-term colony forming culture, reduced sphere formation was observed accompanied with decreased *PRC1* expression while a growing advantage was observed in KI cells (**Figure 30**).

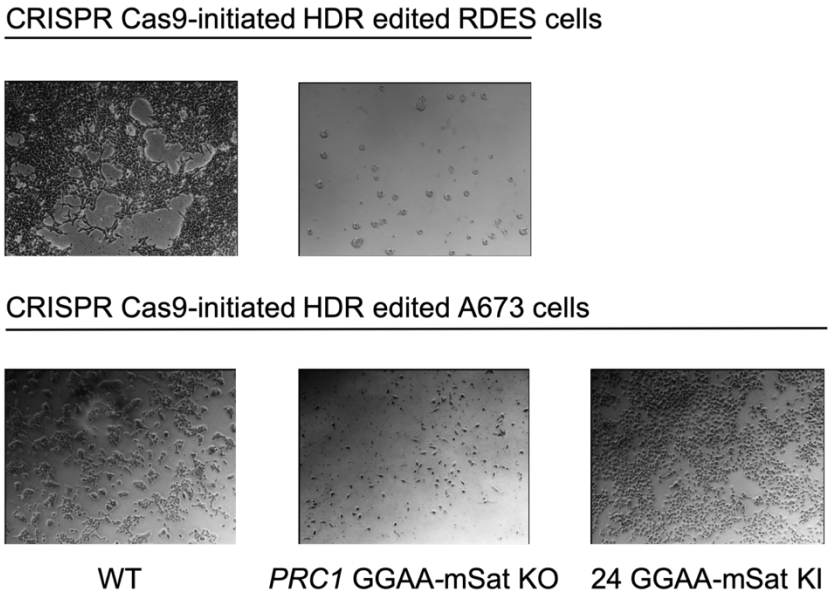

Figure 27 Representative cell culture images of A673 and RDES wt cells and their CIRPSR Cas9-initiated HDR derivatives (magnification: 40X).

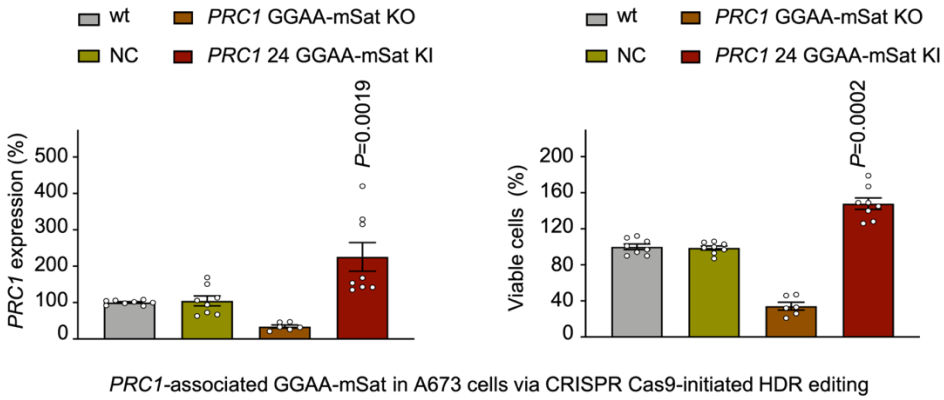

Figure 28 CRISPR Cas9-initiaed HDR edited *PRC1*-mSat knock in modification

Analysis of *PRC1* expression by qRT-PCR **(left)** and viable cells **(right)** in wildtype (wt), CRISPR Cas9-edited negative control (NC) and CRISPR Cas9-initiated HDR edited (KO and insertion of 24-GGAA-repeats) A673 cells 72 h after seeding. Data are displayed as individual dots. Horizontal bars represent means and whiskers SEM, n=8 biologically independent experiments.

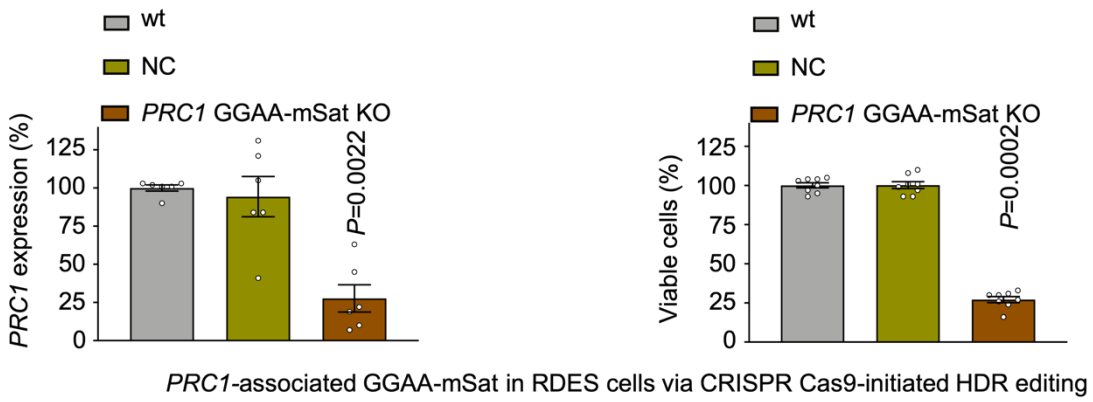

Figure 29 CRISPR Cas9-initiaed HDR edited PRC1-mSat knock-out modification

Analysis of *PRC1* expression **(left)** and proliferation **(right)** of RDES wt, CRISPR Cas9-initiated HDR edited NC and *PRC1*-associated GGAA-mSat KO cells 72 h after seeding. Data are displayed as individual dots. Horizontal bars represent means and whiskers SEM, n=6-8 biologically independent experiments; Two-sided Mann-Whitney test.

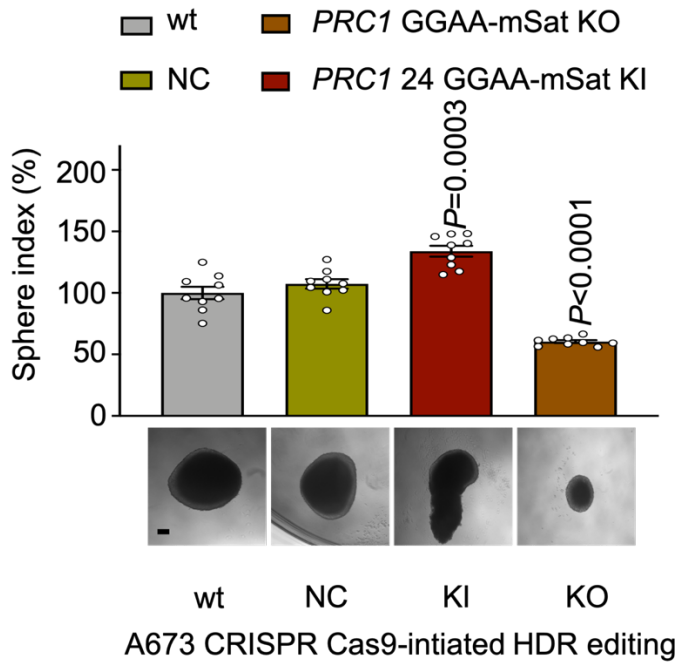

Figure 30 3D-sphere formation assay of CRISPR-HDR edited EwS cells

Sphere formation assays of A673 wt and their CRISPR/Cas9-initiated HDR edited *PRC1*-associated GGAA-mSat derivatives. Data are displayed as individual dots. Horizontal bars represent means and whiskers SEM, n=9 biologically independent experiments; Two-sided Mann-Whitney test. Scale bar=50 µm.

4.2.5 EWSR1-FLI1 physically hijacks *PRC1* expression in EwS

In order to further verify if *PRC1* is a direct target gene of EWSR1-FLI1 in EwS, 3C-PCR was performed to test whether the digested fragment containing EWSR1-FLI1-bound enhancer-like GGAA mSat physically forms a looping to *PRC1* promoter region, thereby regulating *PRC1* expression in EwS. In this assay, CRISPR Cas9-initiated HDR edited A673 EwS cells with either a genomic KO of *PRC1*-associated GGAA-mSat or an elongation of a consecutive 24-GGAA mSat were analyzed, individually. HindIII-digested fragment containing the *PRC1*-associated GGAA-mSat has been used as the bait, while the *PRC1* promoter fragment and three other digested fragments located in various linearize distances away from *PRC1*-associated mSat were separately tested, separately. The digestion efficacy of each fragments tested in the 3C-PCR was evaluated before performing the assay (**Figure 30**). Indeed, the results confirmed a physical interaction of both DNA elements, which was abrogated by KO of the *PRC1*-associated GGAA-mSat (**Figure 31**).

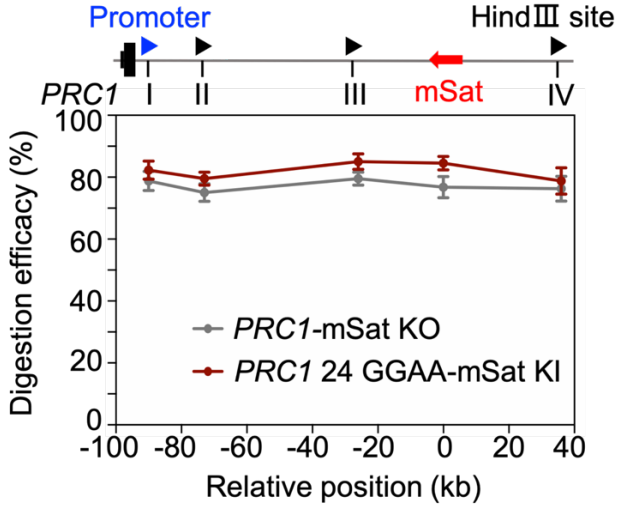

Figure 31 Digestion efficiency of HindIII fragments in 3C-PCR

Digestion efficiency for the HindIII digested fragments analyzed in the 3C-PCR assays measured by qRT-PCR. Dots represent means and whiskers SEM, n=4 biologically independent experiments.

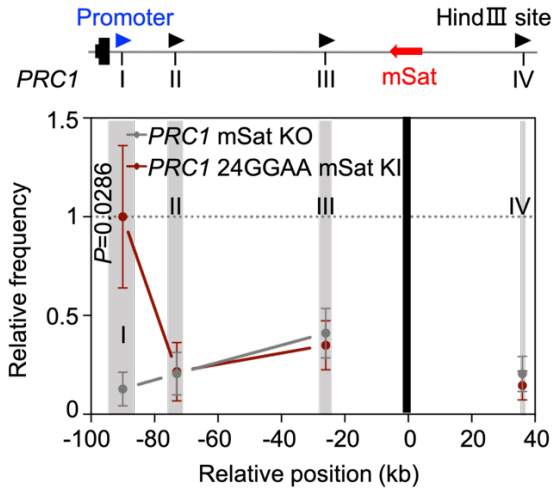

Figure 32 3C-PCR showing relative crosslinking frequencies

Relative crosslinking frequencies observed in CRISPR Cas9-initiated HDR edited *PRC1*-associated GGAA-mSat knockout (KO) A673 EwS cells are shown in gray and insertion of 24-GGAA repeats in dark red. Gray shading refers to tested-fragment position and size, and black shading the 'fixed' fragment harboring the *PRC1*-associated GGAA-mSat. The highest crosslinking frequency value in the graph was normalized and set to 1 in each replicate. Data are mean and SEM, n=4 biologically independent experiments. Two-sided Mann-Whitney test in all panels.

In summary, high but variable expression of PRC1 in EwS is controlled by EWSR1-FLI1-binding to a polymorphic enhancer-like GGAA-mSat.

4.3 PRC1 promotes EwS growing *in vitro* and *in vivo*

4.3.1 Dysregulated *PRC1* inhibits tumor growing triggered by CIN-induced non-viable karyotype *in vitro*

Three EwS cell lines (SK-N-MC, RDES and TC-32) transduced with two different Dox-inducible shRNAs against *PRC1* (shCDS and shUTR) and a shCtrl were established as described in the method part. Dox (1 µg/ml) was applied to the cultured medium of transduced cells for downregulating *PRC1* expression at the mRNA (48 h) and protein level (72 h), respectively (**Figure 33**).

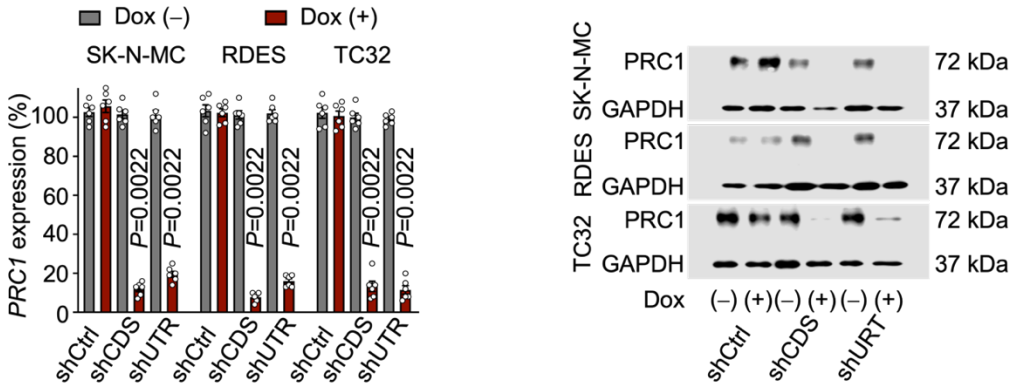

Figure 33 PRC1 knockdown efficacy test

Left: Analysis of *PRC1* mRNA levels by qRT-PCR in three EwS cell lines harboring Dox-inducible shPRC1 (shCDS/shUTR) or shCtrl constructs. Data are displayed as individual dots. Horizontal bars represent means and whiskers SEM, n=6 biologically independent experiments. **Right:** Representative images of Western blots of cells depicted in (left). GAPDH served as loading control.

Afterwards, Affymetrix Clariom D arrays has been performed with/without *PRC1* knockdown in SK-N-MC and RDES EwS cells. Silencing of *PRC1* for 60 h, that is before onset of cell death to avoid obscuring events due to activation of cell death pathways, led to differential gene expressions. In detail, *PRC1* silencing induced a concordant down- or upregulation of 2,896 and 381 genes, respectively, across shRNAs and cell lines (**Figure 34**). Functional gene-set enrichment (GSEA) followed by weighted correlation network analysis revealed that *PRC1* had pleotropic effects on diverse cellular functions linked amongst others to DNA packaging, chromosome formation, cell morphology, and growth (**Figure 35**).

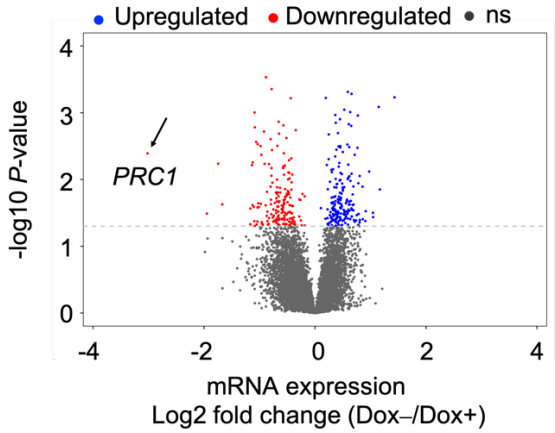

Figure 34 Volcano-plot of DEGs identified in transcription analysis upon *PRC1* knockdown

Volcano-plot depicting differentially expressed genes of RDES and SK-N-MC cells with/without *PRC1* knockdown (summary level data). Arrow indicates PRC1.

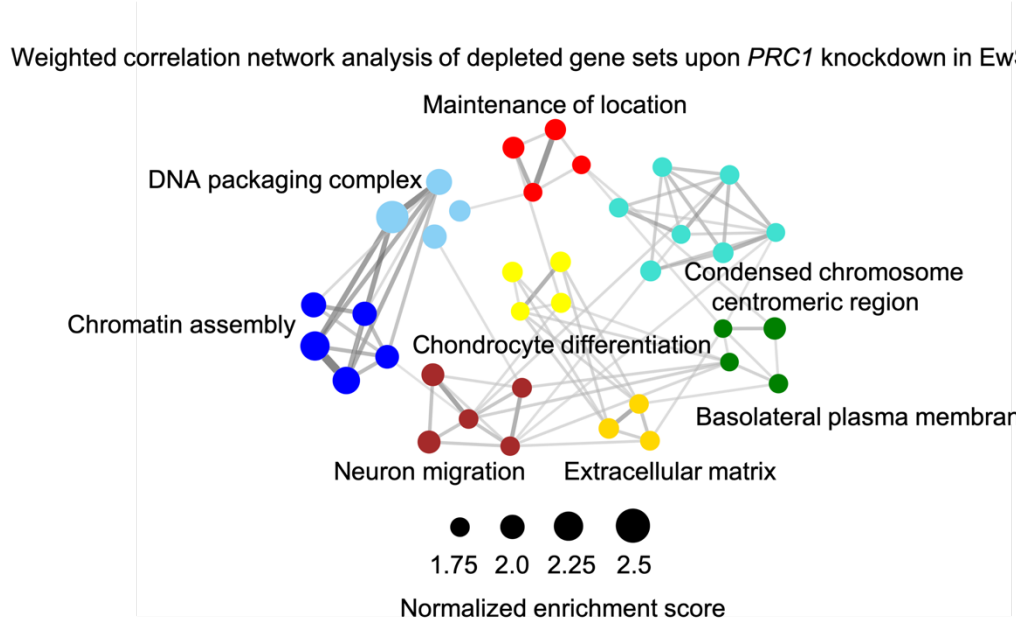

Figure 35 Weighted correlation network analysis of downregulated genes in *PRC1* knockdown cells.

In line with these predictions, Dox-induced *PRC1* knockdown for 72 h strongly reduced the number of viable cells. while inducing massive apoptosis in all three cell lines *in vitro* (**Figure 36a,b**). In the long-term observation, both in 2D clonogenic growth and 3D spheroidal growth assays *PRC1* knockdown significantly reduced clonogenic and spheroidal growth *in vitro* (**Figure 36c,d**).

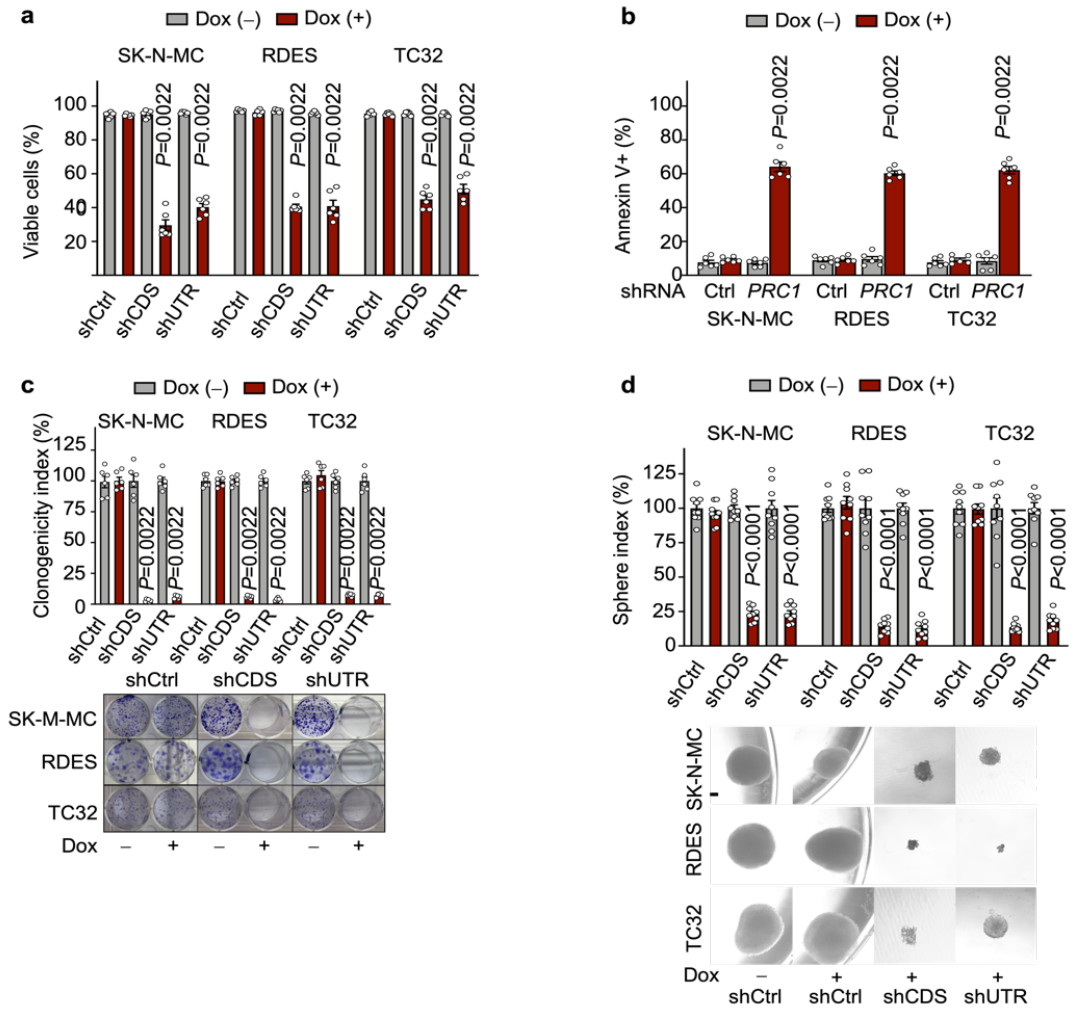

Figure 36 PRC1 contributes to proliferation and tumorigenesis in EwS *in vitro*

a) Analysis of viable cells 72 h after shRNA-mediated knockdown of *PRC1*. **b)** Analysis of apoptosis with/without shRNA-mediated knockdown of *PRC1* for 72 h (summary of two different shRNAs). **c)** Colony-forming assays of EwS cells with Dox-inducible *PRC1* knockdown or a non-targeting shCtrl. **d)** Sphere formation assays of RDES, SK-N-MC, and TC32 EwS cells with Dox-inducible knockdown of *PRC1*. Data are displayed as individual dots. Horizontal bars represent means and whiskers SEM, n=6-9 biologically independent experiments; two-sided Mann-Whitney test. Representative images of spheres are shown; Scare bar=50 µm.

Considering PRC1's essential function in spindle mid-zone formation [70], it is conceivable that these phenotypes may be explained by excessive CIN resulting from cytokinesis defects upon *PRC1* knockdown. Indeed, *PRC1* silenced EwS cells exhibited higher numbers of tetraploid cells through blockage of proper G2/M-phase transition (**Figure 37a**). FISH analyses using pan-centromere probes revealed that *PRC1* knockdown for only 48 h induced likely non-viable chromosomal abnormalities in ~70% of EwS cells compared to ~10% in controls (**Figure 37b**).

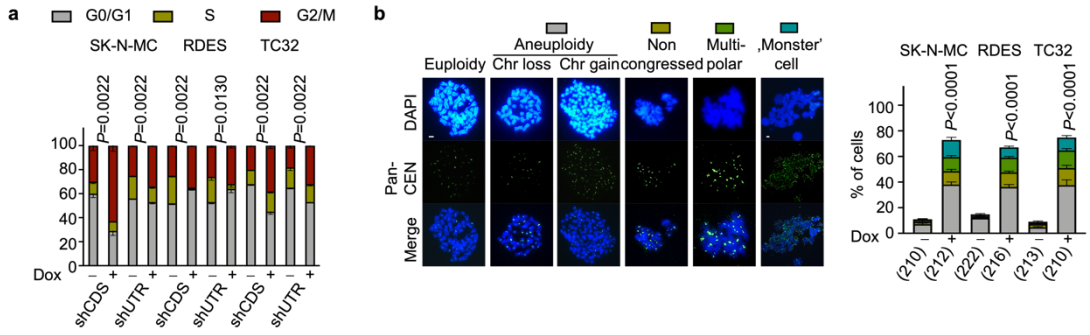

Figure 37 PRC1 safeguards genome stability in EwS

a) Analysis of cell cycle phases after knockdown of *PRC1* for 72 h. Data are displayed as individual dots. Horizontal bars represent means and whiskers SEM, n=6 biologically independent experiments. Two-sided Mann-Whitney test in all panels. **b)** Representative images of mitotic spreads. Each category is composed of an image of the entire mitotic spread in which DAPI (blue), pan-centromere (Pan-CEN)-FITC (green), and merged images are presented. Scale bar=1 µm. Quantification of the data are shown in pile-up bar plots depicting the percentages of aberrant metaphases after shRNA-mediated knockdown of *PRC1* for 48 h. Horizontal bars represent means and whiskers SEM, n=6 biologically independent experiments. The total number of mitoses analyzed in each set is given at the bottom of each bar (summary of 2 different shPRC1 constructs). Two-sided Chi-squared test.

4.3.2 Silencing of *PRC1* prevents tumorigenicity *in vivo* via generating CIN-induced non-viable karyotypes

In order to see whether knockdown of *PRC1* affects tumor growth of xenografted EwS cells *in vivo*, two EwS cells with a Dox-inducible shRNA against *PRC1* were injected subcutaneously in immunocompromised NSG mice. *PRC1* knockdown was induced when tumors were palpable (~100 mm^3) via addition of Dox (2 mg/ml) to the drinking water. Knockdown of *PRC1* reduced growth of EwS xenografts but not in control group (**Figure 38a,b**). The knockdown efficacy of PRC1 was proved *ex vivo* by IHC (**Figure 38c**). Silenced-*PRC1* was associated with a profound decreasing in proliferation indicated by Ki-67 staining and with increased apoptosis indicated by CC3 staining (**Figure 38c**). Similar to observations *in vitro*, reduced tumor growth corresponded to a higher degree of nuclear pleomorphism and presence of so-called ‘monster’ cells with bizarre, aneuploid, and often multilobulated nuclei, as well as to higher rates of DNA double strand breaks as indicated by phospho-γH2AX stains *in vivo*. The human origin of ‘monster’ cells was validated by IHC using a human-specific anti-mitochondrial antibody (**Figure 38d,e**).

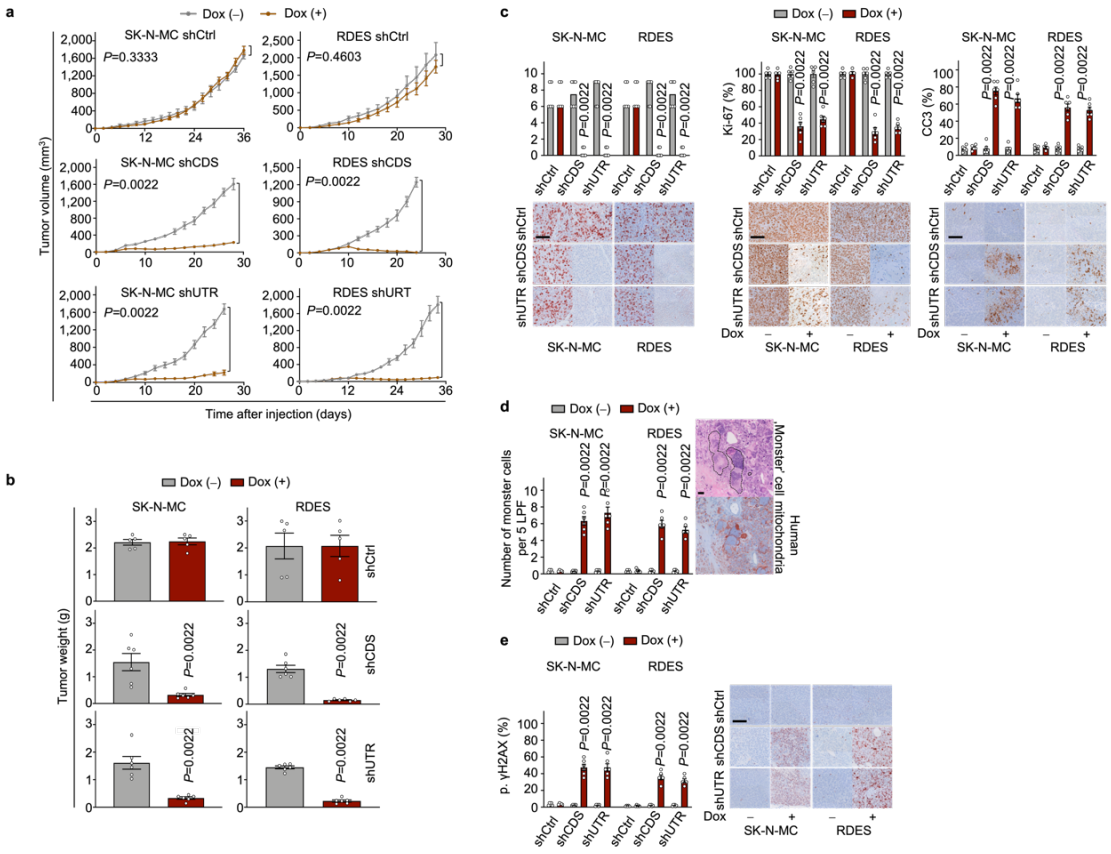

Figure 38 PRC1 contributes to proliferation and tumorigenesis in EwS *in vivo*

a) Tumor volume of RDES and SK-N-MC xenografts harboring either Dox-inducible shPRC1 constructs (shCDS/shUTR) or a non-targeting shCtrl. When tumors were palpable, mice were randomized and treated with either vehicle (–) or Dox (+). Data are mean and SEM, n≥5 animals per condition. P-values were calculated at the experimental endpoint; two-sided Mann-Whitney test. **b)** Tumor weight (g) of xenografts from SK-N-MC and RDES cells containing two Dox-inducible shPRC1 constructs (shCDS/shUTR) or a non-targeting shCtrl. Data are displayed as individual dots. Horizontal bars represent means and whiskers SEM, n≥5 animals per condition. **c)** Representative micrographs of xenografts stained by IHC for PRC1 (IRS), Ki-67 and cleaved caspase-3 (CC3), as well as corresponding quantifications of indicated parameters. Data are displayed as individual dots. Horizontal bars represent median IRS of PRC1 or means and whiskers SEM for positivity, respectively; n≥5 animals per condition; two-sided Mann-Whitney test; Scale bar=100 µm. **d)** Representative micrographs of xenografts stained with H&E and human mitochondria (mt), and quantification of 'monster' cells per low-power field (LPF) at 20× magnification. Data are displayed as individual dots. Horizontal bars represent means and whiskers SEM, n≥5 animals per condition; two-sided Mann-Whitney test; Scale bar=20 µm. **e)** Representative micrographs of xenografts stained by IHC for phospho-γH2AX, and its quantification per HPF. Data are displayed as individual dots. Horizontal bars represent means and whiskers SEM, n≥5 animals per condition; Two-sided Mann-Whitney test; Scale bar=100 µm.

In synopsis, the results suggested that PRC1 is critical for proper cell division in EwS, and that disruption of the delicate balance between mitosis and cytokinesis causes non-viable karyotypes in this otherwise genetically silent pediatric cancer.

4.4 Therapeutically targeting PRC1 via PLK1 inhibition in EwS

4.4.1 PRC1 expression confers sensitivity towards PLK1 inhibition *in vitro*

Since there are no direct inhibitors of PRC1 available to date, its major interacting partner PLK1 could serve as a surrogate target. PRC1 is a direct substrate of PLK1. PLK1 phosphorylates and binds to PRC1, which enables the formation of the PLK1:PRC1 complex critical for PLK1 translocation to the central spindle to initiate cytokinesis [68], [69]. Indeed, both genes were highly and significantly co-expressed in primary EwS tumors (n=196, rPearson=0.58, P=2.2-16) indicated by *Pearson* correlation analysis (**Figure 39a**). Thus, EwS models were treated with two small molecule ATP-competitive PLK1 inhibitors (BI2536, BI6727 [alias Volasertib]) being in clinical trials (**Appendix B**). Both inhibitors showed strong anti-proliferative effects on RDES and TC32 EwS cells at the lower nanomolar range (BI2536 ~5 nM, BI6727 ~20 nM) (**Figure 39b,c**). Even more strikingly, direct and indirect downregulation of *PRC1* either by RNA interference or genetic KO of the *PRC1*-associated GGAA-mSat dramatically diminished the sensitivity of EwS cells toward both PLK1 inhibitors (**Figure 39c**). In contrast, upregulation of PRC1 via CRISPR-mediated elongation of the *PRC1*-associated GGAA-mSat significantly increased their sensitivity toward both inhibitors (**Figure 39c**). To test the long-term effects of these inhibitors, 2D clonogenic and 3D sphere formation assays on RDES wt and TC32 wt cells applying the pre-determined median effective dose (ED50) of each respective inhibitor (BI2536 ~5 nM, BI6727 ~20 nM) was carried out. Both inhibitors strongly reduced clonogenic and spheroidal growth of RDES and TC32 EwS cells as compared to DMSO controls while inducing massive apoptosis (**Figure 38d-f**). In sum, these findings indicated that EwS cells with high *PRC1* expression are very sensitive to PLK1 inhibition, and that this sensitivity can be almost abolished by suppression of PRC1.

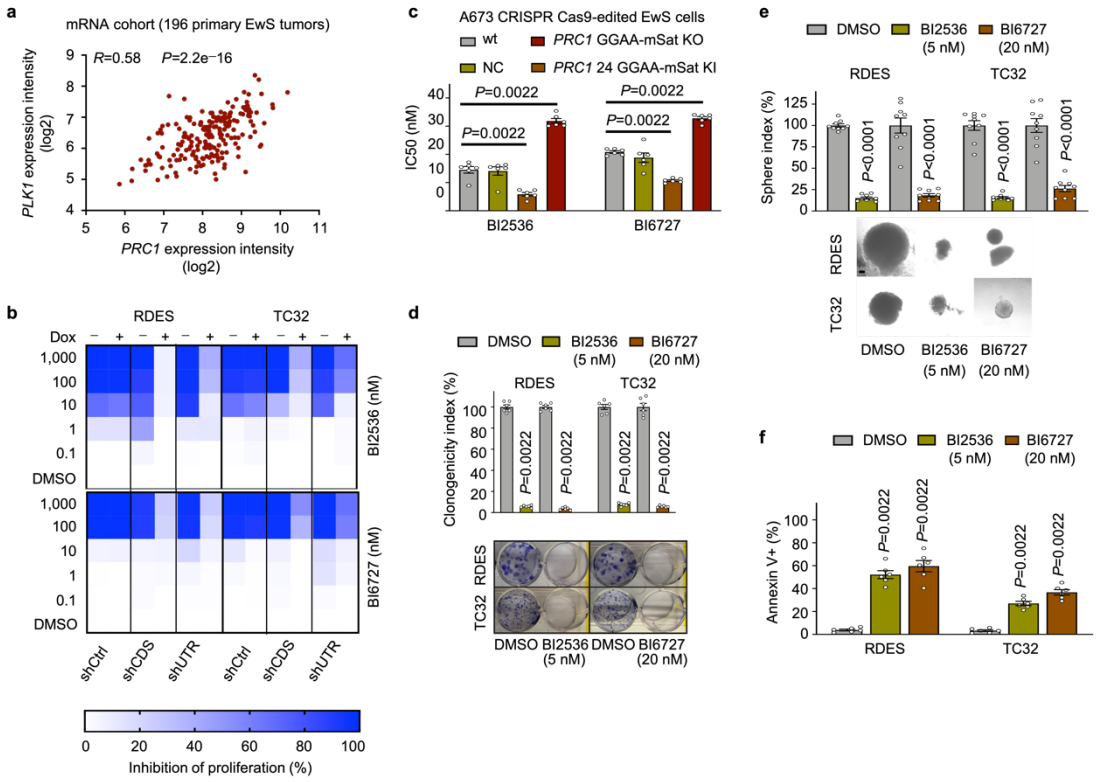

Figure 39 PRC1 primers EwS to PLK1 inhibition *in vitro*

a) Pearson correlation analysis of *PLK1* and *PRC1* mRNA expression levels in 196 primary EwS tumors. **b)** Heatmaps depicting the average percentage of growth inhibition in RDES and TC32 EwS cells containing either Dox-inducible specific shPRC1 (shCDS/shUTR) or non-targeting shCtrl constructs with/without Dox-treatment and after 72 h of PLK1 inhibition; n=6 biologically independent experiments. **c)** Inhibitory concentrations of 50% viability (IC50) in CRISPR Cas9-edited A673 EwS cells after 72 h of PLK1 inhibition. **d)** Colony-forming assays of RDES and TC32 cells treated with PLK1 inhibitor BI2536 or BI6727. **e)** Sphere formation assays of RDES and TC32 EwS cells treated with BI2536 or BI6727. Representative images of spheres are shown; Scale bar=50 µm. **f)** Analysis of apoptosis of RDES and TC32 EwS cells with/without PLK1 inhibition at indicated dose for 72 h using Annexin V/PI staining. For panel **c-f**, data are displayed as individual dots. Horizontal bars represent means and whiskers SEM, n=6-9 biologically independent experiments. Two-sided Mann-Whitney test.

4.4.2 PRC1 expression confers sensitivity towards PLK1 inhibition *in vivo*

To confirm the PRC1-dependency of PLK1 inhibition *in vivo*, CRISPR Cas9-initiated HDR edited A673 EwS cells were xenografted in NSG mice. Once tumors were palpable, mice were treated with BI2536 or BI6727 once per week via tail veil injection at clinically achievable dosages (**Figure 40a**). Treatment of mice xenografted with highly PRC1 expressing EwS cells led to strong inhibition of tumor growth and even tumor regression with massive genomic chaos after only

three cycles of treatment (**Figure 40b,c**) without overt adverse effects, such as weight loss (**Figure 40d**). Tumor regression was accompanied by induction of apoptosis and cell death as evidenced by significantly increased numbers of cells positive for CC3 and Ki67, respectively (**Figure 40e**). Such anti-tumor effects might be induced by generations of massive genomic chaos after PLK1 inhibition as indicated by a higher positivity of phosphor-γH2AX and significantly increased mitotic failure (**Figure 40d,e**). Remarkably, mice with total tumor regression did not show any sign of tumor recurrence up to 25 days after the last cycle as confirmed by necropsy and IHC (**Figure 40f,g**). In contrast, xenografts from A673 EwS cells with KO of the *PRC1*-associated GGAA-mSat exhibited delayed tumor growth and only progressive disease during treatment despite a 4th injection was administered (**Figure 40b-d**). Together, these findings suggested that genomically silent pediatric cancers, such as EwS, may be very sensitive to PLK1 inhibition in case of high PRC1 expression. In support of this notion, analysis of matched *in vivo* gene expression and drug-response data from pediatric tumor types (including EwS) [107] with relatively silent genomes revealed that good responses to BI6727 (Volasertib) were observed exclusively among *PRC1* high expressing xenografts (defined by median expression; P=0.0325, Fisher's exact test)—an effect not observed for PLK1 and MKI67 (**Table 21**).

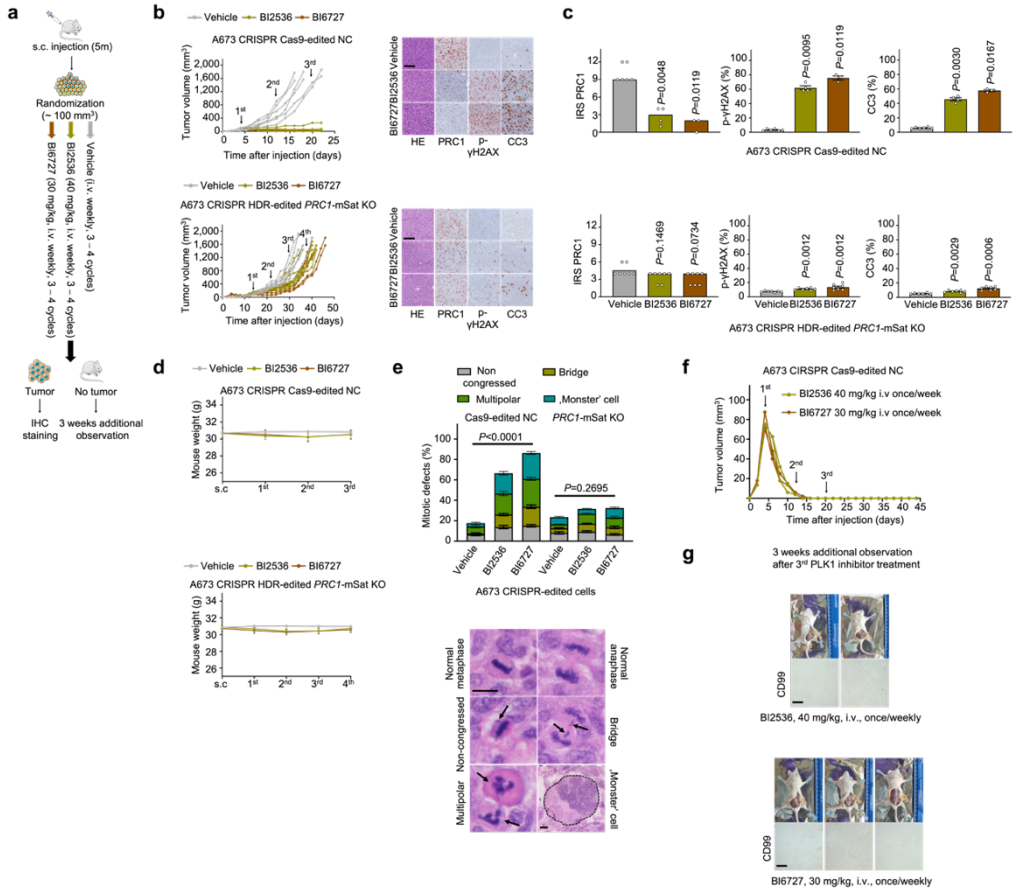

Figure 40 PRC1 primers EwS to PLK1 inhibition *in vivo*

a) Schematic of the experimental setting of PLK1 inhibitor treatment (BI2536, BI6727) *in vivo*. NSG mice were xenografted with A673 CRISPR Cas9-edited negative control (NC) cells and A673 CRISPR HDR-edited PRC1-associated GGAA-mSat KO cells. When tumors were palpable, mice were randomized and treated with either vehicle or PLK1 inhibitor BI2536 in a dose of 40 mg/kg or BI6727 in a dose of 30 mg/kg. **b)** For each condition, the tumor volume of ≥6 mice were plotted over the time of treatment as an individual line. Representative micrographs of H&E and PRC1 staining, positivity of CC3 as well as phospho-γH2AX per HPF. Scale bar=100 µm. **c)** Quantification of IRS of PRC1 and positivity of phospho-γH2AX and cleaved caspase-3 (CC3) per HPF of xenografts related to **b)**. Data are displayed as individual dots. Horizontal bars represent median IRS of PRC1 or means and whiskers SEM for positivity, respectively; *n*≥6 animals per condition; Two-sided Mann-Whitney test. **d)** Body weight of mice during intravenous PLK1 inhibitor treatment with BI2536 or BI6727. Dots represent means and whiskers SEM, *n*≥6 biologically independent animals per condition. **e)** Representative micrographs of xenografts stained with H&E related to **b)**. Quantification of the data are shown in pile-up bar plots depicting the percentage of mitotic defects in each condition (at least 30 mitoses per tumor were evaluated). Horizontal bars represent means and whiskers SEM, n=3–7 animals per condition; Two-sided Chi-squared test; Scale bar=10 µm. **f)** Tumor volume of A673 CRISPR Cas9-edited NC xenografts showing complete tumor regression during PLK1 inhibitor treatment and 25 d additional observation. **g)** Upper: Images of necropsy on A673 CRISPR Cas9-edited NC xenografts showing complete tumor regression after 3 cycles of PLK1 inhibitor treatment with BI2536 or BI6727 followed by 25 d additional observation. Lower: Immunohistological assessment of the injection site of the tumor cells stained with the human EwS-marker CD99. Scale bar=100 µm.

ID	Histology	*PRC1* expression	*PLK1* expression	*MKI67* expression	Response (Volasertib)	Response type
KT-14	Extracranial rhabdoid tumor	19.9114	11.5808	13.9151	PD1	Poor
KT-12	Atypical teratoid/rhabdoid tumor (ATRT)	27.4067	22.8022	18.2974	PD2	Poor
CHLA-79	Neuroblastoma	34.1437	21.5677	11.8097	PD1	Poor
KT-11	Wilms tumor	37.5781	29.6465	28.0239	PD2	Poor
TC-71	Ewing sarcoma	38.8586	27.779	14.1324	PD1	Poor
BT-29	Atypical teratoid/rhabdoid tumor (ATRT)	44.6578	29.15	18.2936	PD1	Poor
CHLA-258	Ewing sarcoma	55.245	51.1741	21.9456	PD1	Poor
KT-13	Wilms tumor	57.4319	48.3395	43.664	PD2	Poor
SK-NEP-1	Ewing sarcoma	62.8287	40.7332	25.9604	PD2	Poor
NB-1771	Neuroblastoma	64.346	25.5629	36.6809	PD2	Poor
NB-EBc1	Neuroblastoma	69.0028	43.4505	30.31	PD2	Poor
Rh-30R	Alveolar rhabdomyosarcoma	70.6508	33.9127	53.0211	CR	Good
NB-1643	Neuroblastoma	73.4423	33.4227	33.8688	SD	Good
Rh-10	Alveolar rhabdomyosarcoma	75.3155	44.0557	51.2629	PD1	Poor
KT-10	Wilms tumor	78.1368	31.3835	63.3262	PD1	Poor
EW-5	Ewing sarcoma	78.5027	69.6248	41.0436	PD1	Poor
Rh-30	Alveolar rhabdomyosarcoma	79.1408	32.4619	59.4743	PD2	Poor
NB-1691	Neuroblastoma	94.2106	51.5524	45.3638	CR	Good
NB-SD	Neuroblastoma	118.62	38.0142	50.511	CR	Good
	P value (good versus poor response)	0.0325	0.3034	0.3034		

Table 21 Analysis of matched *in vivo* gene expression and drug-response data from pediatric tumor types with relatively silent genomes [109]

4.4.3 PLK1 inhibitors synergize with chemotherapeutic drugs in a PRC1-dependent manner

In the clinical setting, Vincristine (VCR) and Doxorubicin (Doxo) are highly active chemotherapeutics employed in first-line treatment and relapsed EwS [33]. Hence, the potential synergistic effects of PLK1 inhibition with both drugs were studied in this thesis. As shown in **Figure 41a**, the microtubule-destabilizing drug VCR showed highly synergistic effects (positive Bliss score) at nanomolar concentrations in RDES cells, which was strongly diminished upon *PRC1* knockdown.

This *PRC1*-dependent effect was confirmed in TC32 EwS cells (**Figure 41b**), and corresponded to prior observations of synergy of BI6727 with VCR in this cell line [108]. This combination therapy also significantly reduced the necessary IC50 of PLK1 inhibitors (**Figure 41c**), which may help to mitigate their potential adverse effects. However, such synergistic effect was not observed for the intercalating drug Doxo across both cell lines and PLK1 inhibitors regardless of the *PRC1* levels (**Figure 42a**). Yet, it is noteworthy that both PLK1 inhibitors were still effective at nanomolar concentrations in EwS cell lines being highly resistant toward Doxo (**Figure 42b**), and that they could partially restore their Doxo-sensitivity (**Figure 41d,e**).

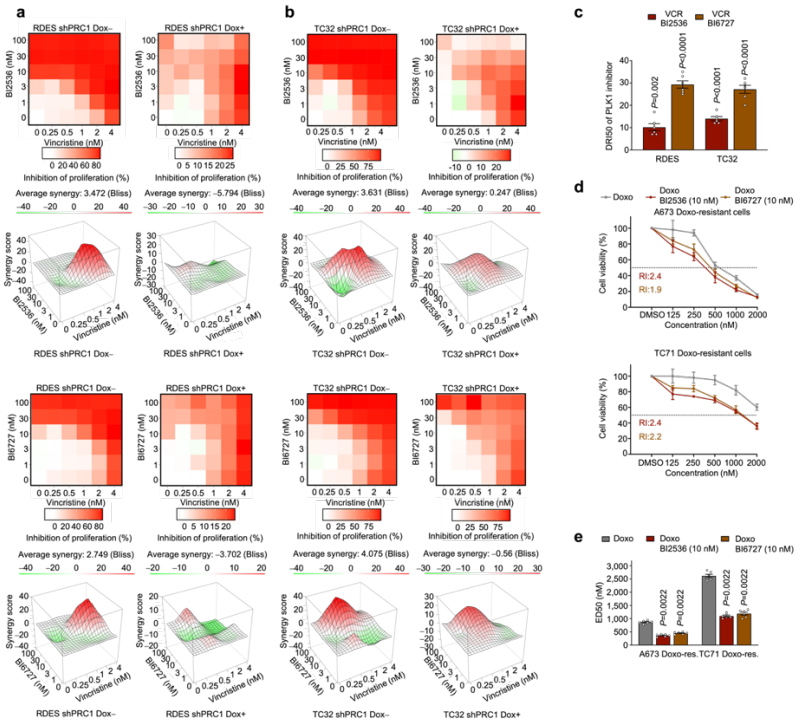

Figure 41 PLK1 inhibitors show synergistic effects when combined with chemo agents in EwS

a-b) Excess over Bliss analysis of RDES a) and TC32 cells **b)** with/without *PRC1* knockdown treated with combinations of Vincristine (VCR) and the PLK1 inhibitors BI2536 or BI6727 (red color indicates synergy). Summary level (mean) data from *n*=6 biologically independent experiments are shown. **c)** Dose reduction index (DRI) of PLK1 inhibitor BI2536 or BI6727 at IC50 level when combined with VCR in RDES and TC32 EwS cells. **d)** Dose-response curves of two Doxorubicin (Doxo)-resistant EwS cell lines A673 and TC71 treated with Doxo combined with PLK1 inhibitor BI2536 or BI6727 for 72 h. The reverse index (RI) is given. **e)** Median effective dose (ED50) for Doxo-treatment alone or in combination with PLK1 inhibitor BI2536 or BI6727 for 72 h in Doxo-resistant A673 and TC71 cells. Data are displayed as individual dots. Horizontal bars represent means and whiskers SEM, *n*=6 biologically independent experiments. Two-sided Mann-Whitney test in all panels.

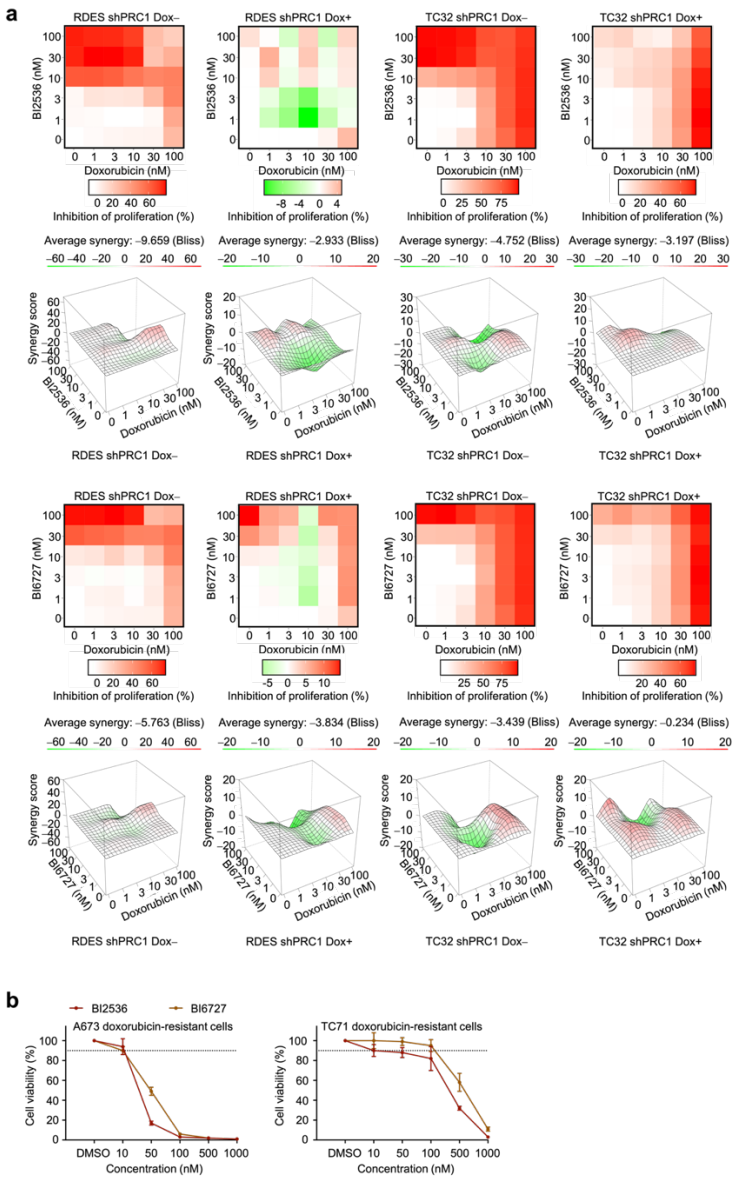

Figure 42 Combination test of PLK1 inhibitors with Doxorubicin in EwS cells

a) Excess over Bliss analysis of RDES and TC32 EwS cells with/without *PRC1* knockdown treated with combinations of Doxorubicin and the PLK1 inhibitors BI2536 or BI6727 (red color indicates synergy). Summary level data (means) from *n*=6 biologically independent experiments are shown. **b)** Dose response of two Doxorubicin-resistant (Doxo-res) EwS cell lines (A673, TC71) treated with the PLK1 inhibitors BI2536 or BI6727. Concentration of either PLK1 inhibitor below inhibitory concentrations of 90% viability (IC10) was defined as non-toxic (dashed lines). Dots represent means and whiskers SEM, *n*=6 biologically independent experiments.

In summary, these data indicated that PRC1-dependent PLK1 inhibitor treatment acts synergistically with other drugs employed in routine EwS therapy, and even is also effective against chemo-resistant EwS cells.

5. Discussion

CIN and cancer have been initially linked together by Theodor Boveri [109]. Although it is still unclear now how CIN-directed therapy seems to be a promising and novel cancer intervention [110]. Mitosis or cytokinesis defects can lead to CIN and chromosome mis-segregation [36]. EwS is genetically remarkably stable, containing a nearly diploid genome, with a single recurrent driver mutation EWSR1-FLI1 [33]. Although fruitful research findings were achieved in the biological field, exploitation of CIN-directed therapies still at its early stage in clinical. Thus, this thesis anticipates that properly exploiting CIN-induced treatment has great potential to affect clinical outcomes, especially in cancers with largely silent genomes, such as EwS.

The thesis aims at provoking cytokinesis failure by targeting PRC1 in EwS. The data represented in this thesis showed that PRC1 is heterogeneously overexpressed in EwS at both mRNA and protein level and its overexpression correlates with poor overall survival, and could additionally serve as an independent prognostic factor for EwS patients. More importantly, *PRC1* is the most overexpressed gene in EwS, which offers a large therapeutic window for a CIN-directed therapy. These findings indicate that the therapeutical potential of specifically targeting PRC1 in highly proliferating EwS cells is less toxic for normal tissues.

The data in this thesis demonstrated that the observed heterogenous PRC1 expression in EwS tumors may result from a direct regulation of EWSR1-FLI1, the major fusion oncoprotein in EwS. A distal *PRC1*-associated GGAA mSat bound by EWSR1-FLI1 showed strong length- and EWSR-FLI1-dependent enhancer activity in EwS cell lines. Moreover, epigenetically silencing or removing this GGAA-mSat significantly reduced *PRC1* expression and proliferation, while an epigenetic elongation of 24-GGAA motifs replaced by a natural 14-consequtive GGAA repeats significantly increased *PRC1* expression and cell viability. A *PRC1*-associated GGAA-mSat physically interacts with the promoter of *PRC1* through spatially forming a loop in the genome as shown in the 3C-PCR assay. The cooperation of a dominant cell cycle regulator (here PRC1) with polymorphic regulator elements (here GGAA-mSats), that are hitherto frequently considered as mere junk DNA, safeguards EwS genome stability required for disease-pro-

motion and explains the inter-individual diversity in clinical outcomes. This genetic mechanism shows how oncogenic hijacking of a cytokinesis regulator in cancer provides a rationale for novel targeted therapies.

GSEA followed by weighted correlation network analysis examined >285,000 transcripts and isoforms, revealing that *PRC1* had pleotropic effects on diverse cellular functions linked amongst others to DNA packaging, chromosome formation, cell morphology, and growth. Functional *in vitro* and *in vivo* experiments consistently showed a decreased proliferation followed by an increased apoptosis in the context of downregulated *PRC1* expression, suggesting an anti-tumor effect of PRC1 in EwS. The anti-tumor effects could be explained by excessive CIN resulting from cytokinesis defects upon *PRC1* knockdown. Indeed, there is an G2/M cell cycle arrest in *PRC1*-knockdown cells in EwS. These dividing tetraploid cells are susceptible to develop aneuploid cells because of, e.g., the extra number of centrosomes resulting in chromosome mis-segregation during mitosis [80], [111], [112]. FISH analyses using pan-centromere probes revealed that *PRC1* knockdown profoundly induced a greater amount of various mitotic defects and non-viable karyotypes compared to controls. Correspondingly, IHC staining revealed a higher degree of nuclear pleomorphism and the presence of so-called ‘monster’ cells with bizarre, aneuploid, and often multilobulated nuclei, as well as higher rates of DNA double strand breaks as indicated by phospho-gammaH2AX stains *in vivo,* which is supported by the finding of a new connection between cytokinesis and DNA damage [113].

An evolving interest in the polo-like kinase (PLK) family as an attractive therapeutic target in oncology has attracted massive attention for the last few decades. PLK1 is deemed extremely important because of its central role in mitosis and cytokinesis [114]. Notably, many cancers, including pediatric tumors, often overexpress PLK1 [115]. This interested is further warranted by the improved safety profile of PLK1 inhibitors versus classical mitotic drugs [116]. However, the responses to PLK1 inhibitors from different studies were discrepant, suggesting PLK1 inhibition (PLK1i) may not be propitious to all cancers [116], [117]. Therefore, highlighting predictive markers for vulnerability of cancer cells towards PLK1 inhibitors is of great interest to affect and/or foretell drug efficacy, which will finally be used to optimize therapy options for patients.

PRC1 interacts with PLK1 to directly recruit regulator proteins to the spindle midzone [61], [118]. Indeed, the results in this thesis showed a strong anti-proliferative effect of PLK1 inhibitor treatment on EwS cells at a relatively low dose, which was critically dependent on the intensity of PRC1 expression. Interestingly, such sensitivity of PLK1i to EwS cells did not depend on the TP53 status, which was previously confirmed in other cancer entities [119], [120]. Thus, EwS patients with mutant *TP53*, who normally present with more aggressive disease, could also benefit from PLK1 inhibitor treatment. Considering that PLK1i alone may be inefficient to completely cure patients, combining a PLK1 inhibitor with other chemo-agents could be necessary. It has been reported that some PLK1 inhibitors showed synergistic effects with microtubule-destabilizing agents such as VCR, in pediatric rhabdomyosarcomas and neuroblastoma cells [115], [121]. VCR is currently used as the standard 1st line combination chemotherapy for primary and relapsed EwS [122]. Similar to a previous paper showing the synergistic effect of a PLK1 inhibitor (BI6727) with VCR in EwS cells [108], the results in this thesis illustrated that PLK1 inhibitors (BI2536 and BI6727) when combined with VCR showed synergistic lethality via triggering massive cell apoptosis in EwS cells. It has been reported that the synergistic lethality could induce mitotic blockage followed by mitochondrial apoptosis through breaking down anti-apoptotic BCL2 proteins and caspase dependent/independent pathways [123]. Interestingly, PRC1 expression to a large extend determines the vulnerability of EwS cells towards PLK1i/VCR cotreatment, which might be explained by the fact that PLK1i/VCR induced mitotic arrest is required for apoptosis since preventing cells from entering mitosis significantly reduced PLK1i/VCR induced apoptosis [123]. Additionally, PLK1 inhibitors have been reported being able to overcome doxorubicin resistance in osteosarcoma [120]. In this thesis, the application of a PLK1 inhibitor was able to at least partially revert the resistance and restore the sensitivity of EwS cells toward doxorubicin, which might be mediated by inducing doxorubicin nuclear accumulation [120].

Collectively, the results in this thesis demonstrate that the EWSR1-FLI1-mediated high PRC1 expression sensitizes EwS cells towards PLK1i, and renders PRC1 as a promising predictive biomarker for therapies evoking cytokinesis defects and mitotic catastrophe (**Figure. 43**). CIN-directed therapies in cancers with largely silent genomes, such as EwS, seem to be a promising cancer intervention.

Still, careful biomarker-guided selection of patients is required to identify those patients who may benefit in particular from therapeutic modulation of CIN. In this regard, PLK4 inhibition was recently recognized as a therapeutic treatment option specifically for *TRIM37*-amplified neuroblastoma and breast cancer by causing centromere-dysfunction [124], [125]. Notably, the findings in this thesis also explain why previous preclinical testing of PLK1i in non-preselected EwS models may have yielded controversial results on its efficacy [107]. It is conceivable that the PRC1-related mechanism identified in EwS model may be translatable to other cancers for which immunohistochemical detection of high PRC1 levels could serve as a broadly available and inexpensive predictive biomarker.

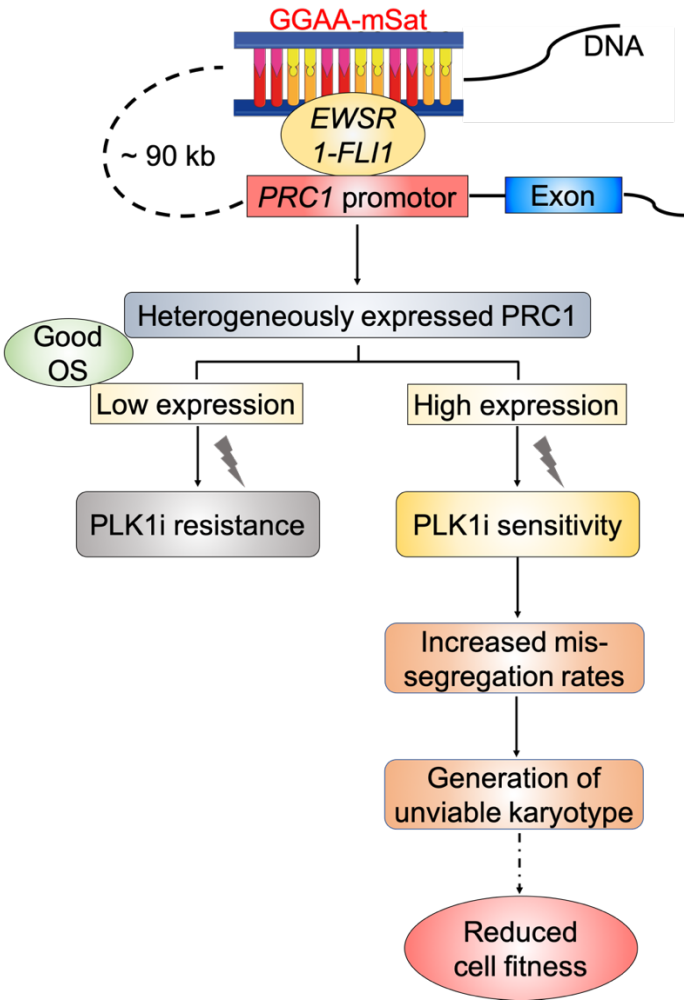

Figure 43 Schematic illustrating key findings of this study

EWSR1-FLI1-mediated high PRC1 expression through binding to a proximal enhancer-like GGAA-mSat in EwS promotes poor clinical outcomes while simultaneously creates a therapeutic vulnerability toward pharmacological PLK1 inhibition by triggering mitotic catastrophe.

6. Limitations and future perspective

In this thesis, the data demonstrates that EWSR1-FLI1-steered high PRC1 expression sensitizes EwS cells towards a PLK1 inhibitor, one broadly tested kinase inhibitor ripe for therapeutic exploitation yet with divergent responses. The results in this thesis indicate to render PRC1 as a promising predictive biomarker for therapies evoking cytokinesis defects and mitotic catastrophe, particularly in cancers with relatively ‚silent' genomes. However, to further solidify the PRC1-related mechanism of PLK1i and to successfully translate this pre-clinical finding to clinical application, there are several gaps needed to be fulfilled:

a) The prognostic value of PRC1 in EwS was consistently identified in two large retrospective cohorts in this thesis. A third perspective evaluation in another large cohort of EwS patients would be desirable for this quite rare disease.

b) Our work lacks the data from EwS patient-derived xenograft model (PDX) or EwS patients who received PLK1 inhibitor treatment in a clinical context. In this regard, the responses to PLK1 inhibition from real EwS tumors/patients can be collected to verify the value of PRC1 stratification for predicting PLK1 inhibitor treatment efficacy in a more robust and straightforward manner.

References

[1] S. F. Bakhoum and D. A. Landau, “Chromosomal Instability as a Driver of Tumor Heterogeneity and Evolution,” *Cold Spring Harb. Perspect. Med.*, vol. 7, no. 6, Jun. 2017, doi: 10.1101/cshperspect.a029611.

[2] S. Turajlic *et al.*, “Tracking Cancer Evolution Reveals Constrained Routes to Metastases: TRACERx Renal,” *Cell*, vol. 173, no. 3, pp. 581-594.e12, Apr. 2018, doi: 10.1016/j.cell.2018.03.057.

[3] S. L. Thompson and D. A. Compton, “Chromosomes and cancer cells,” *Chromosome Res.*, vol. 19, no. 3, pp. 433–444, Apr. 2011, doi: 10.1007/s10577-010-9179-y.

[4] J. Maciejowski, Y. Li, N. Bosco, P. J. Campbell, and T. de Lange, “Chromothripsis and Kataegis Induced by Telomere Crisis,” *Cell*, vol. 163, no. 7, pp. 1641–1654, Dec. 2015, doi: 10.1016/j.cell.2015.11.054.

[5] D. Cimini, B. Howell, P. Maddox, A. Khodjakov, F. Degrassi, and E. D. Salmon, “Merotelic Kinetochore Orientation Is a Major Mechanism of Aneuploidy in Mitotic Mammalian Tissue Cells,” *J. Cell Biol.*, vol. 153, no. 3, pp. 517–528, Apr. 2001.

[6] S. F. Bakhoum and L. C. Cantley, “The Multifaceted Role of Chromosomal Instability in Cancer and Its Microenvironment,” *Cell*, vol. 174, no. 6, pp. 1347–1360, 06 2018, doi: 10.1016/j.cell.2018.08.027.

[7] N. J. Birkbak *et al.*, “Paradoxical relationship between chromosomal instability and survival outcome in cancer,” *Cancer Res.*, vol. 71, no. 10, pp. 3447–3452, May 2011, doi: 10.1158/0008-5472.CAN-10-3667.

[8] M. E. Burkard and B. A. Weaver, “Tuning Chromosomal Instability to Optimize Tumor Fitness,” *Cancer Discov.*, vol. 7, no. 2, pp. 134–136, 2017, doi: 10.1158/2159-8290.CD-16-1415.

[9] H. H. Heng *et al.*, “Chromosomal instability (CIN): what it is and why it is crucial to cancer evolution,” *Cancer Metastasis Rev.*, vol. 32, no. 3–4, pp. 325–340, Dec. 2013, doi: 10.1007/s10555-013-9427-7.

[10] S. Santaguida *et al.*, “Chromosome Mis-segregation Generates Cell-Cycle-Arrested Cells with Complex Karyotypes that Are Eliminated by the Immune System,” *Dev. Cell*, vol. 41, no. 6, pp. 638-651.e5, Jun. 2017, doi: 10.1016/j.devcel.2017.05.022.

[11] J. M. Sheltzer *et al.*, “Single-chromosome Gains Commonly Function as Tumor Suppressors,” *Cancer Cell*, vol. 31, no. 2, pp. 240–255, Feb. 2017, doi: 10.1016/j.ccell.2016.12.004.

[12] E. M. Torres *et al.*, “Effects of aneuploidy on cellular physiology and cell division in haploid yeast,” *Science*, vol. 317, no. 5840, pp. 916–924, Aug. 2007, doi: 10.1126/science.1142210.

[13] A. D. Silk, L. M. Zasadil, A. J. Holland, B. Vitre, D. W. Cleveland, and B. A. Weaver, “Chromosome missegregation rate predicts whether aneuploidy will promote or suppress tumors,” *Proc. Natl. Acad. Sci.*, vol. 110, no. 44, pp. E4134–E4141, Oct. 2013, doi: 10.1073/pnas.1317042110.

[14] B. A. A. Weaver, A. D. Silk, C. Montagna, P. Verdier-Pinard, and D. W. Cleveland, “Aneuploidy acts both oncogenically and as a tumor suppressor,” *Cancer Cell*, vol. 11, no. 1, pp. 25–36, Jan. 2007, doi: 10.1016/j.ccr.2006.12.003.

[15] A. Janssen, G. J. P. L. Kops, and R. H. Medema, “Elevating the frequency of chromosome mis-segregation as a strategy to kill tumor cells,” *Proc. Natl. Acad. Sci.*, vol. 106, no. 45, pp. 19108–19113, Nov. 2009, doi: 10.1073/pnas.0904343106.

[16] P. V. Jallepalli and C. Lengauer, “Chromosome segregation and cancer: cutting through the mystery,” *Nat. Rev. Cancer*, vol. 1, no. 2, pp. 109–117, Nov. 2001, doi: 10.1038/35101065.

[17] L. Sansregret, B. Vanhaesebroeck, and C. Swanton, “Determinants and clinical implications of chromosomal instability in cancer,” *Nat. Rev. Clin. Oncol.*, vol. 15, no. 3, pp. 139–150, Mar. 2018, doi: 10.1038/nrclinonc.2017.198.

[18] F. Tirode, K. Laud-Duval, A. Prieur, B. Delorme, P. Charbord, and O. Delattre, “Mesenchymal stem cell features of Ewing tumors,” *Cancer Cell*, vol. 11, no. 5, pp. 421–429, May 2007, doi: 10.1016/j.ccr.2007.02.027.

[19] Y. Castillero-Trejo, S. Eliazer, L. Xiang, J. A. Richardson, and R. L. Ilaria, “Expression of the EWS/FLI-1 oncogene in murine primary bone-derived cells Results in EWS/FLI-1-dependent, ewing sarcoma-like tumors,” *Cancer Res.*, vol. 65, no. 19, pp. 8698–8705, Oct. 2005, doi: 10.1158/0008-5472.CAN-05-1704.

[20] A. N. Schuetz *et al.*, “Intercellular junctions in Ewing sarcoma/primitive neuroectodermal tumor: additional evidence of epithelial differentiation,” *Mod. Pathol. Off. J. U. S. Can. Acad. Pathol. Inc*, vol. 18, no. 11, pp. 1403–1410, Nov. 2005, doi: 10.1038/modpathol.3800435.

[21] A. Aurias, C. Rimbaut, D. Buffe, J. M. Zucker, and A. Mazabraud, “Translocation involving chromosome 22 in Ewing’s sarcoma. A cytogenetic study of four fresh tumors,” *Cancer Genet. Cytogenet.*, vol. 12, no. 1, pp. 21–25, May 1984, doi: 10.1016/0165-4608(84)90003-7.

[22] O. Delattre *et al.*, “Gene fusion with an ETS DNA-binding domain caused by chromosome translocation in human tumours,” *Nature*, vol. 359, no. 6391, pp. 162–165, Sep. 1992, doi: 10.1038/359162a0.

[23] T. G. P. Grünewald *et al.*, “Chimeric EWSR1-FLI1 regulates the Ewing sarcoma susceptibility gene EGR2 via a GGAA microsatellite,” *Nat. Genet.*, vol. 47, no. 9, pp. 1073–1078, Sep. 2015, doi: 10.1038/ng.3363.

[24] J. Zucman *et al.*, “Combinatorial generation of variable fusion proteins in the Ewing family of tumours.,” *EMBO J.*, vol. 12, no. 12, pp. 4481–4487, Dec. 1993.

[25] P. H. Sorensen, S. L. Lessnick, D. Lopez-Terrada, X. F. Liu, T. J. Triche, and C. T. Denny, “A second Ewing’s sarcoma translocation, t(21;22), fuses the EWS gene to another ETS-family transcription factor, ERG,” *Nat. Genet.*, vol. 6, no. 2, pp. 146–151, Feb. 1994, doi: 10.1038/ng0294-146.

[26] I. S. Jeon *et al.*, “A variant Ewing’s sarcoma translocation (7;22) fuses the EWS gene to the ETS gene ETV1,” *Oncogene*, vol. 10, no. 6, pp. 1229–1234, Mar. 1995.

[27] F. Urano *et al.*, “Molecular Analysis of Ewing’s Sarcoma: Another Fusion Gene, EWS-E1AF, Available for Diagnosis,” *Jpn. J. Cancer Res.*, vol. 89, no. 7, pp. 703–711, 1998, doi: 10.1111/j.1349-7006.1998.tb03274.x.

[28] M. Peter *et al.*, “A new member of the ETS family fused to EWS in Ewing tumors,” *Oncogene*, vol. 14, no. 10, Art. no. 10, Mar. 1997, doi: 10.1038/sj.onc.1200933.

[29] T. L. Ng *et al.*, “Ewing Sarcoma with Novel Translocation t(2;16) Producing an In-Frame Fusion of FUS and FEV,” *J. Mol. Diagn. JMD*, vol. 9, no. 4, pp. 459–463, Sep. 2007, doi: 10.2353/jmoldx.2007.070009.

[30] F. Tirode *et al.*, “Genomic landscape of Ewing sarcoma defines an aggressive subtype with co-association of STAG2 and TP53 mutations,” *Cancer Discov.*, vol. 4, no. 11, pp. 1342–1353, Nov. 2014, doi: 10.1158/2159-8290.CD-14-0622.

[31] C. M. Hattinger *et al.*, “Prognostic impact of chromosomal aberrations in Ewing tumours,” *Br. J. Cancer*, vol. 86, no. 11, pp. 1763–1769, Jun. 2002, doi: 10.1038/sj.bjc.6600332.

[32] P. Roberts *et al.*, “Ploidy and karyotype complexity are powerful prognostic indicators in the Ewing’s sarcoma family of tumors: a study by the United Kingdom Cancer Cytogenetics and the Children’s Cancer and Leukaemia Group,” *Genes. Chromosomes Cancer*, vol. 47, no. 3, pp. 207–220, Mar. 2008, doi: 10.1002/gcc.20523.

[33] T. G. P. Grünewald *et al.*, “Ewing sarcoma,” *Nat. Rev. Dis. Primer*, vol. 4, no. 1, p. 5, 05 2018, doi: 10.1038/s41572-018-0003-x.

[34] N. C. Sheffield *et al.*, “DNA methylation heterogeneity defines a disease spectrum in Ewing sarcoma,” *Nat. Med.*, vol. 23, no. 3, pp. 386–395, Mar. 2017, doi: 10.1038/nm.4273.

[35] N. Riggi *et al.*, “EWS-FLI1 Utilizes Divergent Chromatin Remodeling Mechanisms to Directly Activate or Repress Enhancer Elements in Ewing Sarcoma,” *Cancer Cell*, vol. 26, no. 5, pp. 668–681, Nov. 2014, doi: 10.1016/j.ccell.2014.10.004.

[36] K. M. Johnson *et al.*, “Role for the EWS domain of EWS/FLI in binding GGAA-microsatellites required for Ewing sarcoma anchorage independent growth,” *Proc. Natl. Acad. Sci.*, vol. 114, no. 37, pp. 9870–9875, Sep. 2017, doi: 10.1073/pnas.1701872114.

[37] G. Boulay *et al.*, “Cancer-Specific Retargeting of BAF Complexes by a Prion-like Domain,” *Cell*, vol. 171, no. 1, pp. 163-178.e19, Sep. 2017, doi: 10.1016/j.cell.2017.07.036.

[38] L. Dylla, C. Moore, and P. Jedlicka, “MicroRNAs in Ewing Sarcoma,” *Front. Oncol.*, vol. 3, Mar. 2013, doi: 10.3389/fonc.2013.00065.

[39] V. Y. Jo and C. D. M. Fletcher, “WHO classification of soft tissue tumours: an update based on the 2013 (4th) edition,” *Pathology (Phila.)*, vol. 46, no. 2, pp. 95–104, Feb. 2014, doi: 10.1097/PAT.0000000000000050.

[40] ESMO/European Sarcoma Network Working Group, “Bone sarcomas: ESMO Clinical Practice Guidelines for diagnosis, treatment and follow-up,” *Ann. Oncol. Off. J. Eur. Soc. Med. Oncol.*, vol. 25 Suppl 3, pp. iii113-123, Sep. 2014, doi: 10.1093/annonc/mdu256.

[41] I. M. Ambros, P. F. Ambros, S. Strehl, H. Kovar, H. Gadner, and M. Salzer-Kuntschik, “MIC2 is a specific marker for Ewing’s sarcoma and peripheral primitive neuroectodermal tumors. Evidence for a common histogenesis of Ewing’s sarcoma and peripheral primitive neuroectodermal tumors from MIC2 expression and specific chromosome aberration,” *Cancer*, vol. 67, no. 7, pp. 1886–1893, Apr. 1991, doi: 10.1002/1097-0142(19910401)67:7<1886::aid-cncr2820670712>3.0.co;2-u.

[42] M. F. Orth *et al.*, “High Specificity of BCL11B and GLG1 for EWSR1-FLI1 and EWSR1-ERG Positive Ewing Sarcoma,” *Cancers*, vol. 12, no. 3, Mar. 2020, doi: 10.3390/cancers12030644.

[43] P. H. Sorensen *et al.*, “Reverse transcriptase PCR amplification of EWS/FLI-1 fusion transcripts as a diagnostic test for peripheral primitive neuroectodermal tumors of childhood,” *Diagn. Mol. Pathol. Am. J. Surg. Pathol. Part B*, vol. 2, no. 3, pp. 147–157, Sep. 1993.

[44] N. J. Balamuth and R. B. Womer, “Ewing’s sarcoma,” *Lancet Oncol.*, vol. 11, no. 2, pp. 184–192, Feb. 2010, doi: 10.1016/S1470-2045(09)70286-4.

[45] “ISRCTN Registry.” https://www.isrctn.com/ (accessed Nov. 02, 2020).

[46] M. Stahl *et al.*, “Risk of recurrence and survival after relapse in patients with Ewing sarcoma,” *Pediatr. Blood Cancer*, vol. 57, no. 4, pp. 549–553, Oct. 2011, doi: 10.1002/pbc.23040.

[47] M. Rasper, S. Jabar, A. Ranft, H. Jürgens, S. Amler, and U. Dirksen, “The value of high-dose chemotherapy in patients with first relapsed Ewing sarcoma,” *Pediatr. Blood Cancer*, vol. 61, no. 8, pp. 1382–1386, Aug. 2014, doi: 10.1002/pbc.25042.

[48] F. I. Arnaldez and L. J. Helman, “New strategies in ewing sarcoma: lost in translation?,” *Clin. Cancer Res. Off. J. Am. Assoc. Cancer Res.*, vol. 20, no. 12, pp. 3050–3056, Jun. 2014, doi: 10.1158/1078-0432.CCR-13-0633.

[49] T. A. Potapova, J. Zhu, and R. Li, “Aneuploidy and chromosomal instability: a vicious cycle driving cellular evolution and cancer genome chaos,” *Cancer Metastasis Rev.*, vol. 32, no. 3–4, pp. 377–389, Dec. 2013, doi: 10.1007/s10555-013-9436-6.

[50] F. Baluska, D. Menzel, and P. W. Barlow, “Cytokinesis in plant and animal cells: endosomes ‘shut the door,’” *Dev. Biol.*, vol. 294, no. 1, pp. 1–10, Jun. 2006, doi: 10.1016/j.ydbio.2006.02.047.

[51] T. D. Pollard and B. O’Shaughnessy, “Molecular Mechanism of Cytokinesis,” *Annu. Rev. Biochem.*, vol. 88, pp. 661–689, 20 2019, doi: 10.1146/annurev-biochem-062917-012530.

[52] C. Mollinari, J.-P. Kleman, W. Jiang, G. Schoehn, T. Hunter, and R. L. Margolis, “PRC1 is a microtubule binding and bundling protein essential to maintain the mitotic spindle midzone,” *J. Cell Biol.*, vol. 157, no. 7, pp. 1175–1186, Jun. 2002, doi: 10.1083/jcb.200111052.

[53] W. Jiang *et al.*, “PRC1: a human mitotic spindle-associated CDK substrate protein required for cytokinesis,” *Mol. Cell*, vol. 2, no. 6, pp. 877–885, Dec. 1998.

[54] C. Zhu and W. Jiang, “Cell cycle-dependent translocation of PRC1 on the spindle by Kif4 is essential for midzone formation and cytokinesis,” *Proc. Natl. Acad. Sci. U. S. A.*, vol. 102, no. 2, pp. 343–348, Jan. 2005, doi: 10.1073/pnas.0408438102.

[55] R. Subramanian *et al.*, “Insights into antiparallel microtubule crosslinking by PRC1, a conserved nonmotor microtubule binding protein,” *Cell*, vol. 142, no. 3, pp. 433–443, Aug. 2010, doi: 10.1016/j.cell.2010.07.012.

[56] E. H. Kellogg *et al.*, “Near-atomic cryo-EM structure of PRC1 bound to the microtubule,” *Proc. Natl. Acad. Sci. U. S. A.*, vol. 113, no. 34, pp. 9430–9439, Aug. 2016, doi: 10.1073/pnas.1609903113.

[57] R. Subramanian, S.-C. Ti, L. Tan, S. A. Darst, and T. M. Kapoor, “Marking and measuring single microtubules by PRC1 and kinesin-4,” *Cell*, vol. 154, no. 2, pp. 377–390, Jul. 2013, doi: 10.1016/j.cell.2013.06.021.

[58] C. Zhu, E. Lau, R. Schwarzenbacher, E. Bossy-Wetzel, and W. Jiang, “Spatiotemporal control of spindle midzone formation by PRC1 in human cells,” *Proc. Natl. Acad. Sci. U. S. A.*, vol. 103, no. 16, pp. 6196–6201, Apr. 2006, doi: 10.1073/pnas.0506926103.

[59] Y. Abe *et al.*, “A mitotic kinase TOPK enhances Cdk1/cyclin B1-dependent phosphorylation of PRC1 and promotes cytokinesis,” *J. Mol. Biol.*, vol. 370, no. 2, pp. 231–245, Jul. 2007, doi: 10.1016/j.jmb.2007.04.067.

[60] M. Glotzer, “The 3Ms of central spindle assembly: microtubules, motors and MAPs,” *Nat. Rev. Mol. Cell Biol.*, vol. 10, no. 1, pp. 9–20, Jan. 2009, doi: 10.1038/nrm2609.

[61] C. Zhu, E. Bossy-Wetzel, and W. Jiang, “Recruitment of MKLP1 to the spindle midzone/midbody by INCENP is essential for midbody formation and completion of cytokinesis in human cells,” *Biochem. J.*, vol. 389, no. Pt 2, pp. 373–381, Jul. 2005, doi: 10.1042/BJ20050097.

[62] M. J. Cundell *et al.*, “The BEG (PP2A-B55/ENSA/Greatwall) pathway ensures cytokinesis follows chromosome separation,” *Mol. Cell*, vol. 52, no. 3, pp. 393–405, Nov. 2013, doi: 10.1016/j.molcel.2013.09.005.

[63] Y.-S. Seong *et al.*, “A spindle checkpoint arrest and a cytokinesis failure by the dominant-negative polo-box domain of Plk1 in U-2 OS cells,” *J. Biol. Chem.*, vol. 277, no. 35, pp. 32282–32293, Aug. 2002, doi: 10.1074/jbc.M202602200.

[64] A. E. H. Elia, L. C. Cantley, and M. B. Yaffe, “Proteomic screen finds pSer/pThr-binding domain localizing Plk1 to mitotic substrates,” *Science*, vol. 299, no. 5610, pp. 1228–1231, Feb. 2003, doi: 10.1126/science.1079079.

[65] H. H. W. Silljé and E. A. Nigg, “Capturing Polo Kinase,” *Science*, vol. 299, no. 5610, pp. 1190–1191, Feb. 2003, doi: 10.1126/science.1082384.

[66] F. A. Barr, H. H. W. Silljé, and E. A. Nigg, “Polo-like kinases and the orchestration of cell division,” *Nat. Rev. Mol. Cell Biol.*, vol. 5, no. 6, pp. 429–440, Jun. 2004, doi: 10.1038/nrm1401.

[67] D. M. Lowery, D. H. Mohammad, A. E. H. Elia, and M. B. Yaffe, “The Polo-box domain: a molecular integrator of mitotic kinase cascades and Polo-like kinase function,” *Cell Cycle Georget. Tex*, vol. 3, no. 2, pp. 128–131, Feb. 2004.

[68] R. Neef *et al.*, “Choice of Plk1 docking partners during mitosis and cytokinesis is controlled by the activation state of Cdk1,” *Nat. Cell Biol.*, vol. 9, no. 4, pp. 436–444, Apr. 2007, doi: 10.1038/ncb1557.

[69] C.-K. Hu, M. Coughlin, and T. J. Mitchison, “Midbody assembly and its regulation during cytokinesis,” *Mol. Biol. Cell*, vol. 23, no. 6, pp. 1024–1034, Mar. 2012, doi: 10.1091/mbc.E11-08-0721.

[70] J. Li, M. Dallmayer, T. Kirchner, J. Musa, and T. G. P. Grünewald, “PRC1: Linking Cytokinesis, Chromosomal Instability, and Cancer Evolution,” *Trends Cancer*, vol. 4, no. 1, pp. 59–73, 2018, doi: 10.1016/j.trecan.2017.11.002.

[71] E. K. Kieserman, M. Glotzer, and J. B. Wallingford, “Developmental regulation of central spindle assembly and cytokinesis during vertebrate embryogenesis,” *Curr. Biol. CB*, vol. 18, no. 2, pp. 116–123, Jan. 2008, doi: 10.1016/j.cub.2007.12.028.

[72] C. E. Walczak and S. L. Shaw, “A MAP for bundling microtubules,” *Cell*, vol. 142, no. 3, pp. 364–367, Aug. 2010, doi: 10.1016/j.cell.2010.07.023.

[73] G. Maton *et al.*, “Kinetochore components are required for central spindle assembly,” *Nat. Cell Biol.*, vol. 17, no. 5, pp. 697–705, May 2015, doi: 10.1038/ncb3150.

[74] S. Watanabe, T. De Zan, T. Ishizaki, and S. Narumiya, “Citron kinase mediates transition from constriction to abscission through its coiled-coil domain,” *J. Cell Sci.*, vol. 126, no. Pt 8, pp. 1773–1784, Apr. 2013, doi: 10.1242/jcs.116608.

[75] U. Gruneberg *et al.*, “KIF14 and citron kinase act together to promote efficient cytokinesis,” *J. Cell Biol.*, vol. 172, no. 3, pp. 363–372, Jan. 2006, doi: 10.1083/jcb.200511061.

[76] Z. I. Bassi, M. Audusseau, M. G. Riparbelli, G. Callaini, and P. P. D’Avino, “Citron kinase controls a molecular network required for midbody formation in cytokinesis,” *Proc. Natl. Acad. Sci. U. S. A.*, vol. 110, no. 24, pp. 9782–9787, Jun. 2013, doi: 10.1073/pnas.1301328110.

[77] J. Kajtez *et al.*, “Overlap microtubules link sister k-fibres and balance the forces on bi-oriented kinetochores,” *Nat. Commun.*, vol. 7, p. 10298, Jan. 2016, doi: 10.1038/ncomms10298.

[78] S. L. Carter, A. C. Eklund, I. S. Kohane, L. N. Harris, and Z. Szallasi, “A signature of chromosomal instability inferred from gene expression profiles predicts clinical outcome in multiple human cancers,” *Nat. Genet.*, vol. 38, no. 9, pp. 1043–1048, Sep. 2006, doi: 10.1038/ng1861.

[79] S. M. Dewhurst *et al.*, “Tolerance of whole-genome doubling propagates chromosomal instability and accelerates cancer genome evolution,” *Cancer Discov.*, vol. 4, no. 2, pp. 175–185, Feb. 2014, doi: 10.1158/2159-8290.CD-13-0285.

[80] N. J. Ganem, S. A. Godinho, and D. Pellman, “A mechanism linking extra centrosomes to chromosomal instability,” *Nature*, vol. 460, no. 7252, pp. 278–282, Jul. 2009, doi: 10.1038/nature08136.

[81] L. T. Vassilev *et al.*, “Selective small-molecule inhibitor reveals critical mitotic functions of human CDK1,” *Proc. Natl. Acad. Sci. U. S. A.*, vol. 103, no. 28, pp. 10660–10665, Jul. 2006, doi: 10.1073/pnas.0600447103.

[82] A. T. Das, L. Tenenbaum, and B. Berkhout, “Tet-On Systems For Doxycycline-inducible Gene Expression,” *Curr. Gene Ther.*, vol. 16, no. 3, pp. 156–167, Jun. 2016, doi: 10.2174/1566523216666160524144041.

[83] D. Wiederschain *et al.*, “Single-vector inducible lentiviral RNAi system for oncology target validation,” *Cell Cycle Georget. Tex*, vol. 8, no. 3, pp. 498–504, Feb. 2009, doi: 10.4161/cc.8.3.7701.

[84] D. J. Giard *et al.*, “In vitro cultivation of human tumors: establishment of cell lines derived from a series of solid tumors,” *J. Natl. Cancer Inst.*, vol. 51, no. 5, pp. 1417–1423, Nov. 1973, doi: 10.1093/jnci/51.5.1417.

[85] W. A. May *et al.*, “Characterization and drug resistance patterns of Ewing’s sarcoma family tumor cell lines,” *PloS One*, vol. 8, no. 12, p. e80060, 2013, doi: 10.1371/journal.pone.0080060.

[86] K. J. Livak and T. D. Schmittgen, “Analysis of relative gene expression data using real-time quantitative PCR and the 2(-Delta Delta C(T)) Method,” *Methods San Diego Calif*, vol. 25, no. 4, pp. 402–408, Dec. 2001, doi: 10.1006/meth.2001.1262.

[87] H. Hagège *et al.*, “Quantitative analysis of chromosome conformation capture assays (3C-qPCR),” *Nat. Protoc.*, vol. 2, no. 7, pp. 1722–1733, Jul. 2007, doi: 10.1038/nprot.2007.243.

[88] M. M. Bradford, “A rapid and sensitive method for the quantitation of microgram quantities of protein utilizing the principle of protein-dye binding,” *Anal. Biochem.*, vol. 72, pp. 248–254, May 1976, doi: 10.1006/abio.1976.9999.

[89] L. He *et al.*, “Methods for High-throughput Drug Combination Screening and Synergy Scoring,” *Methods Mol. Biol. Clifton NJ*, vol. 1711, pp. 351–398, 2018, doi: 10.1007/978-1-4939-7493-1_17.

[90] N. Zhang, J.-N. Fu, and T.-C. Chou, “Synergistic combination of microtubule targeting anticancer fludelone with cytoprotective panaxytriol derived from panax ginseng against MX-1 cells in vitro: experimental design and data analysis using the combination index method,” *Am. J. Cancer Res.*, vol. 6, no. 1, pp. 97–104, Dec. 2015.

[91] *ISCN 1995 | Karger Book. An Int. System for Human Cytogenetic Nomenclature (1995)*. .

[92] M. C. Baldauf *et al.*, “Robust diagnosis of Ewing sarcoma by immunohistochemical detection of super-enhancer-driven EWSR1-ETS targets,” *Oncotarget*, vol. 9, no. 2, pp. 1587–1601, Jan. 2018, doi: 10.18632/oncotarget.20098.

[93] G. Sannino *et al.*, “Gene expression and immunohistochemical analyses identify SOX2 as major risk factor for overall survival and relapse in Ewing sarcoma patients,” *EBioMedicine*, Aug. 2019, doi: 10.1016/j.ebiom.2019.08.002.

[94] M. C. Baldauf *et al.*, “Systematic identification of cancer-specific MHC-binding peptides with RAVEN,” *Oncoimmunology*, vol. 7, no. 9, p. e1481558, 2018, doi: 10.1080/2162402X.2018.1481558.

[95] M. E. Ritchie *et al.*, “limma powers differential expression analyses for RNA-sequencing and microarray studies,” *Nucleic Acids Res.*, vol. 43, no. 7, pp. e47–e47, Apr. 2015, doi: 10.1093/nar/gkv007.

[96] G. Yu, L.-G. Wang, Y. Han, and Q.-Y. He, “clusterProfiler: an R Package for Comparing Biological Themes Among Gene Clusters,” *OMICS J. Integr. Biol.*, vol. 16, no. 5, pp. 284–287, Mar. 2012, doi: 10.1089/omi.2011.0118.

[97] M. Dallmayer *et al.*, “Targeting the CALCB/RAMP1 axis inhibits growth of Ewing sarcoma,” *Cell Death Dis.*, vol. 10, no. 2, Art. no. 2, Feb. 2019, doi: 10.1038/s41419-019-1372-0.

[98] A. Subramanian *et al.*, “Gene set enrichment analysis: a knowledge-based approach for interpreting genome-wide expression profiles,” *Proc. Natl. Acad. Sci. U. S. A.*, vol. 102, no. 43, pp. 15545–15550, Oct. 2005, doi: 10.1073/pnas.0506580102.

[99] A. A. Sergushichev, “An algorithm for fast preranked gene set enrichment analysis using cumulative statistic calculation,” *bioRxiv*, p. 060012, Jun. 2016, doi: 10.1101/060012.

[100] S. M. Waszak *et al.*, “Germline Elongator mutations in Sonic Hedgehog medulloblastoma,” *Nature*, vol. 580, no. 7803, Art. no. 7803, Apr. 2020, doi: 10.1038/s41586-020-2164-5.

[101] N. S, G. Vg, and H. Td, “Genomic instability--an evolving hallmark of cancer,” *Nature reviews. Molecular cell biology*, Mar. 2010. https://pubmed.ncbi.nlm.nih.gov/20177397/ (accessed Sep. 21, 2020).

[102] “The Genomic Landscape of Pediatric Ewing Sarcoma | Cancer Discovery.” https://cancerdiscovery.aacrjournals.org/content/4/11/1326 (accessed Aug. 10, 2020).

[103] C. Mollinari *et al.*, “Ablation of PRC1 by Small Interfering RNA Demonstrates that Cytokinetic Abscission Requires a Central Spindle Bundle in Mammalian Cells, whereas Completion of Furrowing Does Not,” *Mol. Biol. Cell*, vol. 16, no. 3, pp. 1043–1055, Mar. 2005, doi: 10.1091/mbc.E04-04-0346.

[104] J. Li, M. Dallmayer, T. Kirchner, J. Musa, and T. G. P. Grünewald, "PRC1: Linking Cytokinesis, Chromosomal Instability, and Cancer Evolution," *Trends Cancer*, vol. 4, no. 1, pp. 59–73, 2018, doi: 10.1016/j.trecan.2017.11.002.

[105] M. C. Baldauf *et al.*, "Systematic identification of cancer-specific MHC-binding peptides with RAVEN," *OncoImmunology*, vol. 7, no. 9, p. e1481558, Sep. 2018, doi: 10.1080/2162402X.2018.1481558.

[106] J. Carrillo *et al.*, "Cholecystokinin Down-Regulation by RNA Interference Impairs Ewing Tumor Growth," *Clin. Cancer Res.*, vol. 13, no. 8, pp. 2429–2440, Apr. 2007, doi: 10.1158/1078-0432.CCR-06-1762.

[107] R. Gorlick *et al.*, "Initial testing (stage 1) of the Polo-like kinase inhibitor volasertib (BI 6727), by the Pediatric Preclinical Testing Program," *Pediatr. Blood Cancer*, vol. 61, no. 1, pp. 158–164, Jan. 2014, doi: 10.1002/pbc.24616.

[108] L. M. Weiß, M. Hugle, S. Romero, and S. Fulda, "Synergistic induction of apoptosis by a polo-like kinase 1 inhibitor and microtubule-interfering drugs in Ewing sarcoma cells," *Int. J. Cancer*, vol. 138, no. 2, pp. 497–506, Jan. 2016, doi: 10.1002/ijc.29725.

[109] T. Boveri, "Concerning the origin of malignant tumours by Theodor Boveri. Translated and annotated by Henry Harris," *J. Cell Sci.*, vol. 121 Suppl 1, pp. 1–84, Jan. 2008, doi: 10.1242/jcs.025742.

[110] A. V Roschke and I. R Kirsch, "Targeting karyotypic complexity and chromosomal instability of cancer cells," *Curr. Drug Targets*, vol. 11, no. 10, pp. 1341–1350, 2010.

[111] W. T. Silkworth, I. K. Nardi, L. M. Scholl, and D. Cimini, "Multipolar spindle pole coalescence is a major source of kinetochore mis-attachment and chromosome mis-segregation in cancer cells," *PloS One*, vol. 4, no. 8, p. e6564, Aug. 2009, doi: 10.1371/journal.pone.0006564.

[112] H. Tanaka *et al.*, "Cytokinetic Failure-induced Tetraploidy Develops into Aneuploidy, Triggering Skin Aging in Phosphovimentin-deficient Mice," *J. Biol. Chem.*, vol. 290, no. 21, pp. 12984–12998, May 2015, doi: 10.1074/jbc.M114.633891.

[113] Fraschini, "Cytokinesis in Eukaryotic Cells: The Furrow Complexity at a Glance | Kopernio." https://kopernio.com/viewer?doi=10.3390/cells9020271&token=WzE1MjM0OTMsIjEwLjMzOTAvY2VsbHM5MDIwMjcxIl0.Jg7jMU-JBYu6fGdXp6JnMAYO5RvY (accessed Feb. 18, 2020).

[114] T. Takaki, K. Trenz, V. Costanzo, and M. Petronczki, "Polo-like kinase 1 reaches beyond mitosis—cytokinesis, DNA damage response, and development," *Curr.*

Opin. Cell Biol., vol. 20, no. 6, pp. 650–660, Dec. 2008, doi: 10.1016/j.ceb.2008.10.005.

[115] S. A. Gatz *et al.*, "A Perspective on Polo-Like Kinase-1 Inhibition for the Treatment of Rhabdomyosarcomas," *Front. Oncol.*, vol. 9, Nov. 2019, doi: 10.3389/fonc.2019.01271.

[116] K. S. Lee, T. R. Burke, J.-E. Park, J. K. Bang, and E. Lee, "Recent Advances and New Strategies in Targeting Plk1 for Anticancer Therapy," *Trends Pharmacol. Sci.*, vol. 36, no. 12, pp. 858–877, Dec. 2015, doi: 10.1016/j.tips.2015.08.013.

[117] R. E. A. Gutteridge, M. A. Ndiaye, X. Liu, and N. Ahmad, "Plk1 Inhibitors in Cancer Therapy: From Laboratory to Clinics," *Mol. Cancer Ther.*, vol. 15, no. 7, pp. 1427–1435, 2016, doi: 10.1158/1535-7163.MCT-15-0897.

[118] Y. Kurasawa, W. C. Earnshaw, Y. Mochizuki, N. Dohmae, and K. Todokoro, "Essential roles of KIF4 and its binding partner PRC1 in organized central spindle midzone formation," *EMBO J.*, vol. 23, no. 16, pp. 3237–3248, Aug. 2004, doi: 10.1038/sj.emboj.7600347.

[119] F. Louwen and J. Yuan, "Battle of the eternal rivals: restoring functional p53 and inhibiting Polo-like kinase 1 as cancer therapy," *Oncotarget*, vol. 4, no. 7, pp. 958–971, Jul. 2013.

[120] V. Sero *et al.*, "Targeting polo-like kinase 1 by NMS-P937 in osteosarcoma cell lines inhibits tumor cell growth and partially overcomes drug resistance," *Invest. New Drugs*, vol. 32, no. 6, pp. 1167–1180, Dec. 2014, doi: 10.1007/s10637-014-0158-6.

[121] S. Czaplinski, M. Hugle, V. Stiehl, and S. Fulda, "Polo-like kinase 1 inhibition sensitizes neuroblastoma cells for vinca alkaloid-induced apoptosis," *Oncotarget*, vol. 7, no. 8, pp. 8700–8711, May 2015, doi: 10.18632/oncotarget.3901.

[122] N. Gaspar *et al.*, "Ewing Sarcoma: Current Management and Future Approaches Through Collaboration," *J. Clin. Oncol. Off. J. Am. Soc. Clin. Oncol.*, vol. 33, no. 27, pp. 3036–3046, Sep. 2015, doi: 10.1200/JCO.2014.59.5256.

[123] M. Hugle, K. Belz, and S. Fulda, "Identification of synthetic lethality of PLK1 inhibition and microtubule-destabilizing drugs," *Cell Death Differ.*, vol. 22, no. 12, pp. 1946–1956, Dec. 2015, doi: 10.1038/cdd.2015.59.

[124] F. Meitinger *et al.*, "TRIM37 controls cancer-specific vulnerability to PLK4 inhibition," *Nature*, Sep. 2020, doi: 10.1038/s41586-020-2710-1.

[125] Z. Y. Yeow *et al.*, "Targeting TRIM37-driven centrosome dysfunction in 17q23-amplified breast cancer," *Nature*, Sep. 2020, doi: 10.1038/s41586-020-2690-1.

Appendix A: GSEA results upon *PRC1* knockdown

Pathway	*P*-value (adjusted)	NES
GO_MATURATION_OF_5_8S_RRNA	0.008806614	2.3038047
GO_SPLICEOSOMAL_TRI_SNRNP_COMPLEX	0.009372064	2.30114
GO_MATURATION_OF_SSU_RRNA	0.00985258	2.1500123
GO_REGULATION_OF_PROTEIN_POLYUBIQUITINATION	0.008061762	2.09080316
GO_APICAL_PART_OF_CELL	0.005259368	-1.7513334
GO_SENSORY_ORGAN_MORPHOGENESIS	0.006701649	-1.7520153
GO_CALMODULIN_BINDING	0.006701649	-1.7541509
GO_BONE_DEVELOPMENT	0.005259368	-1.7572234
GO_CELL_DIVISION	0.005259368	-1.7647592
GO_CALCIUM_ION_TRANSMEMBRANE_TRANSPORT	0.005259368	-1.7682016
GO_MICROTUBULE_BINDING	0.005259368	-1.7732232
GO_EPITHELIAL_CELL_DEVELOPMENT	0.006701649	-1.7955944
GO_AXON_DEVELOPMENT	0.005259368	-1.7989699
GO_MICROTUBULE_ASSOCIATED_COMPLEX	0.006701649	-1.8025688
GO_MICROTUBULE_CYTOSKELETON_ORGANIZATION	0.005259368	-1.8039794
GO_SPINDLE_POLE	0.005259368	-1.8063112
GO_EXTRACELLULAR_STRUCTURE_ORGANIZATION	0.005259368	-1.8067486
GO_FOREBRAIN_DEVELOPMENT	0.005259368	-1.8085248
GO_CELL_SUBSTRATE_ADHESION	0.005259368	-1.8180133
GO_REGULATION_OF_NERVOUS_SYSTEM_DEVELOPMENT	0.005259368	-1.8216658
GO_FAT_CELL_DIFFERENTIATION	0.005259368	-1.8316975
GO_EXTRACELLULAR_MATRIX	0.005259368	-1.8576189
GO_GROWTH_FACTOR_BINDING	0.008913796	-1.8594985
GO_CHONDROCYTE_DIFFERENTIATION	0.008913796	-1.8618331
GO_MITOTIC_NUCLEAR_DIVISION	0.005259368	-1.871198
GO_CONDENSED_CHROMOSOME_CENTROMERIC_REGION	0.005259368	-1.8764235
GO_CALCIUM_ION_TRANSMEMBRANE_TRANSPORTER_ACTIVITY	0.006989604	-1.8952211
GO_POLYOL_METABOLIC_PROCESS	0.009200077	-1.9068411
GO_MAINTENANCE_OF_LOCATION	0.005259368	-1.9291997
GO_BASOLATERAL_PLASMA_MEMBRANE	0.005259368	-1.9566709
GO_CEREBRAL_CORTEX_DEVELOPMENT	0.005259368	-1.9839783
GO_NEURON_MIGRATION	0.005259368	-1.9887176
GO_NEGATIVE_REGULATION_OF_GENE_EXPRESSION_EPIGENETIC	0.005259368	-2.0290812
GO_GLIAL_CELL_ACTIVATION	0.005872163	-2.0572492
GO_NEGATIVE_REGULATION_OF_CHROMATIN_ORGANIZATION	0.005353443	-2.0599932
GO_NEGATIVE_REGULATION_OF_GENE_SILENCING	0.005725357	-2.1035647
GO_PROTEIN_DNA_COMPLEX	0.005259368	-2.1512822

GO_NUCLEOSOME_ORGANIZATION	0.005259368	-2.2260644
GO_CHROMATIN_ASSEMBLY	0.005259368	-2.3250757
GO_DNA_PACKAGING_COMPLEX	0.005259368	-2.4905418

Appendix B: Summary of clinical trials for PLK1 inhibitor BI2536 and BI6727

Drug	Study title	NCT number
BI2536	Open, Randomized Phase II Trial to Investigate the Efficacy and Safety of the PLK-1 Inhibitor BI 2536 in Patients With Advanced, Unresectable Pancreatic Cancer	NCT00710710
	Dose Escalation Study of BI 2536 BS in Patients With Advanced Solid Tumours With Repeated Administration in Patients With Clinical Benefit	NCT02211859
	Dose Escalation Study of BI 2536 With Pemetrexed in Previously Treated Patients With Non-small-cell Lung Cancer	NCT02211833
	BI 2536 BS in Patients With Advanced Solid Tumours and Repeated Administration in Patients With Clinical Benefit	NCT02211872
	Dose-finding Study of BI 2536 Administered in Combination With Gemcitabine in Patients With Locally Advanced or Metastatic Pancreatic Cancer	NCT02215044
	BI 2536 Infusional Treatment in Patients Over 60 Years of Age With Refractory or Relapsed Acute Myeloid Leukaemia	NCT00701766
	Efficacy and Safety of BI 2536 in Advanced or Metastatic Non-Small Cell Lung Cancer	NCT00376623
	BI 2536 Second Line Monotherapy in SCLC	NCT00412880
	Phase II Study of BI 2536 in Prostate Cancer	NCT00706498
	Investigation of Safety, Tolerability and Maximum Tolerated Dose (MTD) of BI 2536 in Patients With Recurrent Advanced Aggressive Non-Hodgkin's Lymphoma (NHL)	NCT00243087
	BI 2536 in Treating Patients With Recurrent or Metastatic Solid Tumors	NCT00526149
BI6727	Volasertib in Japanese Patients With Acute Myeloid Leukemia (AML)	NCT01662505
	BI 6727 (Volasertib) Human ADME Trial in Various Solid Tumours	NCT01145885
	BI 6727 (Volasertib) Monotherapy Phase I Trial in Japanese Patients With Advanced Solid Tumours	NCT01348347
	BI 6727 (Volasertib) in Combination With Cisplatin or Carboplatin in Patients With Advanced or Metastatic Solid Tumor	NCT00969761
	Volasertib + Decitabine in Patients With Acute Myeloid Leukemia (AML)	NCT02003573
	A Study of Volasertib Plus Induction Chemotherapy for Acute Myeloid Leukemia	NCT02527174
	BI 6727 Administered Intravenously Every 3 Weeks in Patients With Solid Tumours	NCT02273388

	Volasertib Combined With Induction Chemotherapy in Acute Myeloid Leukemia	NCT02905994
	Volasertib and Vincristine Sulfate Liposome in Treating Patients With Relapsed or Refractory Acute Lymphoblastic Leukemia	NCT02861040
	A Study to Find a Safe Dose of Volasertib Given in Addition to Standard Salvage Chemotherapy in Children (Age 3 Months to Less Than 18 Years) With Acute Myeloid Leukaemia, in Whom Front-line Chemotherapy Failed	NCT02722135
	Investigation of Potential Drug-drug Interaction of Volasertib With Itraconazole in Patients With Various Tumours	NCT01772563
	An Open Label Phase I Dose Escalation Trial of Intravenous BI 6727 (Volasertib)in Combination With Oral BIBW 2992 (Afatinib) in Patients With Advanced Solid Tumours	NCT01206816
	Dose Finding Study of BI 6727 (Volasertib) in Patients With Various Solid Cancers	NCT00969553
	Combination of BI6727 (Volasertib) and BIBF1120 in Solid Tumors	NCT01022853
	Volasertib in Combination With Azacitidine in Japanese Patients With Myelodysplastic Syndrome or Chronic Myelomonocytic Leukemia	NCT02201329
	Study of Volasertib and Belinostat in Patients With Relapsed and Refractory Aggressive B-cell and T-cell Lymphomas	NCT02875002
	Trial of BI 6727 (Volasertib) Monotherapy and BI 6727 in Combination With Pemetrexed Compared to Pemetrexed Monotherapy in Advanced NSCLC	NCT00824408
	Ph1 Volasertib Plus Romidepsin in R/R PTCL and CTCL	NCT02757248
	Trial of Volasertib With or Without Azacitidine in Patients With Myelodysplastic Syndromes	NCT02721875
	Trial of Intensive Chemotherapy With or Without Volasertib in Patients With Newly Diagnosed High-Risk Myelodysplastic Syndrome (MDS) and Acute Myeloid Leukemia (AML)	NCT02198482
	BI 6727 (Volasertib) Randomized Trial in Ovarian Cancer	NCT01121406
	Phase I Dose Escalation Trial of Volasertib in Combination With Azacitidine in Patients With MDS or CMML	NCT01957644
	Intravenous BI 6727 (Volasertib) in 2nd Line Treatment of Urothelial Cancer	NCT01023958
	Open Dose Escalating Trial to Determine the Maximum Tolerated Dose in Pediatric Patients With Advanced Cancers for Whom no Therapy is Known	NCT01971476
	Phase I/IIa Trial to Investigate BI 6727 (Volasertib) as Monotherapy or in Combination With Cytarabine in Acute Myeloid Leukaemia	NCT00804856
	Volasertib in Combination With Low-dose Cytarabine in Patients Aged 65 Years and Above With Previously Untreated Acute Myeloid Leukaemia, Who Are Ineligible for Intensive Remission Induction Therapy (POLO-AML-2)	NCT01721876

Acknowledgements

First, I would like to express my deepest appreciation to my supervisor Prof. Dr. Dr. Thomas Grünewald who kindly offered me a chance to join his team and educated me with valuable scientific knowledge at each of our many meetings and fully trusted me and my work for the entire process of my study.

I am especially grateful to Prof. Dr. Thomas Kirchner for being part of my Thesis Advisory Committee, agreeing to be a reviewer of my PhD thesis and providing the equipment required for carrying out experiments.

I would like to thank Prof. Andreas Jung for being part of my Thesis Advisory Committee and providing useful suggestions during the TAC meeting.

I owe my deepest gratitude to the China Scholarship Council (CSC) for their financial support, a help without which I would never have been able to complete this work.

Special thanks to Beate Luthart, Anja Heier and Andrea Sendelhofert for excellent technical assistance and their support during my thesis.

I would like to thank Florencia, Shunya, Cornelius and Gaby for proof-reading my manuscript and their helpful feedbacks.

I would like to thank Prof. Uta Dirksen, Prof. Javier Alonso and Prof. Wolfgang Hartmann who provided gene expression data or tissue-microarrays, and helped in statistical analysis of clinical data.

A special thanks goes to the whole AG Grünewald for their technical support and joyful moments that we shared in the lab.

My deepest appreciation goes to my parents and my family who, not only during my studies, but throughout my entire life have always been there for me and always encouraged me in everything I do.

Affidavit

LMU LUDWIG-MAXIMILIANS-UNIVERSITÄT MÜNCHEN

Dean's Office
Medical Faculty

MMRS

Affidavit

Li, Jing
Surname, first name

B410, Im Neuenheimer Feld 280
Street

69120, Heidelberg
Zip code, town

Germany
Country

I hereby declare, that the submitted thesis entitled

Therapeutic targeting of cytokinesis eradicates genomically silent childhood cancer

is my own work. I have only used the sources indicated and have not made unauthorised use of services of a third party. Where the work of others has been quoted or reproduced, the source is always given.

I further declare that the submitted thesis or parts thereof have not been presented as part of an examination degree to any other university.

Heidelberg,03.05.2021
Place, date

Jing Li
Signature doctoral candidate

Affidavit July 2019

Confirmation of congruency

LMU LUDWIG-MAXIMILIANS-UNIVERSITÄT MÜNCHEN

Dean's Office
Medical Faculty

MMRS

Confirmation of congruency between printed and electronic version of the doctoral thesis

Li, Jing
Surname, first name

B410, Im Neuenheimer Feld 280
Street

69120, Heidelberg
Zip code, town

Germany
Country

I hereby declare that the electronic version of the submitted thesis, entitled
Therapeutic targeting of cytokinesis eradicates genomically silent childhood cancer

is congruent with the printed version both in content and format.

Heidelberg,03.05.2021
Place, date

Jing Li
Signature doctoral candidate

Congruency of submitted versions July 2019

List of publications

Scientific papers published during the course of my PhD thesis:

Li, J., Dallmayer, M., Kirchner, T., Musa, J., Grünewald, T.G. (2018). PRC1: Linking Cytokinesis, Chromosomal Instability, and Cancer Evolution. Trends Cancer 4, 59–73.

Marchetto, A., Ohmura, S., Orth, M.F., Knott, M.M.L., Colombo, M.V., Arrigoni, C., Bardinet, V., Saucier, D., Wehweck, F.S., **Li, J.**, Stein, S., Gerke, J.S., Baldauf, M.C., Musa, J., Dallmayer, M., Romero-Pérez, L., Hölting, T.L.B., Amatruda, J.F., Cossarizza, A., Henssen, A.G., Kirchner, T., Moretti, M., Cidre-Aranaz, F., Sannino, G., Grünewald, T.G. (2020). Oncogenic hijacking of a developmental transcription factor evokes vulnerability toward oxidative stress in Ewing sarcoma. Nat Commun 2020 May; 11 (1): 2423.

Orth, M.F., Hölting, T.L.B., Dallmayer, M., Wehweck, F.S., Paul, T., Musa, J., Baldauf, M.C., Surdez, D., Delattre, O., Knott, M.M.L., Romero-Pérez, L., Kasan, M., Cidre- Aranaz, F., Gerke, J.S., Ohmura, S., **Li, J.**, Marchetto, A., Henssen, A.G., Özen, Ö., Sugita, S., Hasegawa, T., Kanaseki, T., Bertram, S., Dirksen, U., Hartmann, W., Kirchner, T., Grünewald, T.G. (2020). High Specificity of BCL11B and GLG1 for EWSR1-FLI1 and EWSR1-ERG Positive (2020) Ewing Sarcoma. Cancers (Basel). 10;12(3):644.

Gerke, J.S., Orth, M.F., Tolkach, Y., Romero-Pérez, L., Wehweck, F.S., Stein, S., Musa, J., Knott, M.M.L., Hölting, T.L.B., **Li, J.**, Sannino, G., Marchetto, A., Ohmura, S., Cidre-Aranaz, F., Müller-Nurasyid, M., Strauch, K., Stief, C., Kristiansen, G., Kirchner, T., Buchner, A., Grünewald, T.G. Integrative clinical transcriptome analysis reveals TMPRSS2-ERG dependency of prognostic biomarkers in prostate adenocarcinoma. Int. J. Cancer. 2020 146 (7):2036-2046.

Musa, J., Cidre-Aranaz, F., Aynaud, M.M., Orth, M.F., Knott, M.M.L., Mirabeau, M., Mazor, G., Varon, M., Hölting, T.L.B., Grossetête, S., Gartlgruber, M., Surdez,

D., Gerke, J.S., Ohmura, S., Marchetto, A., Dallmayer, M., Baldauf, M.C., Stein, S., Sannino, G., **Li, J.**, Romero-Pérez, L., Westermann, F., Hartmann, W., Dirksen, U., Gymrek, M., Anderson, N.D., Shlien, A., Rotblat, B., Kirchner, T., Delattre, O., Grünewald, T.G. (2019). Cooperation of cancer drivers with germline regulatory variants shapes clinical outcomes. Nat Commun 2019 Sept; 10 (1): 4128

Sannino, G., Marchetto, A., Ranft, A., Jabar, S., Zacherl, C., Alba-Rubio, R., Stein, S., Wehweck, F.S., Kiran, M.M., Hölting, T.L.B., **Li, J.**, Jürgens, H., Sastre, A., Alonso, J., Da Silveira, W., Hardiman, G., Gerke, J.S., Orth, M.F., Hartmann, W., Kirchner, T., Ohmura, S., Dirksen, U., Grünewald, T.G. (2019). Gene expression and immunohistochemical analyses identify SOX2 as major risk factor for overall survival and relapse in Ewing sarcoma patients. EBioMedicine 47,156–162.

Dallmayer, M., **Li, J.**, Ohmura, S., Alba Rubio, R., Baldauf, M.C., Hölting, T.L.B., Musa, J., Knott, M.M.L., Stein, S., Cidre-Aranaz, F., Wehweck, F.S., Romero-Pérez, L., Gerke, J.S., Orth, M.F., Marchetto, A., Kirchner, T., Bach, H., Sannino, G., Grünewald, T.G. (2019). Targeting the CALCB/RAMP1 axis inhibits growth of Ewing sarcoma. Cell Death Dis. 10, 116.

Orth, M.F., Gerke, J.S., Knösel, T., Altendorf-Hofmann, A., Musa, J., Alba-Rubio, R., Stein, S., Hölting, T.L.B., Cidre-Aranaz, F., Romero-Pérez, L., **Li, J.**, Hakozaki, M., Kirchner, T., Dandekar, T., Butt, E., Grünewald, T.G. (2019). Functional genomics identifies AMPD2 as a new prognostic marker for undifferentiated pleomorphic sarcoma. Int. J. Cancer 144, 859–867.

Musa, J., **Li, J.**, Grünewald, T.G. (2019). Hepatitis B virus large surface protein is priming for hepatocellular carcinoma development via induction of cytokinesis failure. J. Pathol. 247, 6–8.

Baldauf, M.C., Gerke, J.S., Kirschner, A., Blaeschke, F., Effenberger, M., Schober, K., Rubio, R.A., Kanaseki, T., Kiran, M.M., Dallmayer, M., **Li, J.**, Busch, D.H., Feuchtinger, T., Ohmura, S., Orth, M.F., Thiel, U., Kirchner, T., Grünewald, T.G. (2018). Systematic identification of cancer-specific MHC-binding peptides with RAVEN. Oncoimmunology 7, e1481558.

Baldauf, M.C., Orth, M.F., Dallmayer, M., Marchetto, A., Gerke, J.S., Rubio, R.A., Kiran, M.M., Musa, J., Knott, M.M.L., Ohmura, S., **Li, J.**, Akpolat, N., Akatli, A.N., Özen, Ö., Dirksen, U., Hartmann, W., de Alava, E., Baumhoer, D., Sannino, G., Kirchner, T., Grünewald, T.G. (2018). Robust diagnosis of Ewing sarcoma by immunohistochemical detection of super-enhancer-driven EWSR1-ETS targets. Oncotarget 9, 1587–1601.